Study on Broadband SIS Receivers with Nb/AlOx/Nb Tunnel Junctions at Millimeter Wavelengths

Thesis by

Masanori Takeda

In Partial Fulfillment of the Requirements

for the Degree of

DOCTOR OF ENGINEERING

Department of Astronomical Science

School of Mathematical and Physical Science

The Graduate University for Advanced Studies

September 2002

ACKNOWLEDGMENT

CONTENTS

Appendixes

Chapter I

Introduction

1.1 General radio-telescope receivers

The radio-telescope receivers have been used for ground-based astronomical and atmospheric observations at millimeter and submillimeter wavelengths. The wavelength band of interest is mainly determined by the attenuating nature of the earth's atmosphere as shown in Fig. 1.1 [1]. The power level of the signal is so small, of the order of 10^{-15} to 10^{-20} W, that the development of low-noise receivers is greatly important. At wavelengths longer than 3 mm receivers using cooled low-noise preamplifier such as high-electron-mobility transistor (HEMT) are generally used [2-4], while at shorter wavelengths two types of receivers offer the best performance. One is incoherent or direct receivers such as bolometer, which determine only the intensity of the observed source, and the other is coherent receivers, namely heterodyne receivers such as Schottky barrier diode [5, 6] and SIS (superconductor-insulator-superconductor) receivers [7, 8], which determine both the intensity and the phase of the observed source.

Direct detector is a process in which a photon either raises the temperature of a bolometer element or causes an electron current to flow in a photoconductor. This is a power detection process in which the fundamental noise limiting the sensitivity is the noise in the signal. Since the detector does not actually follow the applied ac power, frequency selectivity is obtained by placing a filter in front of the detector such as in a Fabry-Perot interferometer system. The system resolution and frequency band are

governed by the input-filter.

Most millimeter and submillimeter-wave receivers used in radio astronomy employ the heterodyne technique because the signal frequencies are too high to be manipulated. The input signal radiation at frequency ω_S from the telescope is coupled into the mixer through a feed horn or quasioptical antenna. The mixer combines the signal with local oscillator radiation at frequency ω_{LO} to produce a beat at the intermediate frequency (IF) $\omega_{IF} = |\omega_S \quad \omega_{LO}|$. The IF output is then amplified and fed to some sort of spectrometer to reproduce and display the spectrum of the input signal. This process is schematically depicted in Fig. 1.2 in which radiation in a band at 100 GHz ± 1.5 GHz is downconverted into the same IF band (ω_{IF}), the receiver is operated in double sideband (DSB) mode, as opposed to signal sideband (SSB) mode, where the image frequency (ω_I) is filtered out.

The sensitivity or the minimum detectable signal ΔT_{min} for both types of receivers are governed by radiometer equation [9]

$$\Delta T_{\min} = \frac{T_{sys}}{\sqrt{\Delta v \tau}},$$
(1.1)

where T_{sys} is the system noise temperature, Δv and τ represent the predetection bandwidth and postdetection integration time, respectively. It is found from equation (1.1) that the improvement of sensitivity is to lower the system noise temperature as far as the observation efficiency is concerned. The equivalent input noise temperature of the heterodyne receiver system shown in Fig. 1.3 is characterized by the following expression if high-gain IF- and post-amplifiers are employed:

$$T_{sys} = T_{in} + L_{in}T_{mix} + L_{in}L_{mix}T_{IF},$$
(1.2)

where T_{in} and L_{in} are the noise temperature and loss of the RF input system, and T_{mix} and

2

L_{mix} are the noise temperature and conversion loss of the mixer element, respectively, and T_{IF} is the noise temperature of the IF-chain. From this expression, it is obvious that the mixer in a low-noise receiver should have intrinsically low noise and high conversion efficiency.

1.2 Brief review of SIS mixers

Three types of heterodyne mixer elements have been used at millimeter and submillimeter wavelengths; Schottky diodes, SIS tunnel junctions, and recently developed hot-electron bolometer mixers [7]. The typical DSB receiver noise temperature as a function of LO frequency is summarized in Fig. 1.4. In this figure, the solid straight line represents the quantum limited noise temperature of $h\nu/k$, where h is Plank's constant, ν is frequency, and k is Boltzmann's constant. From this figure, it is found that SIS mixers are the most sensitive detectors at the millimeter and submillimeter wavelengths (at frequencies below the superconducting gap frequency). The theoretical treatment of SIS mixers was established by J.R. Tucker in 1979, and it was predicted that the SIS mixers have the possibilities of the quantum limited noise and mixer conversion gain [10].

SIS junction consists of two superconducting layers separated by an insulator with a few atomic-layer thickness of a few atoms thick, through which a current can flow via quantum mechanical tunneling of electrons. The advantage of the SIS mixer is firstly the extremely strong nonlinearity of the dc current-voltage (I-V) characteristic compared with that of other nonlinear devices such as Schttoky diode. The width of the dc nonlinearity is small compared with the photon energy $h\nu/e$ of the signal, where e is the electron charge. Such a strong nonlinearity provides a mixing element capable for

3

conversion gain (i.e. $L_m < 1$) and low noise temperature. Secondly, the bias voltage in the operation is small, of the order of a few millivolts, while in the Schottky diode it is the order of several tens millivolts. Thirdly, the LO power required for the SIS mixer is much smaller than for Schottky diodes, enabling compact lightweight LO supplies for space applications.

The I-V characteristics of an SIS junction can be explained by the simplified energy-band diagram shown in Fig. 1.4. The superconductors on both sides of the tunnel barrier are in their ground states at $T = 0$ K, and there is an energy gap 2Δ for each electrode required in order to break up a Cooper pair to produce two quasiparticle excitations. Therefore no current can flow until the voltage is large enough for the quasiparticles to overcome the gap. At this gap voltage $V_g = 2\Delta/e$, the infinite densities of states are arisen, causing a steep current rise. The superconductor commonly used is niobium (Nb), with a superconducting transition temperature of 9.2 K. The gap voltage of Nb at 4.2 K is about 2.8 mV.

In the presence of a radiation field, the absorption of incoming photon can provide enough energy for the quasiparticle tunneling. Then the current steps can occur below the gap voltage shown in Fig. 1.5. This phenomenon, which is called "photon-assisted tunneling", suggests that the SIS junctions can be employed as the direct detectors.

The upper frequency limit of SIS mixers is characterized by the gap energy 2Δ. In theory [11], an SIS junction operates as a heterodyne detector as far as it is no longer nonlinear with respect to the radiation. When the voltage modulation produced by the impinging signal is larger than the voltage nonlinearity of the SIS junction, the junction stops mixing. Since the I-V curve of an SIS junction is symmetric, the effective width of the nonlinearity is 4Δ. In the niobium junction, the frequency limit as a mixer is 1.4 THz,

4

twice the gap frequency of Nb.

Superconductors are used as microstrip material to guide the signal towards the junction. Although SIS junctions are possible to mix the signal up to twice the gap frequency, other frequency limit exists in the superconducting microstrip in the mixer. SIS junctions have large geometrical capacitance. This capacitance tends to shunt the incoming high frequency signal. To overcome this problem, the inductive component using microstrips is added to the junction to resonate out the capacitance at a frequency where the resulting impedance of junction is simply the junction resistance. The analogous electronic circuit is a resonant RLC circuit, which has a certain bandwidth around a center frequency. In principle, the superconducting microstrip is extremely low-loss below the gap frequency. Above the gap frequency, however, the RF losses increase significantly because of the onset of pair-breaking [12]. In mixers based on Nb, the upper frequency limit of the microstrip is the gap frequency of 700 GHz.

From the above discussion, SIS mixers using Nb junctions can be used as the excellent mixer up to 700 GHz and can maximally operate as the mixer to 1.4 THz while replacing wiring Nb films with films of smaller surface resistance (e.g. Al and Au) [13]. Niobium-nitride (NbN) tunnel junctions appear a good candidate beyond 700 GHz, as the gap frequency is around 1.4 THz and high-quality NbN junctions can be fabricated [14], yet the performance of SIS mixers using NbN junctions is not competitive and appear to degrade rapidly with frequency, possibly due to film losses [15, 16].

1.3 Importance of broadband SIS mixers

To obtain information on the variety and abundance of gases present in galaxies or

the atmosphere, a spectrum measurement of the incoming signal is required. Most objects in the universe have a strong angular momentum, causing gases, e.g. in outer rings of newly forming stars, to have a large difference in velocity upon movement towards or away from the observer. This causes Doppler shifts in the frequency, like the well known "red-shift" caused by the expansion of the universe. For this reason, rotational lines can be broadened. Since the spectral shape provides information on the velocities with which the object is moving, the entire line shape which can be broadened with several GHz must be measured in a single scan. This poses a lower limit to the bandwidth of receivers when used for astrophysical observations.

An atmospheric window exists in the frequency range from 190 to 300 GHz as shown in Fig. 1.1. There are many interesting spectral lines in both astronomical and atmospheric observations in the region. For example, CS (J = 4-3) emission at 195.9 GHz, CO (J = 2-1) emission at 230.5 GHz, HCN emission at 265.9 GHz and CS (J=6-5) emission at 293.9 GHz in the astronomical observation, and O_3 emissions at 235.7 GHz and 276.9 GHz, ClO emissions at 204.3 GHz and 278.6 GHz, and HNO_3 emission at 269.1 GHz in the atmospheric observation. Usually, two receivers have been used for the complete observation in the region, for example in the case of ozone observation project in Communications Research Laboratory (CRL), a receiver can operate at 190-237 GHz, other one can operate at 242-290 GHz [17]. Broadbanding the receiver so as to operate at 190-300 GHz may be brought a great improvement of the observation efficiency and the reduction of cost in constructing the observation system. The broadband SIS receivers are also greatly helpful in the complex systems such as the radio interferometers and multi-beam receivers.

In SIS mixers integrated tuning circuit, the bandwidth is determined by the $\omega R_n C_j$

6

product, which strongly depends on the critical current density of an SIS junction. Here ω, R_n, and C_j represent the angular frequency of signal, normal-state resistance and geometrical capacitance of an SIS junction, respectively. The broader bandwidth can achieve in the smaller $\omega R_n C_j$ product, which means the higher critical current density. Note that the I-V characteristics for Nb-based SIS junctions show poor tunneling performance (i.e. increased subgap leakage current) at current densities above 10 kA/cm^2, resulting poor noise performance of SIS mixers. Since the required critical current density becomes larger as the signal frequency is higher, the development of the broadband SIS mixers makes very difficult at the submillimeter wavelength.

1.4 Survey of this work

The purpose of this work was to develop broadband SIS mixers using Nb/AlOx/Nb tunnel junctions. Especially, the development of broadband SIS mixers with lower critical current densities of a junction compared with the conventional SIS mixers. In order to achieve the purpose, SIS mixers with inhomogeneous distributed junction arrays, which are new tuning method for canceling out the geometrical capacitance of a junction, were proposed in this work. Based on this new type of tuning circuit, a millimeter-wave band SIS mixer was designed, fabricated, and evaluated. It is found that extremely broadband operation can be achieved by this type of SIS mixer. I believe that these results make an important contribution to radio astronomy and atmospheric observation.

This thesis comprises seven chapters. Chapter 2 describes the fundamental theory on which the thesis is largely based. Firstly, the mechanism of photon-assisted tunneling is presented using the simplified energy-band diagram. Then Tucker's quantum theory

7

of mixing is summarized in the large-signal, small-signal, and noise analyses. Lastly, the general knowledge of superconducting microstrips is presented for designing the tuning circuits.

Chapter 3 describes the properties of various fixed tuned SIS mixers reported up to now. Firstly, the general properties of the tuning circuits using the parallel inductance, end-load, and two-junction are represented and then the relation between the tuning bandwidth and the critical current density of a junction is discussed. It introduces SIS mixers with distributed junction arrays, in which the critical current density can be lowered compared with those of conventional single-junction SIS mixers in order to achieve the reasonable bandwidth, and modifies the Tucker's quantum theory of mixing for the distributed junction array. Lastly, the theoretical calculations of mixing properties for distributed junction array are carried out and the advantage and disadvantage of distributed junction arrays are clarified.

Chapter 4 describes the design and properties of a 190-300 GHz band waveguide SIS mixer with an inhomogeneous distributed junction array using Nb/AlOx/Nb tunnel junctions. Firstly, to overcome the disadvantage of conventional distributed junction arrays clarified in Chapter 3, SIS mixers with inhomogeneous distributed junction arrays are newly proposed, and the design method is presented. Then the theoretical mixing properties are discussed in detail. It is shown that the large noise increase, which always occurs at certain frequencies in the conventional distributed junction array, can be reduced in the inhomogeneous distributed junction array. Lastly, the waveguide SIS mixer-chip layout for the inhomogeneous distributed junction array is described.

Chapter 5 describes the fabrication and properties of Nb/AlOx/Nb tunnel junctions. Firstly, the fabrication process is explained and the dc I-V characteristic of the junction

8

is presented.

Chapter 6 describes the experimental results of the 110-180 GHz and 190-300 GHz bands SIS mixers with the inhomogeneous distributed junction arrays. Firstly, the mixer layout and measurement set-up of the 110-180 GHz SIS mixer are described. Detailed measurements of the receiver noise temperature are made in the frequency range from 100 to 146 GHz. Comparing the conventional SIS mixer with two-junction, the broadband operation of the inhomogeneous distributed junction array is demonstrated in the heterodyne measurement. In the 190-300 GHz band SIS mixer, the performance is evaluated using both of the Fourier transform spectroscopy (FTS) and heterodyne measurements. In the FTS measurement, the bandwidth performance of the inhomogeneous distributed junction array is compared with that of a conventional distributed junction array. The receiver noise temperature is measured in the frequency range from 190 to 284 GHz. The mixing properties are analyzed quantitatively by breaking down the receiver noise temperature into the contributions due to input noise, mixer noise, and IF-chain noise. An uncorrected DSB receiver noise temperature of $5h\nu/k$ was obtained in the frequency range from 205 to 284 GHz.

Chapter 7 concludes the present work described in this work.

References

[1] H. Matsuo, A. Sakamoto, and S. Matsushita, "FTS measurements of submillimeter-wave atmospheric opacity at Pampa la Bola", *Publ. the Astronomical Society of Japan*, **50**, 359 (1998).

[2] M. W. Pospieszalski, "Ultra-low-noise receivers for the 1 to 120 GHz frequency

range", *Proc. 23rd European Microwave Conf.*, Madrid, Spain, 73, September (1993).

[3] M. W. Pospieszalski, L. D. Nguyen, M. Lui, T. Lui, M. A. Thompson, and M. J. Delaney, "Very low noise and low power operation of cryogenic AlInAs/GaInAs/InP HFET's", *Proc. IEEE MTT-S Int. Microwave Symp.*, San Dieo, CA, 1345 (1994).

[4] K. H. G. Duh, S. M. J. Liu, S. C. Wang, M. Y. Kao, P. Ho, P. M. Smith, P. C. Chao, and M. W. Pospiesalski, "InP HEMTS-next generation millimeter-wave devices", *Proc. Asia Microwave Conference*, Tokyo, Japan, 1053, December (1994).

[5] H. P. Röser, H. W. Hubers, T. W. Crowe, and W. C. B. Peatman, "nanostructure GaAs Schottky diodes for far-infrared heterodyne receivers", *Infrared Phisics and Technology*, **35**, 451 (1994).

[6] T. W. Crowe, R. J. Mattauch, H. P. Röser, W. L. Bishop, W. C. B. Peatman, and X. L. Liu, "GaAs Schottky diodes for THz mixing applications", *Proc IEEE*, 80, 1827, (1992).

[7] J. Carlstrom and J. Zmuidzinas, "Millimeter and submillimeter techniques", *Review of Radio Science 1993-1996*, edited by W. Ross Stone (The Oxford University Press, Oxford, 1996).

[8] R. Blundell and C. E. Tong, "Submillimeter receivers for radio astronomy", *Proc. IEEE*, **80**, 1702 (1992).

[9] J. D. Kraus, *RadioAstronomy*, 2nd edition, Powell, OH: Cygnus-Quasar Books (1986).

[10] J.R. Tucker, "Quantum limited detection in tunnel junction mixers", *IEEE J. Quantum Electon.*, **15**, 1234, (1979).

[11] M. J. Feldman, "Theoretical considerations for THz SIS mixerx", *Int. J. Infrared & MM Waves*, 8, 1287 (1987).

10

[12] D. C. Mattis and J. Bardeen, "Theory of the anomalous skin effect in normal and superconducting material", *Phys. Rev.*, **111**, 412 (1958).

[13] M. Bin, M. C. Gaidis, J. Zmuidzinas, and T. G. Phillips, "Low-noise 1 THz niobium superconducting tunnel junction mixer with a normal metal tuning circuit", *Appl. Phys. Lett.*, **68**, 12, 1714 (1996).

[14] Z. Wang, A. Kawakami, and Y. Uzawa, "NbN/AlN/NbN tunnel junctions with high current density up to 54 kA/cm2", *Appl. Phys. Lett.*, **70**, 114 (1997).

[15] Y. Uzawa, Z. Wang, and A. Kawakami, "All-NbN quasi-optical SIS mixers at terahertz frequencies", *Proc. 8th Int. Symp. Space Terahertz Technology*, Boston, USA, 301, March (1997).

[16] P. Dieleman, T. M. Klapwijk, H. van de Stadt, M. Schicke, B. Plathner, and K. H. Gundlach, "Performance limitations of NbN SIS junctions with Al striplines at 600-850 GHz", *Proc. 8th Int. Symp. Space Terahertz Technology*, Boston, USA, 291, March (1997).

[17] H. Masuko, S. Ochiai, and Y. Irimajiri, "CRL 204 GHz and 278 GHz band radiometer/spectrometer system with superconductor mixers for monitoring ozone layer destruction", *Proc. Asia-Pacific Microwave Conference*, Chiba, Japan, 107, July (1994).
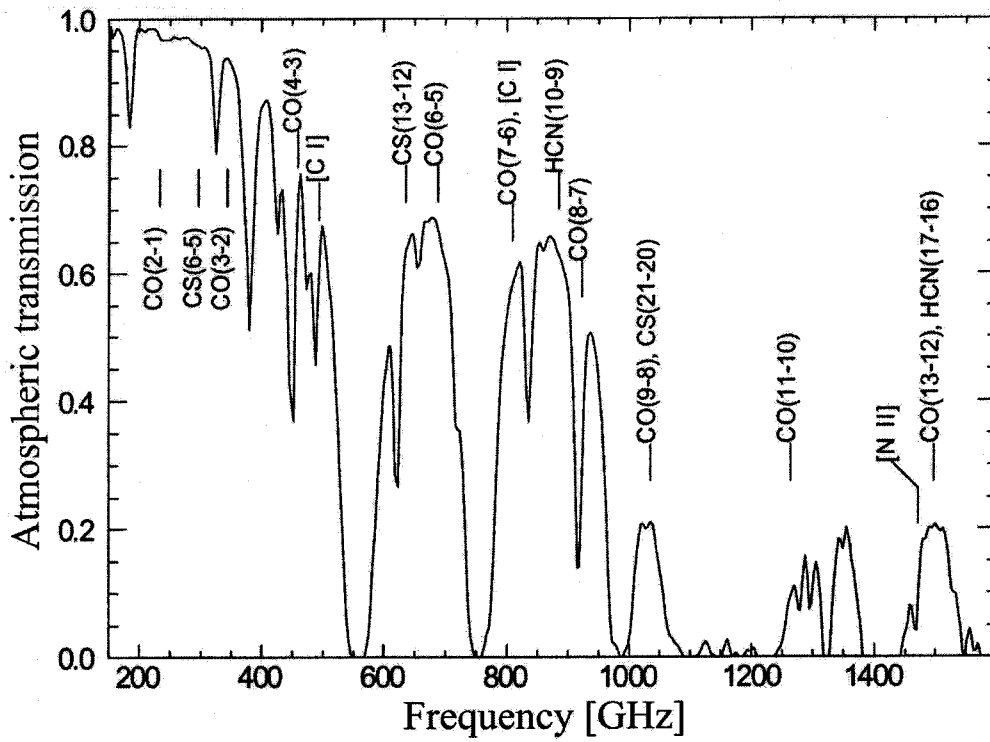
Figure 1.1 Atmospheric transmission at Pampa la Bola.
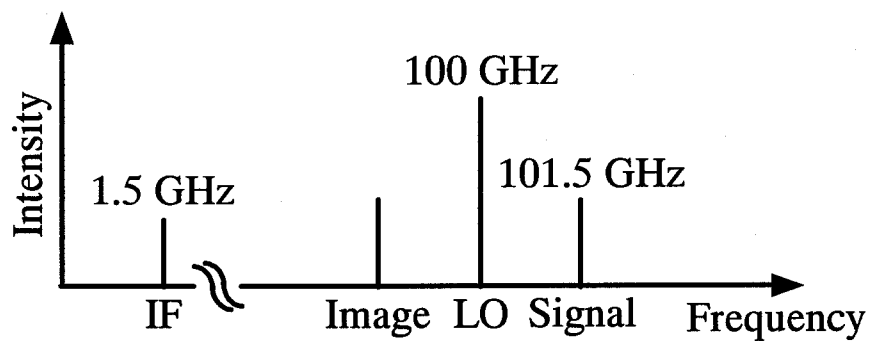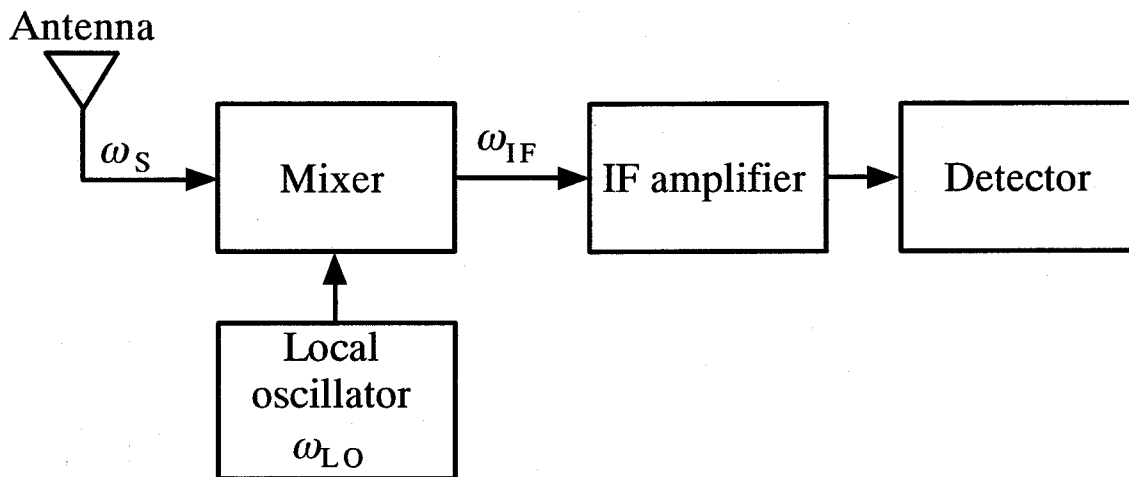
Figure 1.2 Schematic overview of a heterodyne mixer and mixing process.
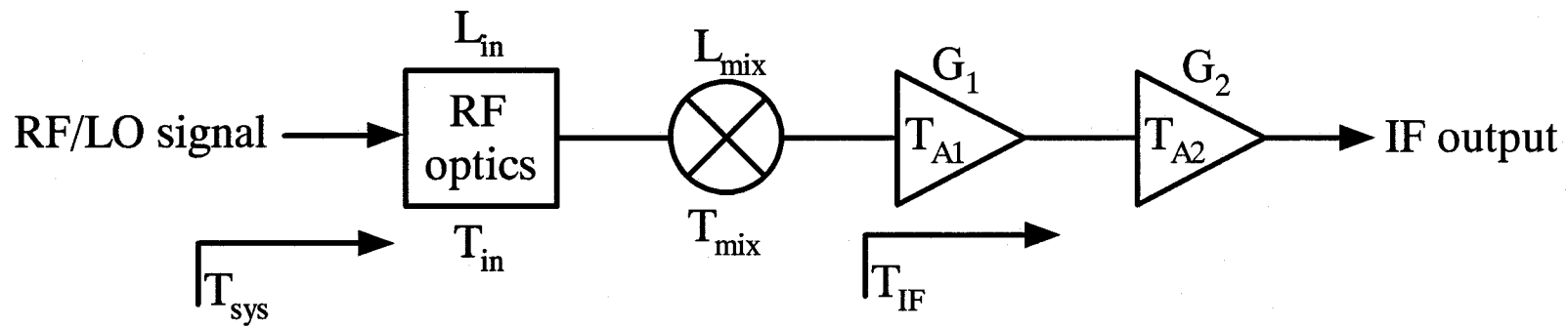
$$T_{sys} = T_{in} + L_{in} T_{mix} + L_{in} L_{mix} T_{A1} + \frac{L_{in} L_{mix}}{G_1} T_{A2}$$

Figure 1.3 The equivalent input noise temperature of the heterodyne receiver system.
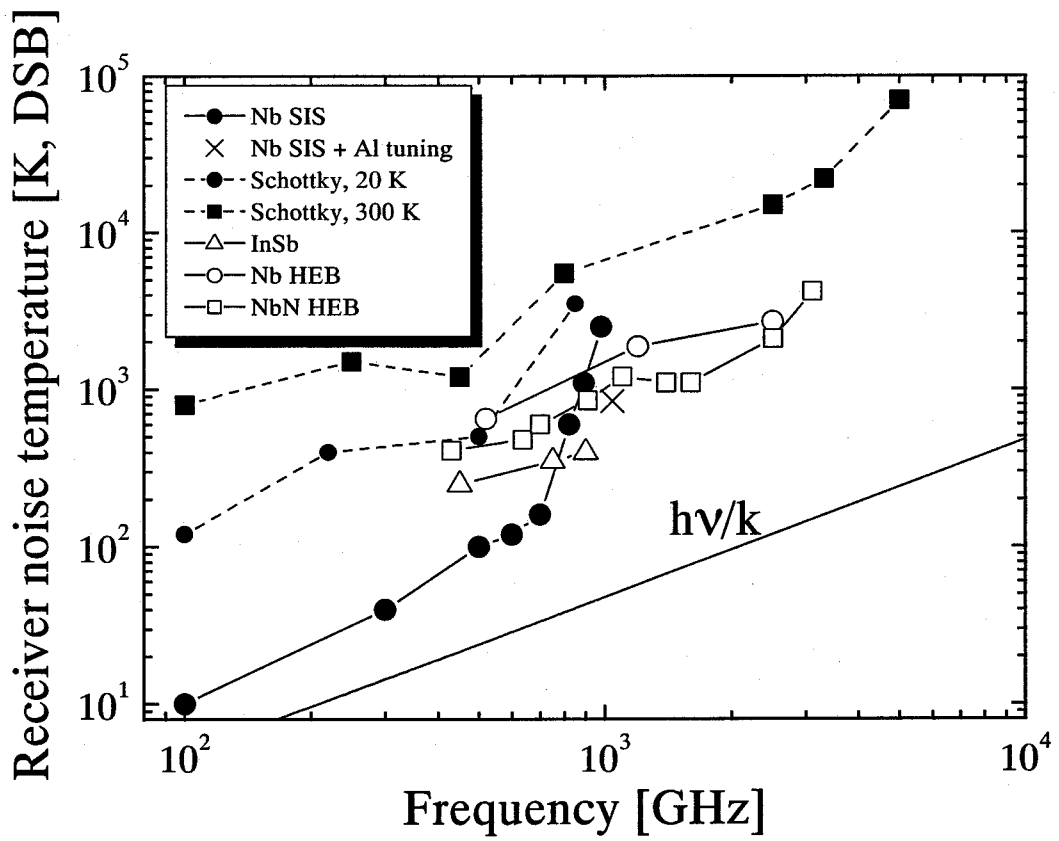
Figure 1.4 The state of the art of heterodyne receivers at millimeter and submillimeter wavelengths.

E

Δ $\hbar\omega$

E_F Δ

E_F

S I S

(a)

I

$\hbar\omega/e$

$2\Delta/e$ V

(b)
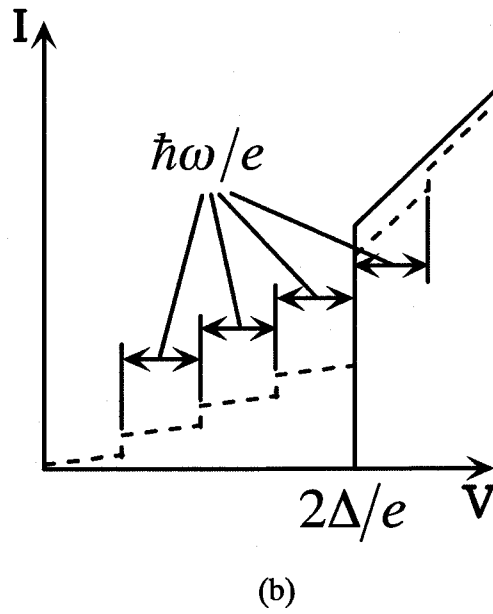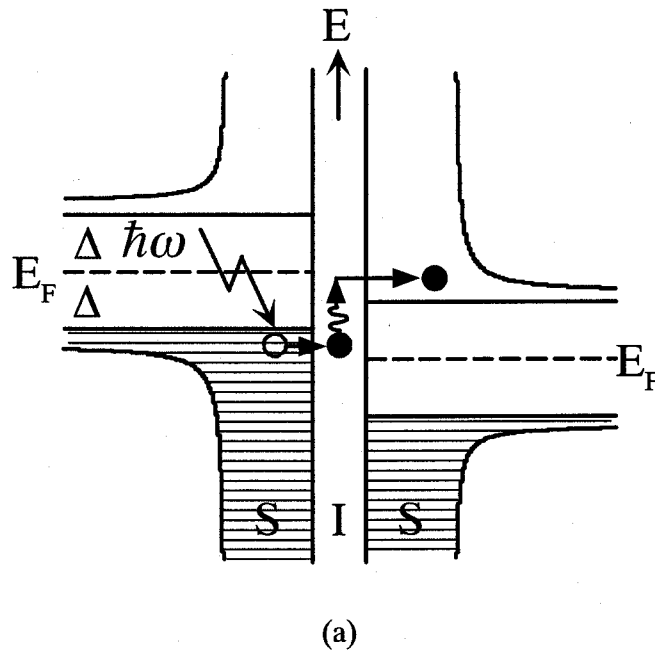
Figure 1.5 (a) Energy diagram of the SIS structure with an applied voltage. An incoming photon can raise the energy of a quasiparticle enabling photon-assisted tunneling. (b) The resulting current-voltage characteristics with (dotted line) and without (solid line) irradiation.

Chapter II

Fundamental theory of SIS mixers

2.1 Photon-assisted tunneling

Photon-assisted tunneling was discovered experimentally by Dayem and Martin in 1962, and explained quantitatively by Tien and Gordon in 1963. In an ideal SIS junction at $T = 0$ K, a quasiparticle can not flow through the tunneling barrier to the bias voltages below the gap voltage of $2\Delta/e$. When electromagnetic waves irradiate the SIS junction, however, the quasiparticle produced by the broken Cooper pair can passes through the tunneling barrier by absorbing the photon energy, even if the bias voltages are below the gap voltage. As a result, quasiparticle steps appear below and above the gap voltage with a space of $\hbar\omega/e$, as shown in Fig. 1.4(b).

Let us consider the presence of a high frequency signal represented by a time dependent voltage applied an SIS junction in addition to a dc bias;

$$V = V_0 + V_\omega \cos\omega t \tag{2.1}$$

This applied voltage will be assumed to modulate adiabatically the potential energy for each quasiparticle level on the ungrounded side of the barrier. The time dependence of the wave function for one electron state can be expressed by the following equation,

$$\psi_i(r,t) = \psi_i(r)\exp\left\{-\frac{i}{\hbar}\int^t dt'[E_i + eV(t')]\right\}$$

$$= \psi_i(r)\exp\left[-i\frac{(E_i + eV_0)t}{\hbar}\right]\sum_{n=-\infty}^{\infty} J_n\left(\frac{eV_\omega}{\hbar\omega}\right)e^{-in\omega t} \tag{2.2}$$

where E_i is the unperturbed energy of the Bloch state and J_n is the n-th order Bessel function (of the first kind). The wave function for one side of superconductor is the sum of the energies such as $E, E \pm \hbar\omega, E \pm 2\hbar\omega, \cdots$, in the opposite side of superconductor.

The dc tunneling current can be given using the conventional tunneling theory;

$$I_0(V_0, V_\omega) = \sum_{n=-\infty}^{\infty} J_n^2 \left(\frac{eV_\omega}{\hbar\omega} \right) I_{dc}\left(V_0 + \frac{n\hbar\omega}{e} \right) \qquad (2.3)$$

$I_{dc}(V_0)$ represents the unmodulated dc I-V characteristic and can express by

$$I_{dc}(V_0) = \frac{G_n}{e} \int \frac{|E' - eV_0|}{\left[(eV_0 - E')^2 - \Delta^2 \right]^{1/2}} \frac{|E'|}{\left[E'^2 - \Delta^2 \right]^{1/2}} \left[f(E' - eV_0) - f(E') \right] dE', \qquad (2.4)$$

where G_n is the normal-state tunneling conductance, and $f(E)$ is the Fermi-Dirac (distribution) function at the ambient temperature T:

$$f(E) = \frac{1}{1 + e^{E/kT}}. \qquad (2.5)$$

As shown in (2.3), in the presence of RF power, the magnitude of the n-th photon-assisted tunneling step is determined through $J_n^2 \left(eV_\omega / \hbar\omega \right)$ and the quasiparticle steps appear at voltage displacements corresponding to integral multiples of $\hbar\omega/e$. Using this quantum effect, we can detect electromagnetic waves sensitively.

2.2 Quantum theory of mixing

In 1979, Tucker developed a quantum theory of mixing based upon the microscopic quantum physics in order to predict the high-frequency behavior of nonlinear quasiparticle tunneling SIS junction as heterodyne mixers [3]. Fundamental theory for classical mixers was studied in depth by Torrey and Whitmer [4], Uhlir [5], Saleh [6], and Held and Kerr [7]. Although the physical mechanism and the actual behavior for the mixer are distinct between a semiconductor diode and an SIS junction as classical versus quantum mixing, their performance can be analyzed using the same strategy. In the first step, a large-signal analysis is carried out to solve self-consistently

18

for the large-amplitude LO waveform impressed the SIS junction. Then, a small-signal analysis is carried out to derive the admittance matrix, in which the conversion for the power between the mixing frequencies can be characterized, and the noise temperature of the SIS mixer is finally evaluated by a noise analysis. The essential results of the quantum theory of mixing are summarized in this section.

2.2.1 Large-signal analysis

The expectation value for the average quasiparticle current flowing through the tunnel barrier may be written in the form

$$\langle I(t) \rangle = \mathrm{Im} \int_{-\infty}^{\infty} d\omega' d\omega'' W(\omega') W^*(\omega'') j(V_0 + \hbar\omega'/e) e^{-i(\omega'-\omega'')t} , \qquad (2.6)$$

where $j(V)$ is the complex response function introduced by Werthamer [8]. Here the effect of a time-dependent potential $V(t)$ across the junction is expressed in terms of the Fourier transform of the phase factor

$$\int_{-\infty}^{\infty} d\omega' W(\omega') e^{-i\omega't} = \exp\left\{ -\frac{ie}{\hbar} \int^t dt' [V(t') - V_0] \right\}. \qquad (2.7)$$

When the time-dependent voltage across the tunnel barrier will be of the form

$$V(t) = V_0 + V_{LO} \cos \omega t , \qquad (2.8)$$

the additional phase factor of (2.7) then becomes

$$W(\omega') = \sum_{n=-\infty}^{\infty} J_n(eV_{LO}/\hbar\omega) \delta(\omega' - n\omega). \qquad (2.9)$$

The induced tunneling current is obtained by substituting (2.9) into (2.6):

$$I_{LO}(t) = \mathrm{Im} \sum_{n,m=-\infty}^{\infty} J_n(\alpha) J_{n+m}(\alpha) e^{im\omega t} j(V_0 + n\hbar\omega/e), \qquad (2.10)$$

where the amplitude of the LO waveform is contained in the argument of the Bessel functions:

$$\alpha = eV_{LO}/\hbar\omega .$$

(2.11)

The current in the junction can be defined in terms of a complex current amplitude I_{LO}^{ω}.

With the assumption that the higher harmonics of the LO are short circuited, the actual

current in the junction is $\mathrm{Re}\!\left(I_{LO}^{\omega}e^{i\omega t}\right)$. The expressions for the current through the

junction is given by:

$$I_{LO}^{\omega} = I_{LO}' + iI_{LO}''$$

$$I_{LO}' = \sum_{n=-\infty}^{\infty} J_n(\alpha)\big[J_{n-1}(\alpha) + J_{n+1}(\alpha)\big]I_{dc}\big(V_0 + n\hbar\omega/e\big)$$

(2.12)

$$I_{LO}'' = \sum_{n=-\infty}^{\infty} J_n(\alpha)\big[J_{n-1}(\alpha) - J_{n+1}(\alpha)\big]I_{KK}\big(V_0 + n\hbar\omega/e\big)$$

$I_{dc}(V)$ is the dc I-V curve directly measured and is expressed by

$$I_{dc}(V) = \mathrm{Im}\, j(V) .$$

(2.13)

$I_{KK}(V)$ is the reactive part of the tunneling current and is via a Kramers-Kronig

transform connected to $I_{dc}(V)$:

$$I_{KK}(V) \equiv \mathrm{Re}\, j(V) = P\!\int_{-\infty}^{\infty} \frac{dV'}{\pi}\, \frac{I_{dc}(V') - V'/R_n}{V' - V} ,$$

(2.14)

where R_n is the normal-state resistance.

The equivalent circuit for the mixer at the LO frequency w is illustrated in Fig. 2.1.

The LO source is represented by a current generator J_{LO} and an effective source

admittance $Y_\omega = G_\omega + iB_\omega$ determined by the input circuit such as the waveguide and the

mounting structure. The susceptance B_ω includes a contribution ωC_j due to the

geometrical capacitance of the junction. The circuit equation in Fig. 2.1 may be written

in the form

$$J_{LO} = I_{LO}^{\omega} + Y_\omega V_{LO} .$$

(2.15)

The available power of the LO incident on the mixer is given by:

$$P_{LO} = \frac{|J_{LO}|^2}{8G_\omega}$$

$$= \frac{1}{8G_\omega}\left[\left(I'_{LO} + G_\omega V_{LO}\right)^2 + \left(I''_{LO} + B_\omega V_{LO}\right)^2\right]$$

(2.16)

The goal of the large-signal analysis is to determine the amplitude V_{LO} of the LO waveform across the junction in terms of the incident power P_{LO} and the effective source admittance Y_ω by an iterative solution to (2.12) and (2.16) using the measurement of a scale model for the mixer or a full large-signal analysis.

2.2.2 Small-signal analysis

The small-signal mixing properties of the SIS junction may be calculated once the amplitude of the LO waveform has been determined. The task at this section is to generate an admittance conversion matrix.

A mixer is sensitive to many frequencies as well as those at which it is designed to operate. Assuming an applied LO frequency ω and the output frequency, which is the intermediate frequency (IF), at ω_0, we can express all sideband frequencies of the current across the junction as

$$\omega_m = m\omega + \omega_0,$$

(2.17)

where $m = 0, \pm1, \pm2,...$ and is any integer. Note that $\omega_1 = \omega + \omega_0$ is equal to a signal frequency ω_S, and that $\omega_{-1} = \omega + \omega_0$ is the image frequency.

The equivalent circuit for a mixer is schematically illustrated in Fig. 2.2, which shows a mixer port with a termination impedance expressed here for convenience as an admittance Y_m. The incoming signal at frequency ω_S is represented by I_S with source admittance $Y_1 = Y_S$, and the problem of interest is the conversion of power to the output frequency ω_0 and its delivery into the load $Y_0 = Y_L$.

21

The sideband voltages and currents across the junction may be represented in the form:

$$v_{SIG} = \mathrm{Re} \sum_{m=-\infty}^{\infty} v_m \exp(i\omega_m t) \qquad (2.18)$$

$$i_{SIG} = \mathrm{Re} \sum_{m=-\infty}^{\infty} i_m \exp(i\omega_m t) \qquad (2.19)$$

These current and voltage components are linearly related for small signals via an admittance matrix

$$i_m = \sum_{m'} Y_{mm'} v_{m'} \, , \qquad (2.20)$$

where

$$Y_{mm'} = G_{mm'} + iB_{mm'}. \qquad (2.21)$$

The elements of this matrix are determined by the large-signal solution, and depend on the strength of LO power and the DC I-V characteristic of the junction.

The total voltage and current across the junction may be written in the form:

$$V(t) = V_0 + V_{LO}(t) + v_{SIG}(t)$$
$$\langle I(t)\rangle = I_{LO}(t) + i_{SIG}(t) \qquad (2.22)$$

Inclusion of $v_{SIG}(t)$ in the applied voltage in (2.7) requires additional terms in the time-dependent phase factor. While retaining only those terms to first order in the sideband voltage components v_m, the new Werthamer phase factor is found such that:

$$W(\omega') = \sum_{n=-\infty}^{\infty} J_n(\alpha)\left\{\delta(\omega' - n\omega) + \sum \frac{e}{2\hbar\omega_{m'}}\left[v_{m'}^* \delta(\omega' - n\omega - \omega_{m'}) - v_{m'}\delta(\omega' - n\omega + \omega_{m'})\right]\right\}$$

$$(2.23)$$

Inserting this result into (2.6) for the quasiparticle tunneling current, and again retaining only terms linear in the sideband voltages v_m, we find the admittance matrix elements that give the signal currents i_m in (2.20) to be

$$G_{mm'} = \frac{e}{2\hbar\omega_{m'}} \sum_{n,n'=-\infty}^{\infty} J_n(\alpha)J_{n'}(\alpha)\delta_{m-m',n'-n}\left\{\left[I_{dc}\left(V_0 + n'\hbar\omega/e + \hbar\omega_{m'}/e\right) - I_{dc}\left(V_0 + n'\hbar\omega/e\right)\right]\right.$$
$$\left. + \left[I_{dc}\left(V_0 + n\hbar\omega/e\right) - I_{dc}\left(V_0 + n\hbar\omega/e - \hbar\omega_{m'}/e\right)\right]\right\} \tag{2.24}$$

$$B_{mm'} = \frac{e}{2\hbar\omega_{m'}} \sum_{n,n'=-\infty}^{\infty} J_n(\alpha)J_{n'}(\alpha)\delta_{m-m',n'-n}\left\{\left[I_{KK}\left(V_0 + n'\hbar\omega/e + \hbar\omega_{m'}/e\right) - I_{KK}\left(V_0 + n'\hbar\omega/e\right)\right]\right.$$
$$\left. + \left[I_{KK}\left(V_0 + n\hbar\omega/e\right) - I_{KK}\left(V_0 + n\hbar\omega/e - \hbar\omega_{m'}/e\right)\right]\right\}. \tag{2.25}$$

Apparently $Y_{mm'}$ is seen to have real and imaginary parts, which depend on the reduced LO voltage α and dc I-V characteristic. The imaginary part, which is called "quantum susceptance", arises from the effects due to absorption or emission of particular numbers of photons during the tunneling process. In the classical limit, the imaginary part of $Y_{mm'}$ given by (2.25) vanishes and $Y_{mm'}$ is reduced to only the real part [9].

Once the elements of the admittance matrix $Y_{mm'}$ relating the small-signal voltages and currents at the various sideband frequencies have been determined, the analysis of mixer performance is straightforward. An arbitrary set of current generators $\{J_m\}$ placed at each sideband ω_m of the mixer will produce small-signal current and voltage components across the SIS junction satisfying

$$J_m = i_m + Y_m v_m$$
$$= \sum_m \left(Y_{mm'} + Y_m\delta_{mm'}\right)v_{m'}. \tag{2.26}$$

Inverting these equations, we can obtain the signal voltages produced by this arbitrary set of current generators as

$$v_m = \sum_m Z_{mm'}J_{m'}, \tag{2.27}$$

where, in matrix notation,

$$\|Z_{mm'}\| = \|Y_{mm'} + Y_m\delta_{mm'}\|^{-1}. \tag{2.28}$$

Now, $Y_1 = Y_S$, $J_1 = J_S$, $J_m = 0$ $(m \neq 0)$, $Y_0 = Y_L$ are assumed in Fig. 2.2. Y_S and Y_L are the

load admittance for the signal and for the output, respectively. Since the output voltage can be written in the form

$$v_0 = \sum_m Z_{0m} J_m = Z_{01} J_S,$$

(2.29)

the power down-converted and delivered in the output load (i.e., intermediate frequency output $P_0 = P_{IF}$) can be given by

$$P_{IF} = \frac{1}{2} G_L |v_0|^2 = \frac{1}{2} G_L |Z_{01}|^2 |J_S|^2.$$

(2.30)

The available power for the signal at the input is

$$P_S = \frac{|J_S|^2}{8 G_S}.$$

(2.31)

The conversion loss then becomes

$$L_C = \frac{P_S}{P_{IF}} = \frac{1}{4 G_S G_L |Z_{01}|^2}.$$

(2.32)

In these expressions, G_S and G_L represent the real parts of the source and load admittances Y_S and Y_L, respectively.

2.2.3 Noise analysis

The major noise sources in SIS mixers are the shot noise arising from the fluctuations of the LO current through the tunnel junction and the thermal noise generated by dissipative terminations at sideband frequency ports. The quantum fluctuations of the input signal, regard as the quantum limit of the detection, is commonly ignored in the noise analysis. While both types of noises are equalized as small-signal current sources connected in parallel with the junction, as illustrated in Fig. 2.3, the noise analysis can be carried out just as the small-signal analysis described

above.

The shot noise due to LO current tunneling through the barrier may be represented by a noise generator $\left[I(t) - \langle I(t) \rangle\right]$ placed in parallel with an idealized "noiseless" mixer, where $I(t)$ is the current operator for the junction. Although the large-signal tunneling current $I(t)$ is made up of components at the various harmonic frequencies of the LO signal, fluctuations over the average current $\langle I(t) \rangle = I_{LO}(t)$, which is given by (2.10), are random processes and its spectral density is therefore a continuum. The shot-noise current components at the sideband frequencies are converted into the IF output of the mixer. Tucker derived the shot-noise correlation matrix of LO-pumped tunnel junctions for the quantum theory of mixing. The matrix elements are given by

$$
\begin{aligned}
H_{mm'}^{s} = \left\langle I_{sm}' I_{sm'}'^{*} \right\rangle = e \sum_{n,n'=-\infty}^{\infty} J_n(\alpha) J_{n'}(\alpha) \delta_{m-m',n'-n} \\
\cdot \left\{ \coth\left[\beta\left(eV_0 + n'\hbar\omega + \hbar\omega_{m'}\right)/2\right] J_{dc}\left(V_0 + n'\hbar\omega/e + \hbar\omega_{m'}/e\right) \right. \\
\left. \coth\left[\beta\left(eV_0 + n\hbar\omega - \hbar\omega_{m'}\right)/2\right] J_{dc}\left(V_0 + n\hbar\omega/e - \hbar\omega_{m'}/e\right) \right\},
\end{aligned}
\tag{2.33}
$$

where β is designated as $1/kT$.

Regarding the thermal noise in SIS mixers, its mechanism and behavior are exactly the same as in classical mixers. The thermal-noise correlation matrix is diagonal and has elements as follows:

$$
H_{mm'}^{t} = \left\langle I_{tm}' I_{tm'}'^{*} \right\rangle = \begin{cases} \dfrac{4\hbar\omega_m \Delta f G_m}{\exp(\beta\hbar\omega_m)-1} & m = m' \\ 0 & m \neq m' \end{cases}
\tag{2.34}
$$

The total noise-correlation matrix can be written by

$$
H_{mm'} = H_{mm'}^{s} + H_{mm'}^{t}.
\tag{2.35}
$$

A detectable signal noise power is derived by considering the expectation value for the square of the LO noise current within the output bandwidth [9]:

$$P_{\text{det}} = kT_{mix}B = \frac{1}{4G_S|Z_{01}|^2} \sum_{m,m'} Z_{0m}Z_{0m'}^*H_{mm'} \,, \tag{2.36}$$

where T_{mix} is the total mixer noise temperature, which represents the thermal noise generated by dissipative elements and the shot noise generated by the combination of dc bias voltage and the LO waveform impressed across the junction.

2.3 Superconducting microstrip transmission line

At RF and microwave frequencies, normal metal circuits such as coaxial lines, hollow waveguides and microstrip transmission line, are widely used in consumer and industrial electronics. These have sufficiently low losses to be generally acceptable for use in systems operated at ambient temperature (e.g., 300 K). There are, however, important applications in terrestrial and space communication systems and ultra-low noise receivers, where exceptionally high performance is required. The attenuation and dispersion are the main factors limiting the technical achievement of normal metal circuits.

Superconducting microstrip transmission lines have extremely low conduction-loss characteristics below the gap frequency ($f_g = 2\Delta/h$). The reduction in loss is accompanied by lower heat production and greater transmission efficiency. The benefits for signal transmission include reduced signal attenuation and noise, and lower signal dispersion [10].

Figure 2.4 illustrates the geometry of a general microstrip transmission line and the equivalent circuit of a section of the line of differential length dz, which is made up of a distributed series impedance Z per unit length and a distributed shunt admittance Y per unit length. In practice, Z and Y can be expressed as

$$Z = R + j\omega L, Y = G + j\omega C, \qquad (2.37)$$

where R, G, L, and C are the distributed constants.

The propagation of a sinusoidal voltage $V(x,\omega)\exp(i\omega t)$ on a transmission line is governed by the differential equation

$$\frac{d^2 V}{dx^2} = \gamma^2 V, \qquad (2.38)$$

where γ is the propagation constant and is generally defined by

$$\gamma = \alpha + j\beta. \qquad (2.39)$$

The real part α in (2.39) is the attenuation constant and the imaginary part β is the phase constant. The characteristic impedance and the propagation constant line are given by

$$Z_0 = \sqrt{\frac{Z}{Y}} \qquad (2.40.1)$$

and

$$\gamma = \sqrt{ZY}. \qquad (2.40.2)$$

Given Z and Y, the transmission line, the propagation properties of transmission line can be completely characterized by Z_0 and γ.

In analyzing the superconducting microstrip line a lossless dielectric is assumed. Then the shunt admittance Y reduces to the capacitive component of a unit length of line and is given by

$$Y = i\omega \frac{\varepsilon \varepsilon_0 W}{s} K(W, s, d_1), \qquad (2.41)$$

where ε is the relative dielectric constant and ε_0 is the permittivity of free space. The series impedance is given by

$$Z = \frac{Z_{s1} + Z_{s2}}{WK(W, s, d_1)} + i\omega \frac{\mu_0}{WK(W, s, d_1)}, \qquad (2.42)$$

where μ_0 is the permeability of free space, and Z_{s1} and Z_{s2} are the surface impedances of

the strip and groundplane. $K(W,s,d)$ represents the fringe field factor introduced by Chang and $K(W,s,d)$ approaches to unity when the aspect ratio W/s [11]. The first term of (2.42) accounts for fields penetrating into the conductors and the second term is the inductance associated with magnetic fields in the dielectric region.

The surface impedance Z_s is given by [12]

$$Z_s(\omega) = \left(\frac{i\omega\mu_0}{\sigma}\right)^{1/2} \coth\left[(i\omega\mu_0\sigma)^{1/2}d\right],\tag{2.43}$$

where $\sigma = \sigma_1 - i\sigma_2$ is the complex conductivity. The complex conductivity can be calculated using the microscopic theory of superconductivity including the effects of the energy gap. This was extended from the BCS weak-coupling theory by Mattis and Bardeen to derive expression as follows [13]:

$$\frac{\sigma_1}{\sigma_n} = \frac{2}{\hbar\omega}\int_\Delta^\infty [f(E) - f(E + \hbar\omega)]g(E)dE + \frac{1}{\hbar\omega}\int_{\Delta-\hbar\omega}^{-\Delta}[1 - 2f(E + \hbar\omega)]g(E)dE\tag{2.44}$$

$$\frac{\sigma_2}{\sigma_n} = \frac{1}{\hbar\omega}\int_{\Delta-\hbar\omega,-\Delta}^{\Delta} \frac{[1 - 2f(E + \hbar\omega)][E^2 + \Delta^2 + \hbar\omega E]}{(\Delta^2 - E^2)^{1/2}[(E + \hbar\omega)^2 - \Delta^2]^{1/2}}dE,\tag{2.45}$$

where σ_n is the normal-state conductivity, $f(E)$ is the Fermi-Dirac (distribution) function expressed by (2.5), and

$$g(E) = \frac{E^2 + \Delta^2 + \hbar\omega E}{(E^2 - \Delta^2)^{1/2}[(E + \hbar\omega)^2 - \Delta^2]^{1/2}}.\tag{2.46}$$

The first integral in (2.44) represents the effect of the thermally excited quasiparticles, and the second integral in (2.44) accounts for the contribution of photon-excited quasiparticles and is zero for $\omega < 2\Delta$. Equation (2.46) describes the "kinetic inductance" of the surface caused by the response of the Cooper pairs and its lower limit is taken as Δ if $\omega < 2\Delta$.

References

[1] A. H. Dayem and R. J. Martin, "Quantum interaction of microwave radiation with tunneling between superconductors", *Phys. Rev. Lett.*, **8**, 246 (1962).

[2] P. K. Tien and J. P. Gordon, "Multiphoton process observed in the interaction of microwave fields with the tunneling between superconductor films", *Phys. Rev.*, **129**, 647 (1963).

[3] J. R. Tucker, "Quantum limited detection in tunnel junction mixers", *IEEE J. Quantum Electron.*, **15**, 1234 (1979).

[4] H. C. Torrey and C. A. Whitmer, *Crystal Rectifiers*, MTT Radiation Lab. Series, 15, New York: McGraw-Hill (1948).

[5] A. Jr. Uhlir, "The potential of semiconductor diodes in high-frequency communications", *Proc. IRE*, **46**, 1099 (1958).

[6] A. A. M. Saleh, *Theory of Resistive Mixers*, Cambridge, MA: MIT press (1971)

[7] D. N. Held and A. R. Kerr, "Conventional loss and noise of microwave and millimeter wave mixers: Part I-Theory", *IEEE Trans. Microwave Theory Tech.*, **26**, 49 (1978).

[8] N. R. Werthamer, "Nonlinear self-coupling of Josephson radiation in superconducting tunnel junctions", *Phys. Rev.*, **147**, 255 (1996).

[9] J. R. Tucker and M. J. Feldman, "Quantum detection at millimeter wavelengths", *Rev. Mod. Phys.*, **57**, 4, 1055 (1985).

[10] R. L. Kautz, "Picosecond pulses on superconducting striplines", *J. Appl. Phys.*, **49**, 1, 308 (1978).

[11] W. H. Chang, "The inductance of a superconducting strip transmission line", *J. Appl. Phys.*, **50**, 12, 8129 (1979).

[12] S. Ramo, J. R. Whinnery, and T. van Duzer, *Fields and Waves in Communication Electronics*, 2nd edition, New York, NY: Jone Wiley & Sons (1984).

[13] D. C. Mattis and J. Bardeen, "Theory of the anomalous skin effect in normal and superconducting materials", *Phys. Rev.*, **111**, 412 (1958).
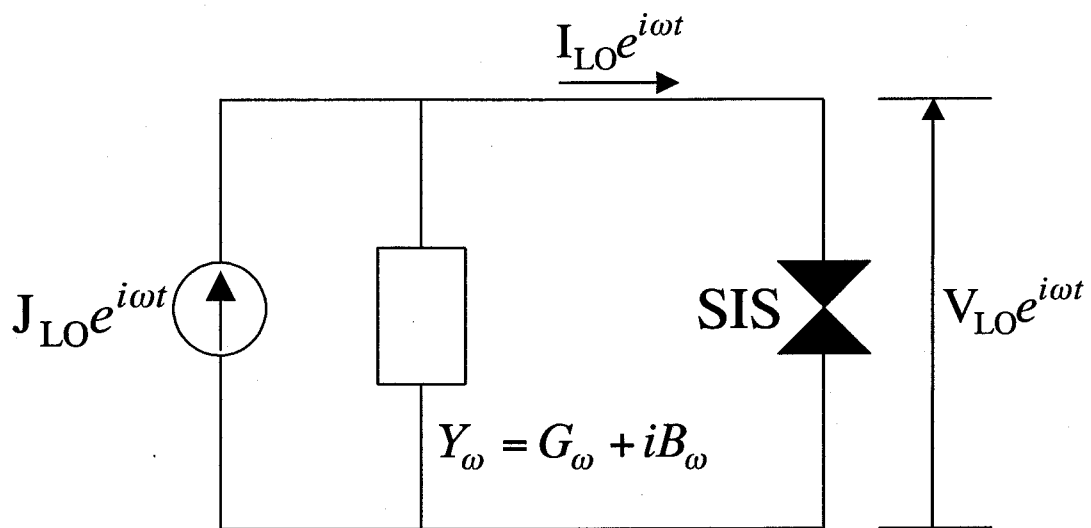
Figure 2.1 Large-signal equivalent circuit for a SIS mixer. The LO is applied at frequency ω. All higher harmonics of LO are assumed to be short circuited.
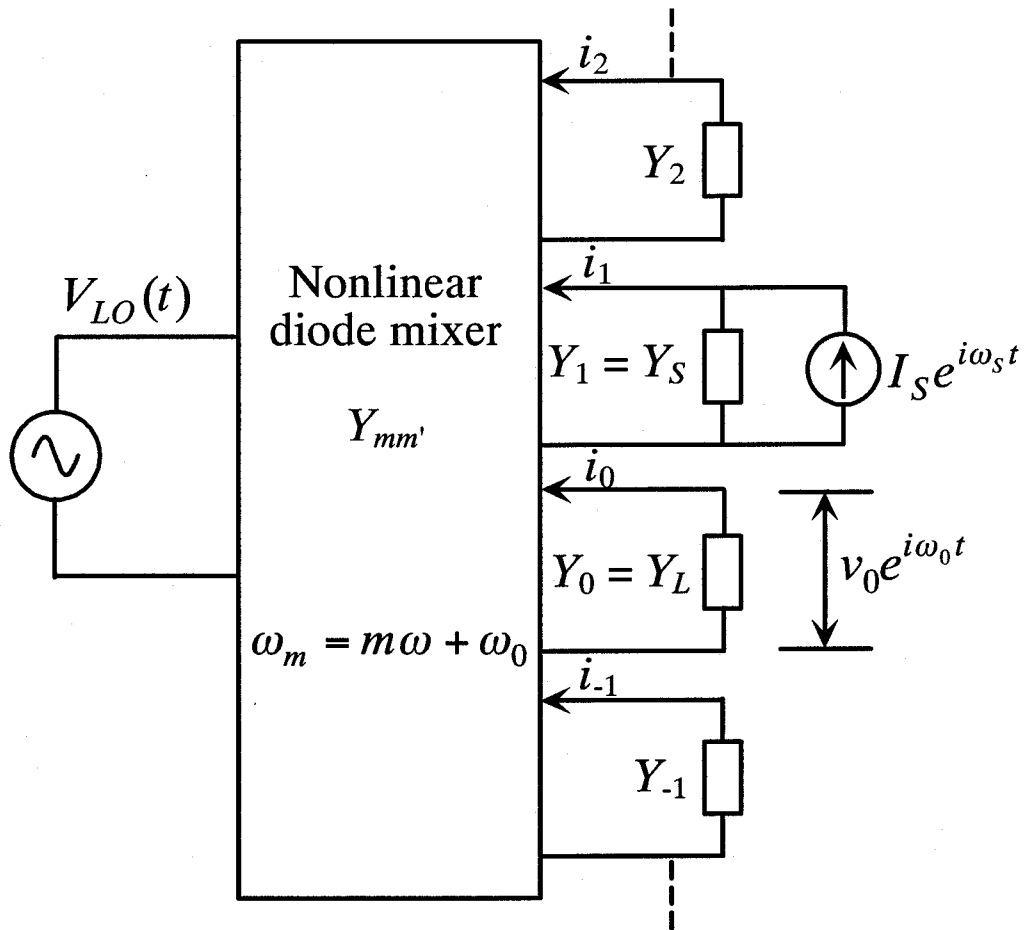
Figure 2.2 Multiport representation of a general fundamental mixer, with applied LO frequency w, signal frequency $\omega_S = \omega_1$, and IF output at ω_0.
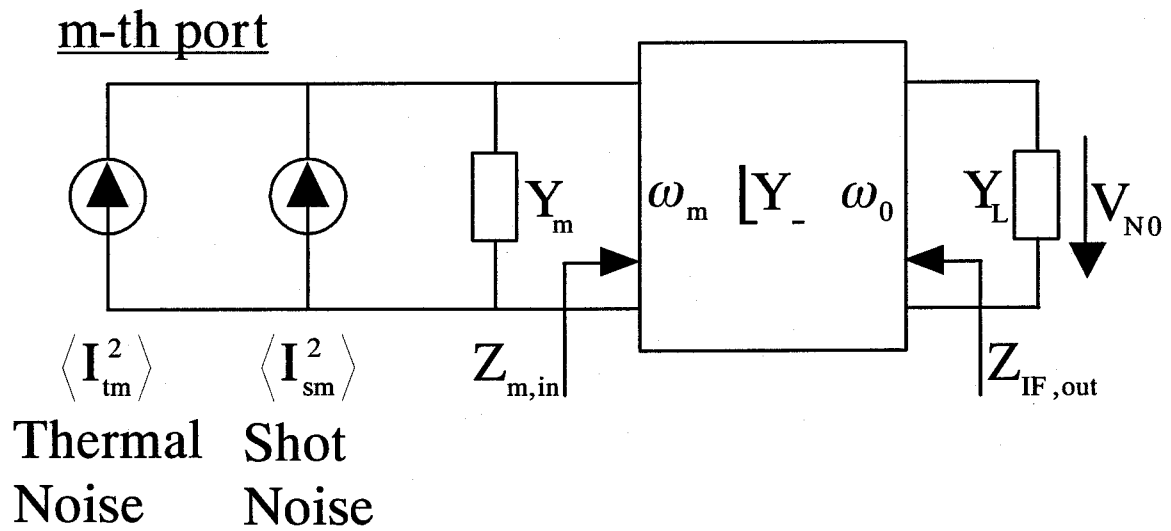
m-th port

Figure 2.3 Noise equivalent circuit of a general mixer, with a shot-noise and thermal-noise current sources connected in parallel at the m-th port (the same form at other ports). Notice that the thermal-noise components at the input and output ports should be excluded while these two ports look at rather than noises but useful signals.
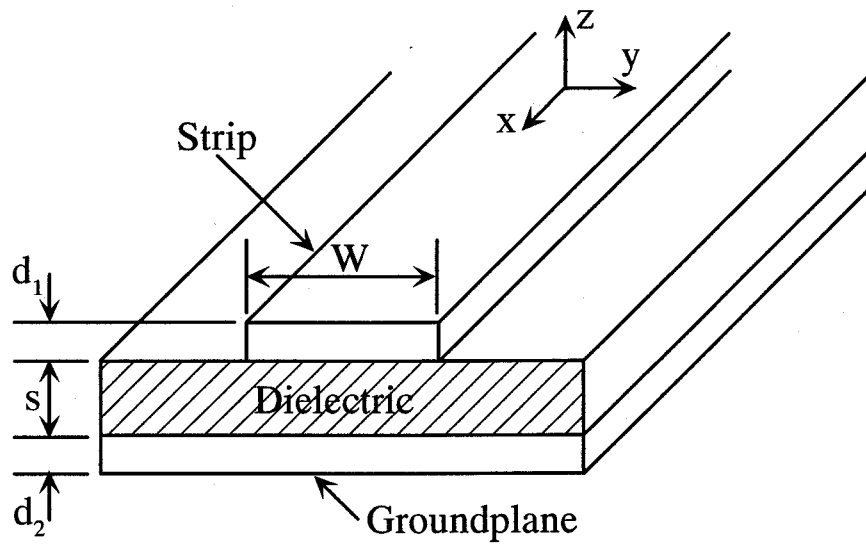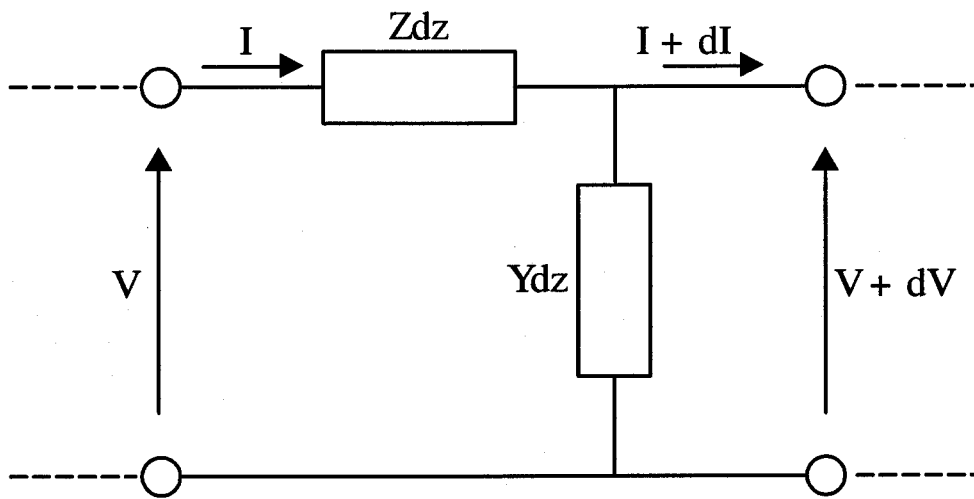
Figure 2.4 (a) Geometry of a microstrip line. (b) General transmission-line equivalent circuit in differential length *dz*.

Chapter III

Historical view of SIS mixers

3.1 SIS junction and tuning circuit

In general, an SIS junction has large geometrical capacitance since it consists of two superconducting layers separated by a thin insulating layer with relatively high dielectric constant. Electronically the junction is represented by a normal-state resistance R_n with a geometrical capacitance C_j in parallel, as shown in Fig. 3.1. High frequency signals fed to the junction would be short-circuited by the capacitance. To achieve waveguide-type SIS mixers with high sensitivity performance, the capacitance must be removed by adding an appropriate tuning circuit. Traditionally, mechanical tuning circuit with a backshort and a stub-tuner is used. By this tuning system extremely broadband operation has been achieved [1]. For real receivers, however, mechanically tuned mixers are inconvenient to operation and their performance will be degraded after a period of operation. Such problems will be much more pronounced in submillimeter-wave SIS mixers and complex systems such as interferometer arrays and multibeam receivers [2]. Hence it is highly desirable to develop SIS mixers with tuneless or fixed tuned SIS mixers [3].

3.2 Various integrated tuning circuits for SIS mixers

In tuneless or fixed tuned waveguide-type SIS receivers, tuning circuits integrated on SIS mixer chip are necessary to resonate out the geometrical capacitance and to match the impedance of the junction to that of the input waveguide, in which the height

is reduced in order to lower the impedance. Almost all of the circuit so far proposed for tuning out the capacitance fall into three broad categories as shown in Fig. 3.2.

The first category is a circuit in which a tuning inductance in series with a dc-blocking capacitor C_b is located in parallel with the SIS junction, as shown in Fig. 3.2(a) [4]. The input impedance at the resonance becomes R_n (usually several tens ohms), which is relatively easy to match the impedance of the input waveguide, compared with the other categories. The blocking capacitance can be implemented by a quarter-wavelength radial or open stub. However, in order to avoid reducing the bandwidth, the RF impedance of this blocking capacitor must be kept small, $Z_b(\omega)$ << $1/\omega C_j$, namely, the blocking capacitance must be made large in comparison to the junction geometrical capacitance C_j in order to achieve the maximum bandwidth for the tuning circuit. This constraint will make a difficulty to satisfy in practice for submillimeter wavelengths.

The second category is shown in Fig. 3.2(b), in which a series inductance is used [5]. This is commonly referred to as an "end-loaded" stub. The difficulty presented by this circuit is that it also acts as an impedance transformer, producing a real impedance on the order of $R_n/(\omega R_n C_j)^2$ [6]. The input impedance of the circuit becomes quite low when the $\omega R_n C_j$ is large. A multisection quarter-wavelength transformer is then needed to match this quite low impedance to the input-waveguide impedance. The transformer will reduce the bandwidth and make the circuit more susceptible to losses, especially at submillimeter wavelengths for which a larger transformation factor will be needed.

The third category incorporates two SIS junctions separated by a tuning inductance, as shown in Fig. 3.2(c), and is called a "parallel connected twin junctions (PCTJ)" [7, 8] or a "two-junction tuning circuit" [6], [9, 10]. The PCTJ circuit does not need a

dc-blocking capacitor. The input impedance at resonance is just equal to half of the normal-state resistance, $R_n/2$, which is relatively easy to match to the input waveguide. The circuit has a tuning inductance twice of that in magnitude in Fig. 3.2(a). A larger inductance produces merit concerning fabrication tolerance.

3.3 Bandwidth characteristics of SIS mixers

Bandwidth characteristics of tuning circuits (parallel inductor, end-load, and PCTJ) described in previous section roughly defined by $1/\omega R_n C_j$ ($= \Delta\omega/\omega_0$), which is approximately equal to the Q-factor for those tuning circuits. The $\omega R_n C_j$ product is actually independent of the dimension of a junction and depends only upon the thickness of the tunnel barrier, namely, the junction critical current density. The relation between $\omega R_n C_j$ product and critical current density J_c is represented by

$$J_c = \omega C_s \frac{I_c R_n}{\omega R_n C_j},$$ (3.1)

where C_s is the specific capacitance of an SIS junction and is assumed to be 90 fF/μm^2 throughout this thesis [11]. The $I_c R_n$ product is 2.0 mV in high-quality Nb/AlOx/Nb tunnel junctions. Figure 3.3 shows the relation between the relative bandwidth ΔB and the critical current density. To achieve SIS mixers with broader bandwidths, higher critical current densities, which are namely smaller $\omega R_n C_j$ products, are required. The critical current density, in addition, must be increased to keep a constant bandwidth as the signal frequency becomes high. Since normal-state resistances are smaller as critical current densities are increased, junctions with smaller dimensions are required. This brings a difficulty in the junction fabrication. Unfortunately, it is usually difficult to fabricate SIS junctions with high critical current densities, for example, 10 kA/cm^2 for

Nb junctions, and the high critical current density may cause various disadvantages, such as large sub-gap leakage current, increase of sub-harmonic gap structure and a reduction of the yields of junctions in the fabrication [12]. The problem on critical current density will become more remarkable as the signal frequencies increase.

The noise temperature of some of recently developed broadband SIS receivers in the 200 GHz band are plotted as a function of frequency in Fig. 3.4 [1], [13]. It can be seen that the bandwidth corresponded to Fig. 3.3 has been obtained. The SIS mixer with series array is less dependent on the critical current density, but a complicated RF matching network has been added with the SIS junctions [13].

3.4 SIS mixers with distributed junction arrays

Two different types of broadband SIS mixers having junctions with low critical current density have been proposed. One is an SIS mixer made of a nonlinear thin-film transmission line proposed by Tong [14, 15]. It has been shown that the required critical current density of this type of SIS mixer to achieve a reasonable bandwidth can be lowered in contrast with the conventional SIS mixers as shown in Fig. 3.2. The receiver noise temperature is frequency independent over a broad bandwidth. However, this type of SIS mixer has a very small line width (~ 0.1 μm) and requires the use of electron-beam lithography for junction fabrication.

The other type of mixer is SIS mixers with distributed junction arrays proposed by Shi [16, 17]. The distributed junction array consists of a number of junctions with identical dimensions homogeneously placed on a superconducting microstrip, as shown in Fig. 3.5. This type of SIS mixer is possible to fabricate the junction using the conventional optical lithography technique and can overcome the difficulty of

fabrication of the former. Since the distributed junction arrays are just the extension of PCTJs, the mixing properties can theoretically evaluate based on the analysis for PCTJ [6]. In this section, the large- and small-signal analyses for distributed junction arrays are summarized and the mixing properties are described.

3.4.1 Mixing theory for distributed junction arrays

3.4.1.1 Large-signal analysis

To understand the distribution of the LO voltage in a distributed junction array, it is necessary to implement a large-signal analysis. The equivalent circuit of k-th SIS junction for a distributed junction array with N-junctions is illustrated in Fig. 3.6, in which the tuning superconducting microstrip between two junctions is represented by a chain matrix $[C]$. This chain matrix is defined by

$$[C] = \begin{bmatrix} C_{11} & C_{12} \\ C_{21} & C_{22} \end{bmatrix} = \begin{bmatrix} \cosh(\gamma l) & Z_0 \sinh(\gamma l) \\ Z_0^{-1} \sinh(\gamma l) & \cosh(\gamma l) \end{bmatrix}, \tag{3.2}$$

where l, γ and Z_0 are the length of the microstrip between every two junctions, the propagation constant and characteristic impedance of the microstrip, respectively. The LO voltage V_p^{k-1} applied to and the LO current I_p^{k-1} flowed out the port $(k-1)$, can be written by the following equations:

$$V_p^{k-1} = C_{11,p} V_p^k + C_{12,p} \left(I_p^k + I_{j,p}^k + i\omega C_j V_p^k \right)$$
$$I_p^{k-1} = C_{21,p} V_p^k + C_{22,p} \left(I_p^k + I_{j,p}^k + i\omega C_j V_p^k \right), \tag{3.3}$$

where V_p^k and I_p^k denote the LO voltage and current at port k, respectively, and $I_{j,p}^k$ is the LO current induced in the k-th junction given by (2.12). Apparently the LO voltage V_p^k may be different from V_p^{k-1} in both magnitude and phase. Notice that there is a boundary condition that I_p^k is equal to zero at $k = N$ (i.e., at last junction). The LO

voltage developed to each junction can be calculated using (3.3), once the LO voltage across the last junction is determined.

3.4.1.2 Small-signal analysis

The small-signal circuit of the k-th junction at m'-th sideband, including its shot-noise current source and an equivalent one representing the shot noise due to all the following junctions, is illustrated in Fig. 3.7. $I_{s,m'}^k$ is the shot-noise current of k-th junction at m'-th sideband and $I_{se,m'}^k$ is the total noise current at port k at m'-th sideband. It is assumed that only the small-signal voltage $V_{m'}$ at the m'-th sideband is developed to this junction. The small-signal voltage at port (k-1) at the m'-th sideband is then given by

$$V_{m'}^{k-1} = C_{11,m'}V_{m'}^k + C_{12,m'}\left(I_{m'}^k + I_{j,m'}^k + i\omega_{m'}C_jV_{m'}^k\right) \tag{3.4}$$

and the small-signal current at port (k-1) induced at the m-th sideband by

$$I_m^{k-1} = C_{21,m}V_{m'}^k\delta_{mm'} + C_{22,m}\left(I_m^k + I_{j,m}^k + i\omega_mC_jV_{m'}^k\delta_{mm'}\right). \tag{3.5}$$

The equivalent conversion admittance matrix at port (k-1) is therefore represented by

$$Y_{mm',e}^{k-1} = \frac{C_{21,m}\delta_{mm'} + C_{22,m}\left(Y_{mm',e}^k + Y_{mm'}^k + i\omega_mC_j\delta_{mm'}\right)}{C_{11,m'} + C_{12,m'}\left(Y_{m'm',e}^k + Y_{m'm'}^k + i\omega_{m'}C_j\right)}, \tag{3.6}$$

where Y_{ij}^k is the conversion admittance matrix of the k-th junction given by (2.21) and $Y_{ij,e}^k$ is the equivalent conversion admittance matrix at port k.

3.4.1.3 Noise analysis

The equivalent noise circuit at port (k-1) at the m'-th sideband is illustrated in Fig. 3.8. According to the theory of noisy fourpoles [18], the two shot-noise current sources

in Fig. 3.7 can be represented by a noise voltage source E_m^{k-1} and a noise current source I_m^{k-1} in parallel with the input admittance seen before the chain matrix. Then, the magnitudes of the two equivalent noise sources are expressed as

$$E_{m'}^{k-1} = C_{12,m'}\left(I_{s,m'}^k + I_{se,m'}^k\right)$$
$$I_{m'}^{k-1} = C_{22,m'}\left(I_{s,m'}^k + I_{se,m'}^k\right). \tag{3.7}$$

The total noise current at port (k-1) at m'-th sideband is therefore given by

$$I_{se,m'}^{k-1} = E_{m'}^{k-1}Y_{in,m'}^{k-1} - I_{m'}^{k-1}$$
$$= \left(C_{12,m'}Y_{m'm',e}^{k-1} - C_{22,m'}\right)\left(I_{s,m'}^k + I_{se,m'}^k\right), \tag{3.8}$$

where $Y_{in,m'}^{k-1}$ is the input impedance seen before the chain matrix at the m'-th sideband and corresponds to (3.6). The noise correlation matrix of this equivalent noise current source can be written in the form

$$H_{mm',e}^{k-1} = C_{e,m}C_{e,m'}^*\left(H_{mm'}^k + H_{mm',e}^k\right), \tag{3.9}$$

where $H_{mm'}^k$ and $H_{mm',e}^k$ are the shot-noise correlation matrix for the k-th junction and the equivalent shot-noise correlation matrix at port k, respectively, $C_{e,m}$ is a transfer factor defined as

$$C_{e,m} = C_{12,m}Y_{mm,e}^k - C_{22,m}. \tag{3.10}$$

3.4.2 Mixing properties of distributed junction arrays

Using the quantum theory of mixing together with the equivalent circuit model described in the previous section, the mixing properties of the distributed junction arrays can be calculated in the frequency range from 190 to 300 GHz. As examples, the calculations were implemented for the distributed junction arrays with two (i.e., PCTJ), five and ten junctions. All the junctions of those arrays were assumed to have the same

41

critical current density as 3 kA/cm^2, which is relatively low value for Nb junctions, that corresponds to a $\omega R_n C_j$ product of about eight at 230 GHz. Therefore, a sharp junction I-V characteristic shown in Fig. 3.9, in which the ratio of the sub-gap resistance at 2.0 mV to the normal-state resistance is around 20, was employed in the calculations. In the program for the calculation of the mixing properties, the I-V characteristic shown in Fig. 3.9 is automatically transformed to that for the SIS junctions used in the calculations. The flow chart of the program is shown in Fig. 3.10. The dimensions of junctions and the spacings between adjacent junctions were assumed to be 1.5 μm^2 and 67 μm (60 μm in the case of PCTJ), respectively. The width of the superconducting microstrip was assumed to be 6.0 μm, which corresponds to the characteristic impedance of 10.9 Ω, following to the analysis of superconducting microstrip described in Chapter II. The equivalent normal-state resistance of the distributed junction arrays is given by R_n/N, where N is the number of junctions. The RF termination normalized to the equivalent normal-state resistance was assumed to be unity over the frequency band. An intermediate frequency (IF) and IF termination were set to be 1.5 GHz and 50 Ω that corresponds to the input resistance of general IF amplifier, respectively.

Figure 3.11 shows the input return losses and RF impedance at the input port of the arrays with two, five, and ten junctions. The RF input impedance is normalized to the equivalent normal-state resistance of each array. It is found from Fig. 3.11 that the diameter of the circle of an impedance locus on a Smith chart is small and the locus of the normalized impedance is concentrated around unity, as the number of junction is increased.

Figure 3.12 shows the calculated single-sideband (SSB) mixer noise temperature and conversion gain as a function of frequency. Note here that the dc bias and LO

42

voltages across the arrays were optimized with respect to the receiver noise temperature at each frequency by assuming a noise temperature of an IF amplifier of 10 K. It is found from this figure that the bandwidth of PCTJ is limited by $1/\omega R_n C_j$ as described in Sec. 3.3 and the relative bandwidth is about 12%. It is obviously visible that the overall bandwidth performance of distributed junction arrays is improved immensely as the number of junctions is increased, in spite of the same $\omega R_n C_j$ product. The distributed junction array composed of N junctions has N-1 resonance frequencies at where geometrical capacitances of junctions are completely resonated out, as shown in Fig. 3.5. The lower frequency f_{r1} is determined by the length of the superconducting microstrip and the upper frequency $f_{r(N-1)}$ is determined by the spacing between the adjacent junctions. The bandwidth centered at a resonance frequency is characterized by $1/\omega R_n C_j$. Therefore even low critical current density the broadband operation can be obtained in the distributed junction arrays. The frequency characteristics of the distributed junction arrays resemble that of LC low-pass filters. However, there is a serious problem in the distributed junction arrays. It is that a very large capacitance will appear at frequencies between adjacent resonance-frequencies. This large capacitance may cause the degradation of input coupling efficiency and may increase noise temperature. In practice, it is shown from Fig. 3.12 that a very large increase in noise temperature is observed at several frequencies and the conversion gain is considerably decreased near those frequencies in the distributed junction arrays.

The large increase in noise can be also seen in the experimental result by Shi *et al.* [16]. In the result for the distributed junction array with ten junctions, the minimum double-sideband (DSB) noise temperature is 95 K at 485 GHz ($4hf/k$), but a larger noise than 200 K is observed at any frequencies. In the practical applications, the large

increase in noise should reduce sufficiently.

References

[1] J. W. Kooi, M. Chan, T. G. Phillips, B. Bumble, and H. G. LeDuc, "A low noise 230 GHz heterodyne receiver employing .25 μm^2 area Nb/AlOx/Nb tunnel junctions", *IEEE Trans. Microwave Theory and Tech.*, **40**, 5, 812 (1992).

[2] K. Sunada, C. Yamaguchi, N. Kuno, and N. Ukita, "Development and first results of NRO 25-BEam Array Receiver System (BEARS)", *ASP Conference Series*, Tucson (1999).

[3] K. Sunada, R. Kawabe, and J. Inatani, "Tunerless mixer mount for an SIS 80-120 GHz receiver", *Int. J. Infrared & MM Waves*, 14, 1251 (1993).

[4] A. R. Kerr, S. -K. Pan, and M. J. Feldman, "Integrated tuning elements for SIS mixers", *Int. J. Infrared & MM Waves*, **9**, 203 (1988).

[5] T. H. Büttgenbach, H. G. LeDuc, P. D. Maker, and T. G. Phillips, "A fixed tuned broadband matching structure for submillimeter SIS receivers", *IEEE Trans. Appl. Supercond.*, **2**, 165 (1992).

[6] J. Zmuidzinas, H. G. LeDuc, J. A. Stern, and S. R. Cypher, "Two-junction tuning circuits for submillimeter SIS mixers", *IEEE Trans. Microwave Theory and Tech.*, **42**, 698 (1994).

[7] T. Noguchi, S. -C. Shi, and J. Inatani, "Parallel connected twin junctions for millimeter and submillimeter wave mixers: analysis and experimental", *IEICE Trans. Electron.*, **E-78**, 481 (1995).

[8] S. -C. Shi and T. Noguchi, "Low-noise superconducting receivers for millimeter and

submillimeter wavelengths", *IEICE Trans. Electron.*, **E81-C**, 1584 (1998)

[9] V. Y. Belitsky and M. A. Tarasov, "SIS junction complete reactance compensation", *IEEE Trans. Magn.* **27**, 2638 (1991).

[10] S. W. Jacobsson, V. Y. Belitsky, L. V. Filippenko, S. A. Kovtonjuk, V. P. Koshelets, and E. L. Kollberg, "Quasi-optical 0.5 THz receiver with twin junction tuning circuit", *Proc. 18th Int. Conf. on IR and MM Waves*, Colcheester, UK, **SPIE-2104**, 267 (1993).

[11] The specific capacitance of Nb/AlOx/Nb tunnel junction was estimated in Nobeyama Radio Observatory, National Astronomical Observatory, Japan.

[12] A. W. Kleinsasser, F. M. Rammo, and M. Bhushan, "Degradation of superconducting tunnel junction characteristics with increasing barrier transparency", *Appl. Phys. Lett.*, **62**, 1017 (1993).

[13] A. R. Kerr, S. -K. Pan, A. W. Lichtenberger, and H. H. Huang, "A tunerless SIS mixer for 200-280 GHz with low output capacitance and inductance", *Proc. 9th Int. Symp. Space Terahertz Technology*, Pasadena, USA, 195, March (1998).

[14] C. E. Tong, R. Blundell, B. Bumble, J. A. Stern, and H. G. LeDuc, "Quantum limited heterodyne detection in superconducting nonlinear transmission lines at sub-millimeter wavelengths", *Appl. Phys. Lett.*, **67**, 1304 (1995).

[15] C. E. Tong, L. Chen, and R. Blundell, "Theory of distributed mixing and amplification in a superconducting quasi-particle nonlinear transmission line", *IEEE Trans. Microwave Theory and Tech.*, **45**, 1086 (1997).

[16] S. -C. Shi, T. Noguchi, and J. Inatani, "Analysis of the bandwidth performance of SIS mixers with distributed junction arrays", *Proc. 8th Int. Symp. Space Terahertz Technology*, Boston, USA, 81, March (1997).
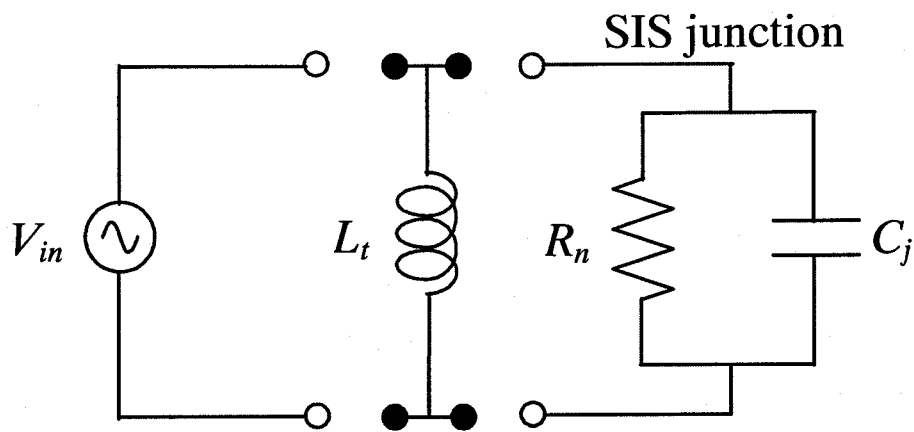
[17] S. -C. Shi, T. Noguchi, J. Inatani, Y. Irimajiri, and T. Saito, "Experimental results of

SIS mixers with distributed junction arrays", *IEEE Microwave and Guided Wave Lett.*, **8**, 381, (1998).

[18] H. Rothe and W. Dahlke, "Theory of noisy fourpoles", *Proc. IRE*, **44**, 811 (1956).
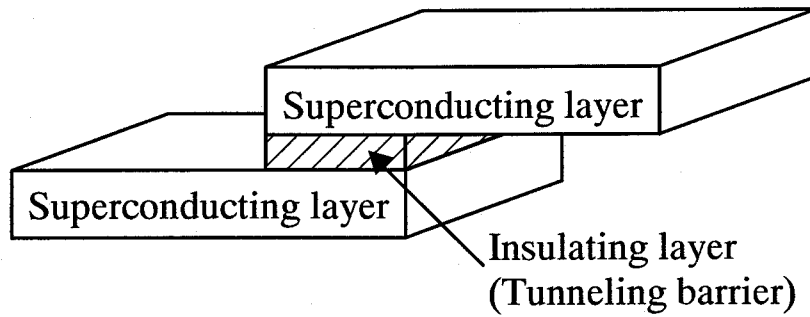
Figure 3.1 (a) Schematic view of an SIS junction. (b) The electrical equivalent circuit for an SIS junction. An inductor is added with the junction in order to cancel out the geometrical capacitance C_j leaving only the normal-state resistance R_n.
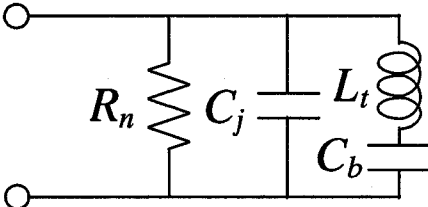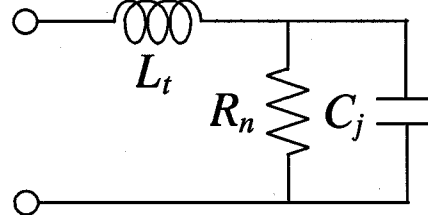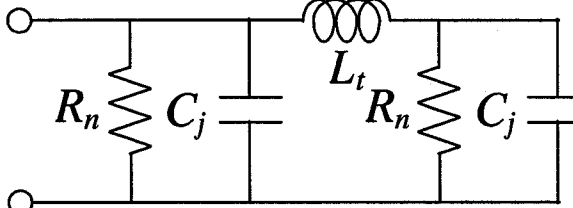
	Tuning inductance	Input impedance	Fabrication
(a)	$\dfrac{1}{\omega_0^2 C_j}$	R_n	difficult
(b)	$\dfrac{1}{\omega_0^2 C_j}$	$\dfrac{R_n}{\left(\omega R_n C_j\right)^2 + 1}$	easy
(c)	$\dfrac{2}{\omega_0^2 C_j}$	$\dfrac{R_n}{2}$	easy

Figure 3.2 Equivalent circuit models and properties of three types of general integrated tuning circuits for the SIS junction: (a) parallel inductance, (b) end-load, and (c) PCTJ.
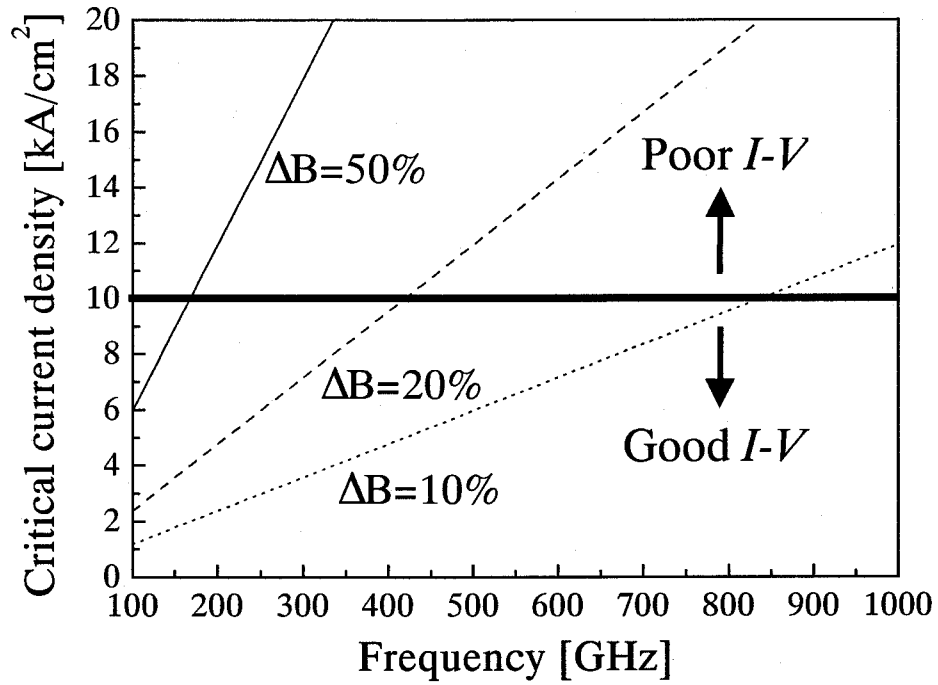
Figure 3.3 Critical-current density dependence of the relative bandwidth of general tuning circuits (parallel inductance, end-load, and PCTJ). For Nb-based SIS junctions, the junction quality degrades suddenly at the critical current densities above 10 kA/cm^2.
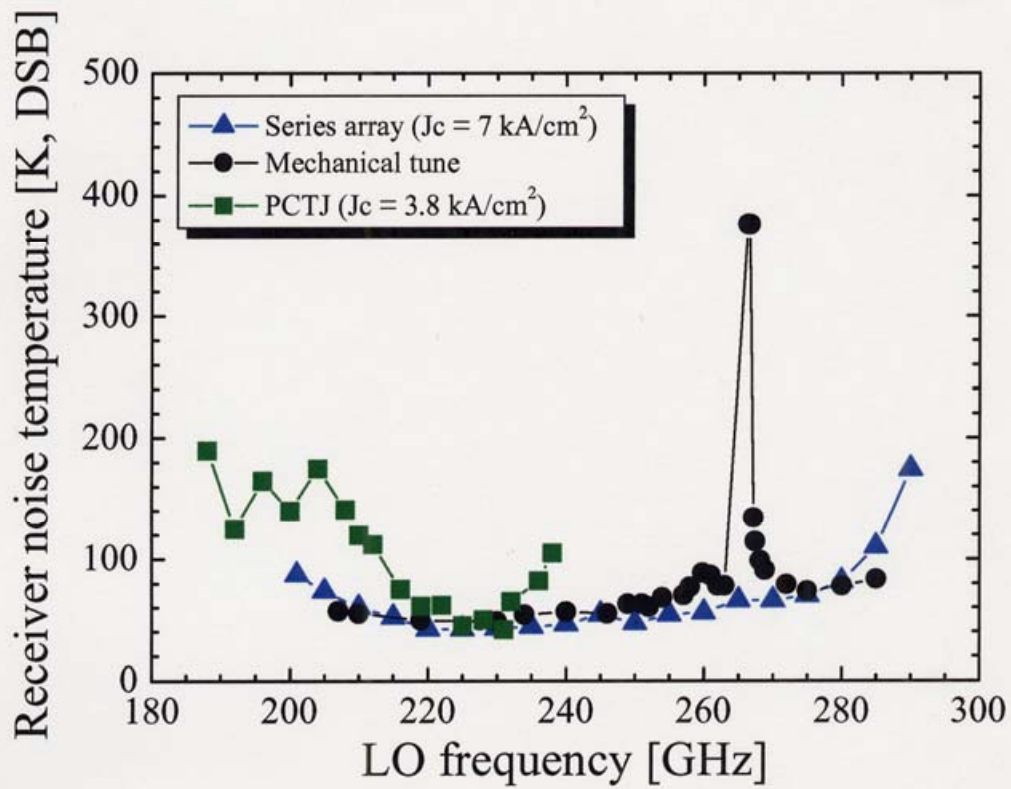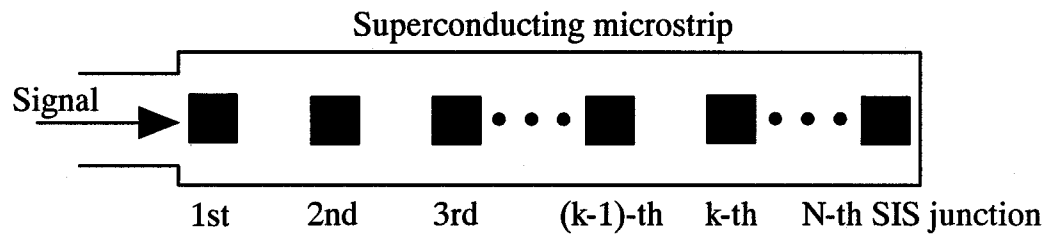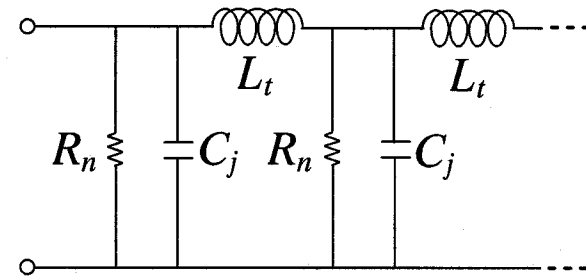
Figure 3.4 Receiver noise temperatures of recently developed SIS receivers in the 200 GHz band.
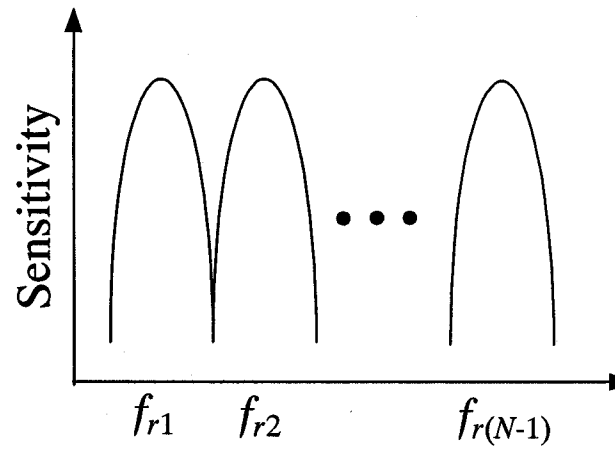
Figure 3.5 (a) Schematic representation of a distributed junction array with N junctions. (b) The equivalent electrical circuit between two junctions. (c) Resonance property of a distributed junction array.
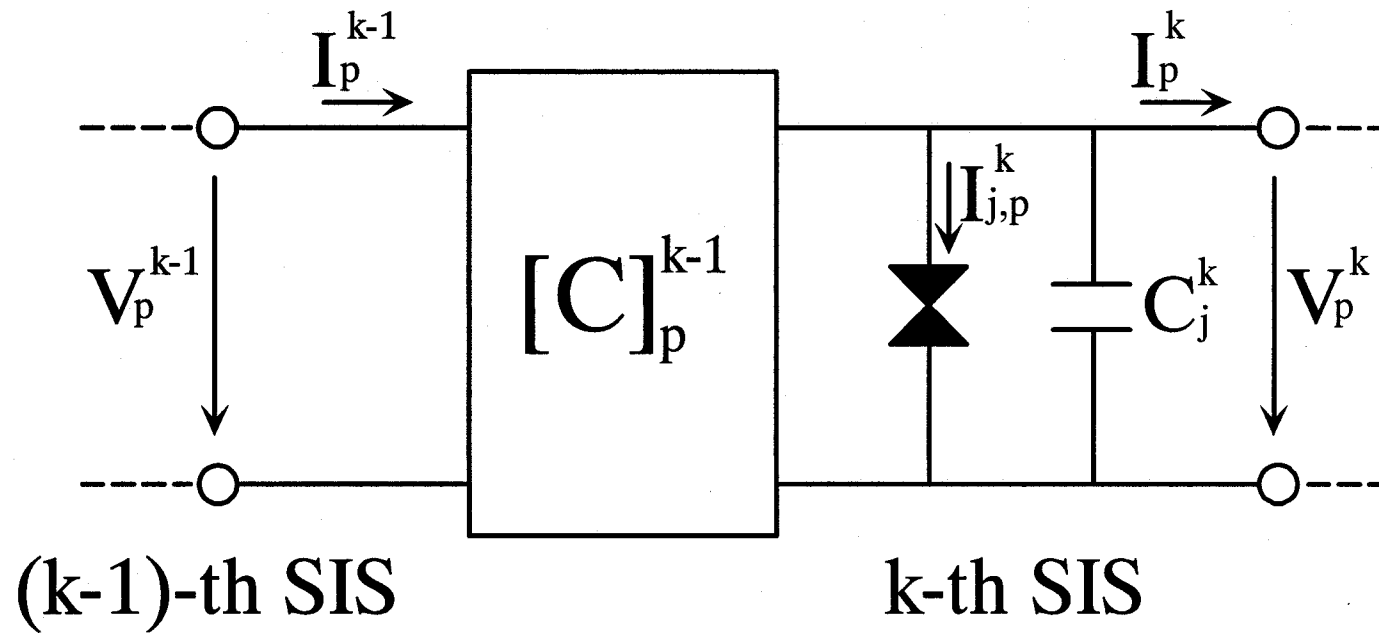
Figure 3.6 Large-signal equivalent circuit for the k-th junction and its preceding tuning element (described by a chain matrix $[C]$).
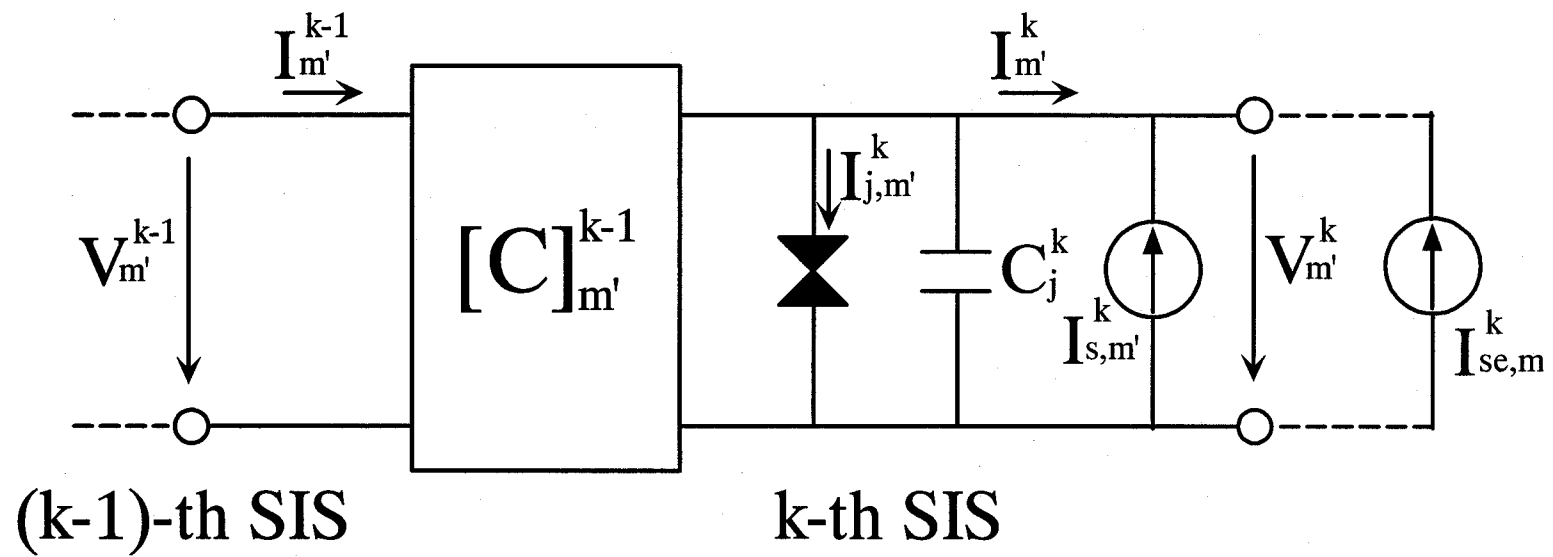
Figure 3.7 Small-signal equivalent circuit for the k-th junction and its preceding tuning element at m'-th sideband including the shot-noise current sources connected in parallel with the SIS junction.
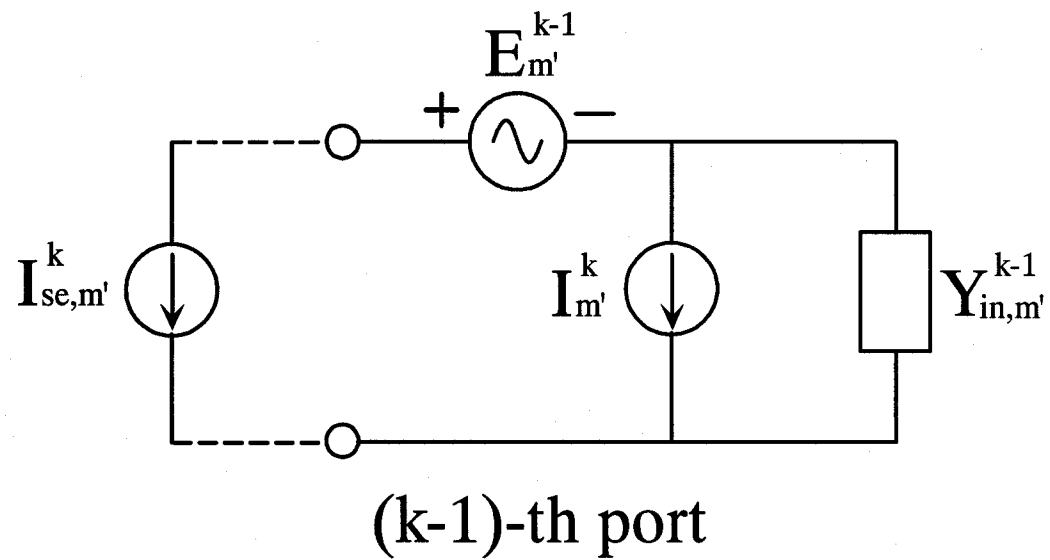
Figure 3.8 Noise equivalent circuit at port (*k*-1), representing all the shot-noise sources due to the *k*-th and following junctions.
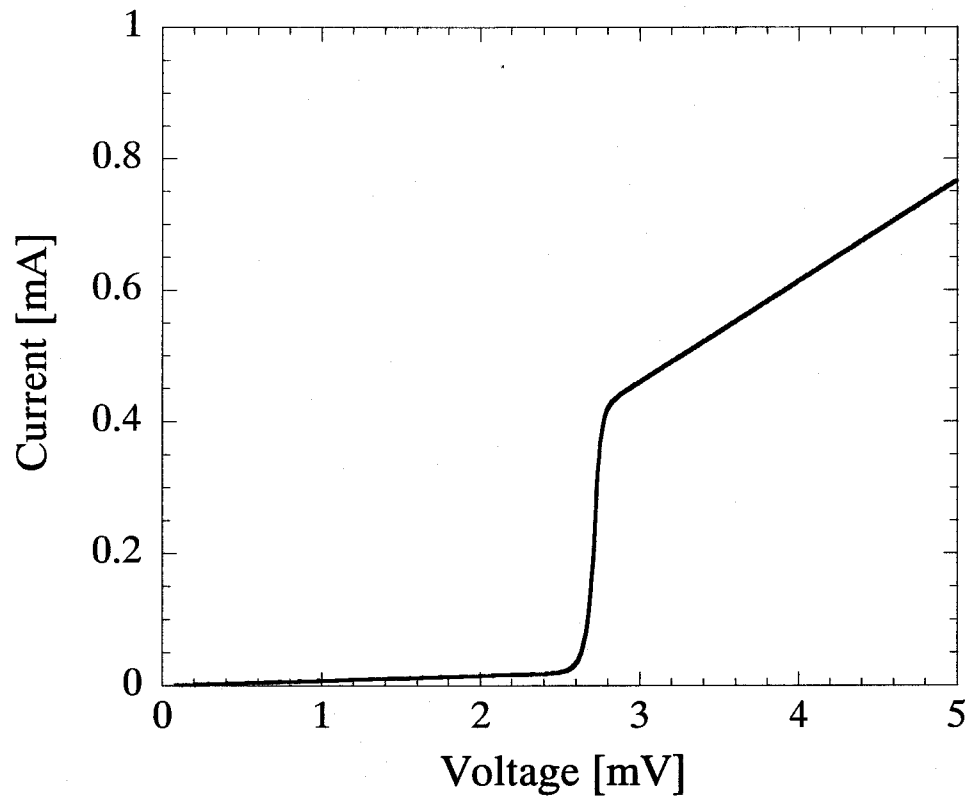
Figure 3.9 Junction DC I-V characteristic employed in the calculations of the mixing properties for distributed junction arrays. The ratio of sub-gap resistance at 2.0 mV to the normal-state resistance is around 20.
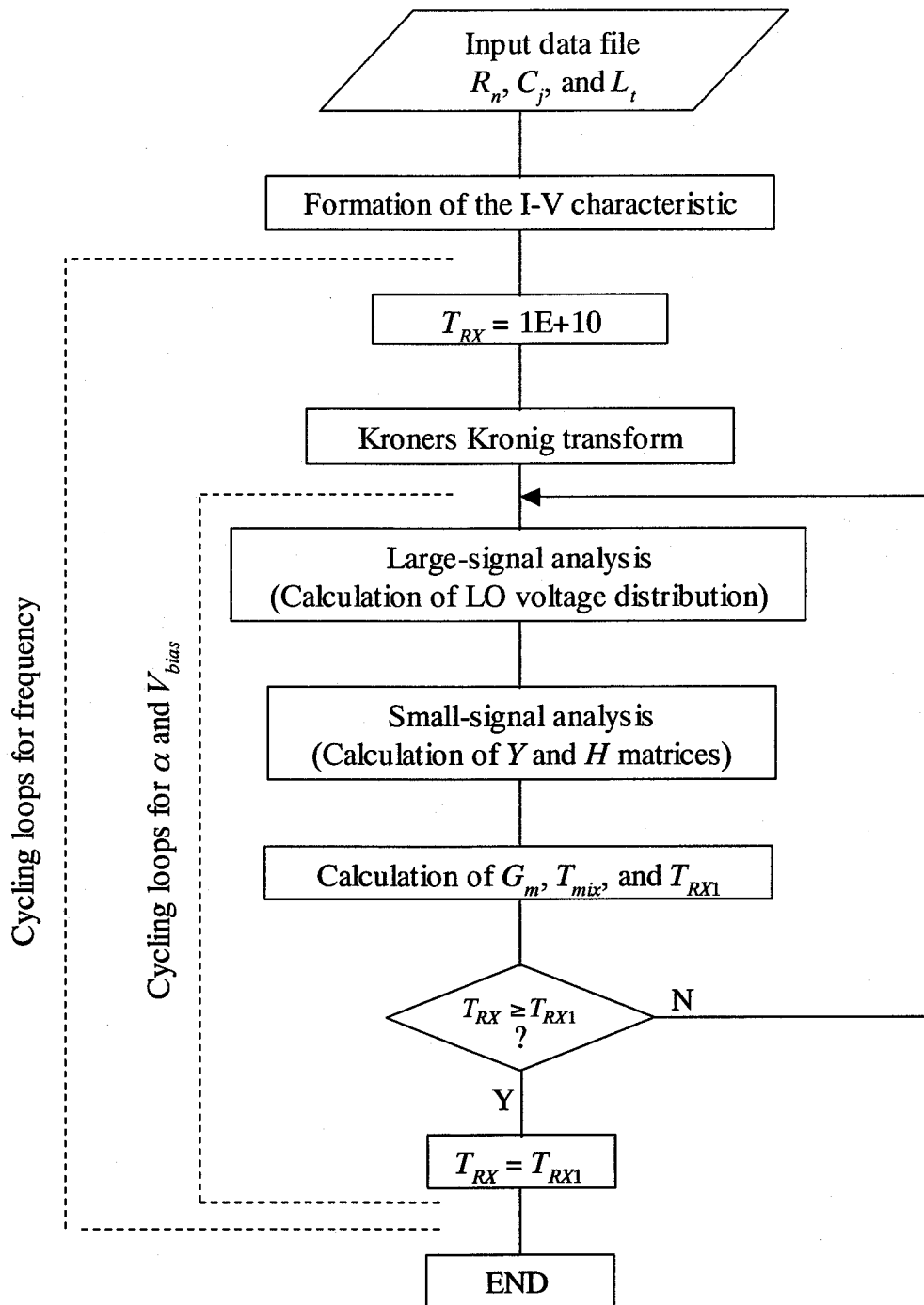
Figure 3.10 Flow chart of the program for the calculation of the mixing properties.
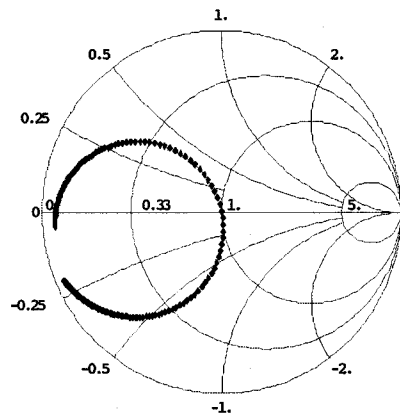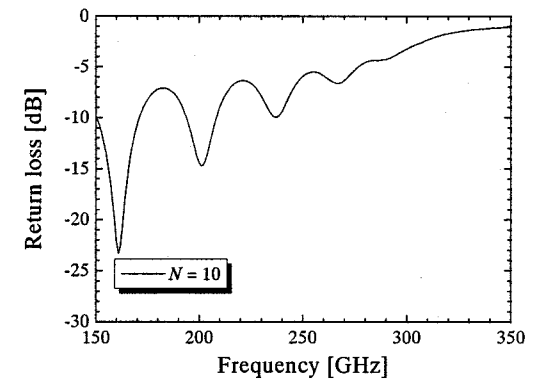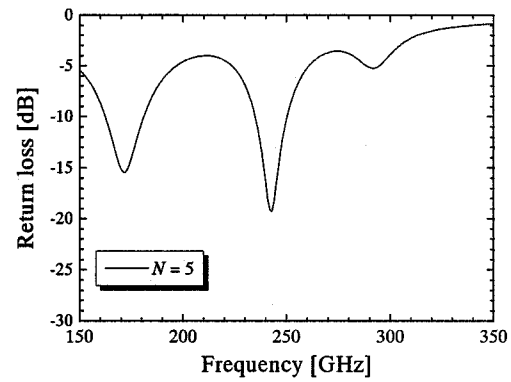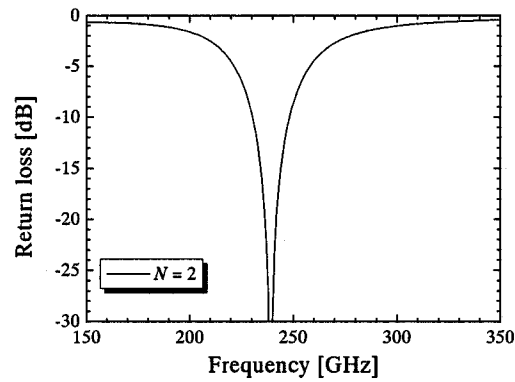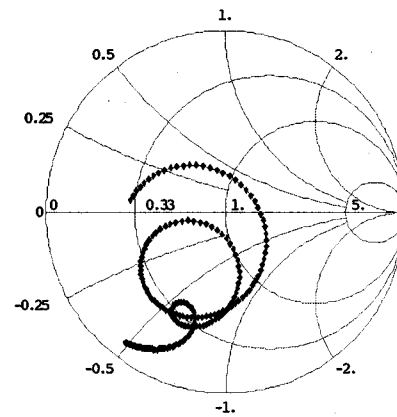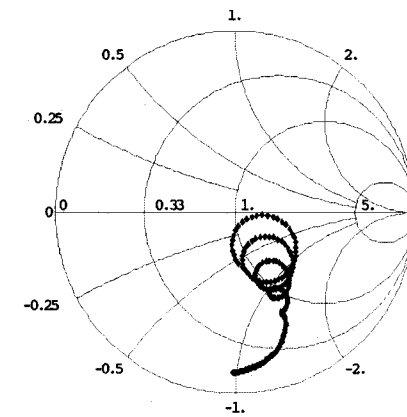
Figure 3.11 Frequency dependence of the input return loss for the array with two, five, and ten junctions. The RF input impedance of each array is also shown on the Smith chart.
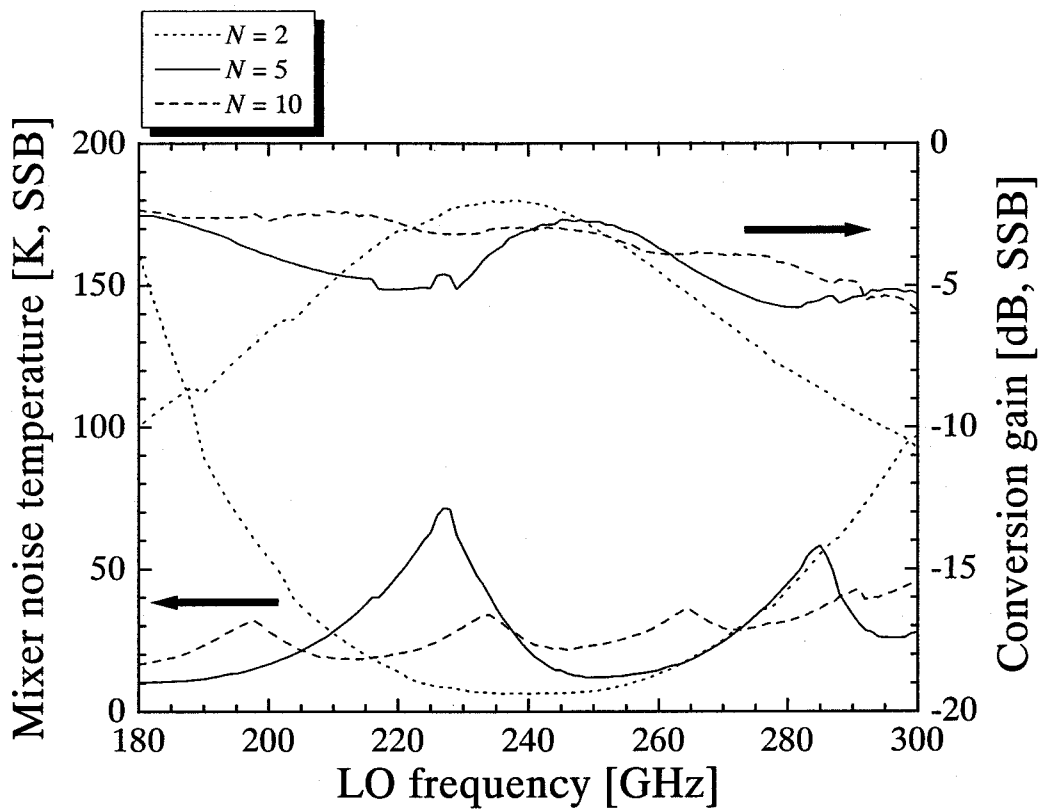
Figure 3.12 Calculated mixer noise temperature and conversion gain for distributed junction arrays with two (dotted lines), five (solid lines), and ten (dashed lines) junctions as a function of frequency in the range from 180 GHz to 300 GHz. N is the number of junctions in the array. The critical current density of 3.0 kA/cm^2 is assumed.

Chapter IV

Design of a 190-300 GHz bands waveguide SIS mixer

4.1 Introduction

Developing broadband waveguide SIS mixers in millimeter- and submillimeter-wave bands has been greatly helpful in the astronomical observations. It was described in the previous chapter that the bandwidth of conventional SIS mixers is strongly dependent on the critical current density of a junction. Although the bandwidth of SIS mixers with distributed junction arrays is less dependent on the critical current density, a large increase of noise temperature and a degradation of conversion gain always occurs at certain frequencies.

To overcome the problem in the distributed junction array, a new type of SIS mixer with an inhomogeneous distributed junction array is proposed in this work [1, 2]. This chapter describes mainly the detailed design and calculation results of the mixing properties for the 190-300 GHz waveguide SIS mixer with the inhomogeneous distributed junction array. Section 4.2 introduces the design method for the inhomogeneous distributed junction array, while section 4.3 gives the calculated mixing properties (i.e., the mixer noise temperature and the conversion gain) using the expanded Tucker's quantum theory of mixing. Section 4.4 gives the complete layout of the SIS mixer-chip, and the conclusion is described in section 4.5.

4.2 Design method for inhomogeneous distributed junction arrays

The inhomogeneous distributed junction array consists of multiple junctions

having different dimensions located on a superconducting microstrip where the spacings between adjacent junctions are different as shown in Fig. 4.1. In the inhomogeneous distributed junction array, the dimensions of junctions and spacings between adjacent junctions must be determined for a given critical current density prior to the calculation of mixing properties.

It is very important for achieving excellent mixing properties that the RF signal is coupled to the SIS junctions efficiently. Therefore the dimensions of junctions and spacings between adjacent junctions were optimized so as to minimize the reflection coefficient (i.e., return loss), which is seen from the input port of the inhomogeneous distributed junction array, in a given frequency range using microwave CAD (Microwave Design System) [3]. To simplify the calculation in the determination of a set of dimensions and spacings, it was assumed that every SIS junction can be represented by a combination of linear resistance R_n and geometrical capacitance C_j connected in parallel. The simplified electrical equivalent-circuit is shown in Fig. 4.2. Note that in the optimization of the dimensions and spacings the conventional distributed junction array (called "homogeneous distributed junction array") was set as the beginning condition.

An inhomogeneous distributed junction array was designed in the frequency range from 190 to 300 GHz. All the junctions were assumed to have the same critical current density of 3.0 kA/cm^2, which is less than half of the values of those used in conventional SIS mixers in the same frequency range. The number of junctions in the inhomogeneous distributed junction array was set as five to give the array a moderate input impedance which enables it to match the source well. The width of the microstrip was assumed to be 6.0 μm.

In the determination of the dimensions of junctions and spacings between every two junctions, there are many possible sets of dimensions and spacings which could satisfy the condition of the optimization for the return loss. Let us express a normalized impedance to the equivalent normal-state resistance of inhomogeneous distributed junction arrays by $z = r + jx$. Here, r and x are the normalized resistance and reactance, respectively. In many obtained solutions, four inhomogeneous distributed junction arrays are mentioned as an example. The first is an array (Array A) which has the input impedance in the region of $r \leq 1$ and $x \leq 0$. The second is an array (Array B) which has the input impedance in the region of $r \leq 1$ and $x \geq 0$. The third (Array C) is an array which has the input impedance in the region of $r \geq 1$ and $x \leq 0$. The last is an array (Array D) which the input impedance in the region of $r \geq 1$ and $x \geq 0$. The dimensions of junctions and spacings between all pairs of adjacent junctions are listed in Table 4.1. For comparison, those in the homogeneous distributed junction array are also presented in Table 4.1. In Table 4.1, $A^{(k)}$ and $L^{(k)}$ express the dimension of the k-th junction and the spacings between k- and $(k+1)$-th junctions, respectively. The equivalent normal-state resistances of the inhomogeneous distributed junction arrays are 3.7 Ω in Array A, 3.2 Ω in Array B, 3.2 Ω in Array C, and 4.3 Ω in Array D.

The frequency dependences of reflection coefficient with the Smith chart plot of the RF impedance for the four inhomogeneous distributed junction arrays are shown in Fig. 4.3. As shown in Fig. 4.3, the reflection coefficient in all inhomogeneous distributed junction arrays is considerably improved over the given frequency range in comparison with that in the homogeneous distributed junction array. The reflection coefficient in homogeneous distributed junction arrays becomes less dependent on frequency as the number of junctions or the critical current density is increased [4].

4.3 Calculation of mixing properties

4.3.1 Quasi-five-port model

The Tucker's quantum theory of mixing is the basis for all analysis and design of SIS mixers. In the mixing theory, an infinite number of mixing frequencies exists since the performance of SIS mixers can be analyzed in term of the multi-frequency model. However, it is fairly time consuming to carry out such analyses. Hence the Tucker's three-frequency approximation has been widely used [5]. In this approximation, it is assumed, as indicated in Fig. 4.4(a), that the embedding impedance seen by the junction is finite at the LO frequency ω, and at the upper, lower sideband ω_1, ω_{-1}, and intermediate frequencies ω_0. At all higher frequencies the junction is short-circuited. This is likely to be a good approximation for junctions with large capacitance. The three-frequency approximation implies a sinusoidal LO voltage at the junction. The mixing theory gives expressions for the elements Y_{ij} and H_{ij} of the 3×3 admittance and noise correlation matrices. The analyses based on this three-frequency approximation do not yield real mixers, although giving some useful insights.

Apparently the three-frequency approximation ignores the conversion effects at the harmonic sidebands of the LO frequency. Although the solution of three-frequency approximation for the SIS mixers with high-$\omega R_n C_j$ junction (>50) is equivalent to a full harmonic-Newton solution [6, 7], it occurs a large difference from the full harmonic-Newton solution for the SIS mixers with small-$\omega R_n C_j$ junction. A quasi five-frequency approximation that can be a considerable improvement compared with the three-frequency approximation was suggested by Kerr et al [8]. The quasi five-frequency approximation assumes the sinusoidal LO voltage waveform. However, while the second LO harmonic 2ω is short-circuited at the junction, the second

62

harmonic sidebands $2\omega \pm \omega_0$ are not. This is depicted in Fig. 4.4(b). Expressions for the elements of the 5×5 admittance and noise correlation matrices are given by the mixing theory. The quasi five-frequency approximation can describe the mixing properties quite well for $\omega R_n C_j$ 4, which is in the appropriate range used in the calculation for the inhomogeneous distributed junction array. Therefore, this quasi five-frequency approximation is employed here to analyze the mixing properties of SIS mixers.

4.3.2 Calculation results

An equivalent large- and small-signal models for the inhomogeneous distributed junction arrays was established in this work, following the method derived by Shi *et al.* for homogeneous distributed junction arrays, and then the mixing properties of the inhomogeneous distributed junction arrays were calculated. The only difference between the analysis for the inhomogeneous distributed junction arrays and that for the homogeneous ones is that the admittance and noise correlation matrices must be derived for each junction, since they depend on the I-V characteristics of individual SIS junctions.

The calculated mixer noise temperature and conversion gain for four types of inhomogeneous distributed junction array are shown in Fig. 4.5. The amplitude of the noise increase is small in the arrays that have the normalized resistance in the region of $r \geq 1$ (i.e., Array C and Array D) as compared with those that have the normalized resistance in the region of $r \leq 1$ (i.e., Array A and Array B), being independent of the value of x. On the other hand, the amplitude of the conversion gain is larger in the arrays with $x \leq 0$ (i.e., Array B and Array D) than those with $x \geq 0$ (i.e., Array A and Array C), being independent of the value of r. If the synthetic receiver performance

is compared in four types of the array, Array D is the most excellent receiver. Therefore, inhomogeneous distributed junction arrays should be designed in the input impedance region of $r \geq 1$ and $x \leq 0$ in order to reduce the amplitude of the noise increase. However, if the value of r becomes very large or the value of x becomes very small, the input coupling efficiency deteriorates. In such an array, although the amplitude of the noise increase becomes very small, the mixer noise temperature and conversion loss become remarkably large. It was derived from the calculation of the mixing properties that the optimal value of the normalized input resistance is in the range of $1 \leq r \leq 2.5$ and that of the normalized input reactance is in the range of $-1 \leq x \leq 0$. The same phenomena as inhomogeneous distributed junction arrays can be observed also in homogeneous distributed junction arrays (see Fig. 3.11). In the homogeneous distributed junction array with five junctions the normalized input resistance is in the range of $r \leq 1$. On the other hand, in the homogeneous distributed junction array with ten junctions the normalized input resistance is in the range of $r \geq 1$ and the amplitude of the noise increase is small. In the homogeneous distributed junction arrays it is impossible to move an impedance locus to the optimal range ($1 \leq r \leq 2.5$ and $-1 \leq x \leq 0$) unless the number of junction or current density is increased, in the inhomogeneous distributed junction arrays it is possible to control the impedance locus easily by changing the set of dimensions of junctions and spacings between every two junctions, without increasing the number of junctions or the critical current density. Finally, Array D (the input impedance is in the range of the optimal value) was selected from the obtained sets by optimization described in Section 4.2.

It is well known in the analysis of SIS mixers with single junctions that one of the key parameters of determining the performance of SIS mixers is the RF embedding

impedance. Figure 4.6 shows the mixer noise temperature and conversion gain for an SIS mixer with single junction at 240 GHz to the normalized RF terminating impedance. The normalized IF termination, $R_{IF}/R_{n,e}$, was assumed to be 10 in order to compare with the result for the inhomogeneous distributed junction array. It is found from Fig. 4.6 that in single-junction SIS mixers the optimum range in the RF terminating impedance is the region with a hatch and corresponds to the optimum region in the input impedance of inhomogeneous distributed junction arrays well. In inhomogeneous distributed junction arrays, it is possible to make the input impedance exist in the region by controlling an impedance locus, even if operating frequency shifts from center frequency.

Figure 4.7 shows the calculated mixer noise temperature and conversion gain for the inhomogeneous (Array D) and homogeneous distributed junction arrays. As shown in Fig. 4.7, it is found that the amplitude of the noise increase at certain frequencies is considerably reduced in the inhomogeneous distributed junction array, in contrast with the homogeneous distributed junction array with the same number of junctions. The fluctuation of the conversion gain over the frequency band is also very much reduced in the inhomogeneous distributed junction array.

It is possible to reduce the distributed junction array to an equivalent single-junction unless a total length of distributed junction array becomes enough longer than a wavelength at an operation frequency. The limitation of noise temperature in homogeneous distributed junction arrays with a moderate number of junctions ($N<10$) would be given by quantum limited noise hf/k. It may be possible to design complex tuning circuits which have multiple resonances with conventional SIS mixers. The distributed junction arrays inherently have multiple resonances, whose number is dependent on the number of junctions as described in the previous chapter. In the

inhomogeneous distributed junction arrays, it is possible to design so that the resonances continuously occur over the given frequency range. The resonance characteristic then makes blur over the frequency range. Therefore the fluctuation of mixing properties is considerably reduced in the inhomogeneous distributed junction arrays, but the minimum noise temperature may become a little large than that of the homogeneous distributed junction arrays with the same number of junctions. This relation between the minimum noise and the fluctuation is similar to behaviors of the Chevishev filters.

From the viewpoint of amplitude of noise increase, it is clear that the inhomogeneous distributed junction array with five junctions is nearly competitive with the homogeneous distributed junction array with ten junctions. Namely, the number of junctions can be further reduced in inhomogeneous distributed junction arrays than that of homogeneous distributed junction arrays in order to achieve nearly the same mixing properties. This will bring significant advantages in the fabrication of junctions and impedance match to the source.

When the dimensions of junctions in the inhomogeneous distributed junction array were optimized using microwave CAD, a constraint that the dimension of each junction must be the same as or large than that in the homogeneous distributed junction array was included. This constraint makes the fabrication of the inhomogeneous distributed junction array easier than that of the homogeneous distributed junction array. In spite of the restricted optimization, however, it is found that the entire mixing property was extremely improved in the inhomogeneous distributed junction array. It is also noted here that the calculated SSB mixer noise temperature and SSB conversion gain of the inhomogeneous distributed junction array were less than 40 K and larger than -5.0 dB in

the frequency range from 190 to 300 GHz, respectively. This mixing property is competitive with that in the conventional SIS mixer.

4.4 Waveguide SIS mixer-chip

The waveguide-type mount of the 190-300 GHz band SIS mixer was based on a 470 GHz waveguide SIS mixer mount using in Nobeyama Radio Observatory (NRO) [9], with a scaling factor of 1.95. The SIS mixer chip consists of a waveguide probe, three stages of quarter-wavelength impedance transformer, the inhomogeneous distributed junction array, and an IF/dc-bias circuit. Detailed descriptions for all the components of the SIS mixer are given below.

4.4.1 Waveguide probe

To yield a tuneless waveguide SIS mixer, broadband RF matching between the input waveguide (of a characteristic impedance around 500 Ω) and the SIS junction (of a typical input impedance less than 100 Ω) is essential. A very reduced-height waveguide is quite effective but may become too small-sized to be fabricated in the higher frequency region. One good alternative is to use a waveguide probe inserted across the waveguide. Waveguide probes play a role to transit RF signal to microstrip mode from waveguide mode. A waveguide probe used in this work was proposed by Shi *et al.* [10]. The schematic representation is shown in Fig. 4.8. The coupling efficiency of the signal to the microstrip through the waveguide probe is strongly dependent on the inductance of the waveguide probe as the larger inductance brings the narrower bandwidth of the transition [11]. Since the inductance can vary by shifting the waveguide probe from the central waveguide E-plane, the waveguide probe was shifted

a distance Δy from the central E-plane so as to improve the bandwidth of the transition. The dimensional parameters of RF input circuit including the probe are listed in Table 4.2.

The analysis of this waveguide-to-microstrip transition was performed using Hewlett Packard's High Frequency Structure Simulator (HFSS), in which a finite-element method (FEM) is available [12]. For the calculation of the S-parameter, two ports were set in the structure. One (port 1) is at the waveguide and the other (port 2) is at the 75-Ω microstrip. The calculated reflection coefficient S_{11} and transmission coefficient S_{21} are shown in Fig. 4.9. The excellent power coupling to the 75-Ω microstrip from the waveguide can be achieved in the frequency range from 190 to 274 GHz. The coupling efficiency, however, is degraded above 274 GHz. The reason for this is that the undesirable modes occur in the waveguide, in which the electromagnetic wave can no longer be propagated by the single mode (only TE_{10}-mode) above 274 GHz.

4.4.2 RF impedance transformer

The quarter-wavelength impedance transformer section is aimed to match the output impedance (75 Ω) of the waveguide-to-microstrip transition to the input impedance (5 Ω) of the inhomogeneous distributed junction array. Since this impedance ratio (= 75/5) is extremely large, three stages of impedance transformer were employed. The first stage is the microstrip of 255 μm wide connected just after a 75-Ω microstrip. This microstrip has a characteristic impedance of 44.7 Ω and a length of 181 μm ($\sim \lambda_g/4$ at 245 GHz). Both its characteristic impedance and wavelength were calculated with the aid of HFSS. The second and third stages are made of a Nb-based superconducting

microstrip with a dielectric layer consisted of Nb_2O_5, SiO_2 and Al_2O_3. The second stage of 4 μm wide and 109 μm long ($\sim \lambda_g/4$) has a characteristic impedance of 14.9 Ω. The third stage of 11 μm wide and 109 μm long ($\sim \lambda_g/4$) has a characteristic impedance of 6.6 Ω.

4.4.3 RF choke filter

In order to avoid that the LO and RF frequencies enter the substrate channel, the substrate supports a low-pass filter which passes the IF output signal and the DC bias, but rejects the LO and RF signals. The RF choke filter consisted of a series of wide and narrow sections of microstrip with a length of $\lambda_g/4$. As is commonly in series with SIS junctions, such an RF choke filter is required to provide an RF short-circuit at its input port so as to make the RF and LO signals to be coupled to the junctions efficiently.

Figure 4.10 shows the RF choke filter used in the 190-300 GHz band SIS mixer. The wavelength along microstrip is found by the relation $\lambda_g = \lambda_0/(\varepsilon_{eff})^{1/2}$, where λ_0 is the free space wavelength and ε_{eff} is the effective dielectric constant. The effective dielectric constant is somewhat lower than the dielectric constant of the material itself, because part of electromagnetic field is transmitted in the space above the microstrip. It can be seen from Fig. 4.10 that the conductor of the low-impedance section is adjacent to the metallic enclosure of the slot channel and there are gaps between the substrate and the vertical walls of the enclosure. Therefore it is possibly inappropriate to regard these transmission lines as the conventional microstrips. The characteristic impedance and the effective dielectric constant were analyzed using HFSS. The first section of the RF choke filter is slightly shorter than other low-impedance section, because of one tapered section introduced to reduce the coupling effect between the choke filter and the first

quarter-wavelength impedance transformer. The input impedance of the RF choke filter normalized to 27 Ω (= $44.7^2/75$) is plotted on a Smith chart in Fig. 4.11. It is found that the filter achieves an RF short-circuit at its input port. Figure 4.12 shows the calculated frequency dependence of the return loss. The rejection bandwidth of the RF choke filter is in the frequency range from 160 to 320 GHz.

4.4.4 Complete layout of the 190-300 GHz band SIS mixer-chip

A waveguide probe, RF impedance matching circuit, inhomogeneous distributed junction array, and RF choke filter are integrated in the SIS mixer-chip used in this work. The layout of mixer chip is shown in Fig. 4.13. The 25-μm diameter Al wires are ultra-sonically bonded into the IF and DC output of a 50-Ω microstrip followed by an SMA connector. The slot of the other port, which is the region of the left end in Fig. 4.13, is filled with indium and electrically grounded.

The RF embedding impedance seen by the inhomogeneous distributed junction array was calculated. The normalized embedding impedance to the normal-state resistance of the inhomogeneous distributed junction array (5 Ω) at the fundamental sideband frequencies is plotted in Fig. 4.14.

An important consideration of designing SIS mixers is the IF bandwidth. It is pointed out by Padin *et al.* that to realize a wide IF bandwidth, the SIS mixer must be designed with low output capacitance, and in general minimizing the output circuit parasitics (capacitance and inductance) will facilitate broadband coupling to the IF amplifier [13]. In many SIS mixers most of the output capacitance is associated with the quarter-wavelength impedance transformers and RF choke filter except for SIS junctions, and the output inductance is mainly in the RF choke filter. For the 190-300

GHz band SIS mixer, the static (low frequency) capacitance is 1604 fF, which is a sum of 76 fF from the RF choke filter, 223 fF from the RF impedance-transformer section, and 1305 fF from the inhomogeneous distributed junction array. The low-frequency inductance is 556 pH, of which only 22 pH is from the RF impedance-transformer section. The value of the IF output capacitance is quite large. Especially, the contribution from the inhomogeneous distributed junction array is large compared with the conventional SIS mixer, in which the junction capacitance is the order of several ten to several hundreds fF. This large contribution from the array may possibly overcome by connecting the arrays in series, but the mixer layout must be reconsidered in this case. The IF cutoff frequency is given by

$$ f_c = \frac{1}{2\pi\sqrt{L_{if}C_{if}}}, \tag{4.1} $$

where L_{if} and C_{if} are the IF output inductance and capacitance, respectively. In this SIS mixer the IF cutoff frequency was 5.3 GHz. Therefore, the IF amplifier with 1-2 GHz bandwidth is well available in the experiment.

4.4.5 Mixer block construction

It is very important that the temperature of the mixer chip in the mixer block is as low as possible (close to the temperature of the liquid helium temperature of 4.2 K). The mixer block itself is cooled by conduction via the cold stage (4.2 K) of a GM/JT refrigerator. The mixer block used in this work was therefore made of oxygen-free high-conductivity (OFHC) copper plated with gold. The mixer block is split into two halves. The alignment of two halves is determined by two fitting pins. A slot channel is included in one of the halves. A corrugated feed horn is connected through the

waveguide flange of UG-387/U-M, which is included in other half. Externally-adjustable mechanical tuners are not employed for simplicity.

The IF circuit substrate was consisted of a 50-Ω microstrip and was made of RT/duroid 5880 with 0.38-mm thick ($\varepsilon_r = 2.2$). The IF circuit substrate is put into the square space (6.87×10 mm) and is driven screw with a screwdriver. An SMA connector was soldered to the microstrip-conductor of the IF circuit substrate. A commercial bias tee, which takes part in supplying a DC current to the SIS junction, set to the outside of the mixer block.

The complete drawing of the mixer block is displayed in Figs. 4.15-17. Figure 4.18 shows the photograph of the mixer block.

4.5 Conclusions

The theoretical analyses for SIS mixers with inhomogeneous distributed junction arrays were carried out in this chapter. In the inhomogeneous array, dimensions of junctions and spacings between every two junctions were optimized so that return loss becomes small. Form many solutions obtained by optimization, one inhomogeneous distributed junction array, which has the optimal input impedance, was selected. The optimal value of the normalized input resistance is in the range of $1 \le r \le 2.5$ and that of the normalized input reactance is in the range of $-1 \le x \le 0$. It was found that the optimal region of the input impedance for inhomogeneous distributed junction arrays corresponds to that of the RF terminating impedance for single-junction SIS mixers well. The extended quantum theory of mixing for the inhomogeneous distributed junction array was established and the mixing properties were theoretically calculated. Two main results were obtained from the calculation of mixing properties. One is that the critical

72

current density to achieve a reasonable bandwidth can be lowered in the homogeneous and inhomogeneous distributed junction arrays compared with the conventional single-junction SIS mixers. Other is that the amplitude of the noise increase, which always occurs at certain frequencies in the homogeneous distributed junction arrays, can be extremely reduced in the inhomogeneous distributed junction arrays. In the inhomogeneous distributed junction array with the critical current density of 3.0 kA/cm^2, the SSB mixer noise temperature less than 40 K and the SSB conversion gain larger than -5.0 dB were predicted in the frequency range from 190 to 300 GHz.

The waveguide-type mixer chip for the 190-300 GHz band SIS mixer was consisted of a waveguide probe, three-stages of quarter-wavelength impedance transformer, inhomogeneous distributed junction array, and RF choke filter. The characteristics of each component were precisely calculated.

References

[1] M. Takeda and T. Noguchi, "Performance of inhomogeneous distributed junction arrays", *Applied Superconductivity*, **167**, 639 (1999).

[2] M. Takeda, T. Noguchi and S. -C. Shi, "Predicted performance of SIS mixers with inhomogeneous distributed junction arrays", *Jpn. J. Appl. Phys.*, **39**, 9A, 5095 (2000).

[3] *Microwave Design System*, Hewlett-Packard Co., Palo Alto, CA 94303, USA.

[4]S. -C. Shi, T. Noguchi, J. Inatani, Y. Irimajiri and T. Saito, "Experimental results of SIS mixer with distributed junction arrays", *Proc. 9th Int. Symp. Space Terahertz Technology*, Pasadena, USA, 223, March (1998).

[5] J. R. Tucker and M. J. Feldman, "Quantum detection at millimeter wavelengths",

Rev. Mod. Phys., **57**, 4, 1055 (1985).

[6] C. -Y. E Tong and R. Blundell, "Simulation of superconducting quasiparticle mixer using a five-port model", *IEEE Trans. Microwave Theory Tech.*, **38**, 10, 1391 (1990).

[7] M. J. Feldman and S. Rudner, "Mixing with SIS arrays", in *Reviews of Infrared & Millimeter Waves*, New York: Plenum, **1**, 47 (1983).

[8] A. R. Kerr, S -K Pan, and S. Withington, "Embedding impedance approximations in the analysis of SIS mixers", *IEEE Trans. Microwave Theory Tech.*, **41**, 4, 590 (1993).

[9] S. -C. Shi and T. Noguchi, "Low-noise superconducting receiver for millimeter and submillimeter wavelengths", *IEICE Trans. Electronics*, **E-81c**, 1584 (1998).

[10] S. -C. Shi and J. Inatani, "A Waveguide-to-microstrip transition with a DC/IF return path and an offset probe", *IEEE Trans. Microwave Theory Tech.*, **45**, 3, 442 (1997).

[11] Y. C. Shih, T. N. Ton, and L. Q. Bui, "Waveguide-to-microstrip probe transitions for 26-110 GHz frequency range", *MWSYM*, **1**, 473 (1988).

[12] *High Frequency Structure Simulator*, Hewlett-Packard Co., Palo Alto, CA 94303, USA.

[13] S. Padin, D. P. Woody, J. A. Stern, H. G. LeDuc, R. Blundell, C. -Y. E Tong, and M. W. Pospieszalski, "An integrated SIS mixer and HEMT IF amplifier", *IEEE Trans. Microwave Theory Tech.*, **44**, 6, 987 (1996).
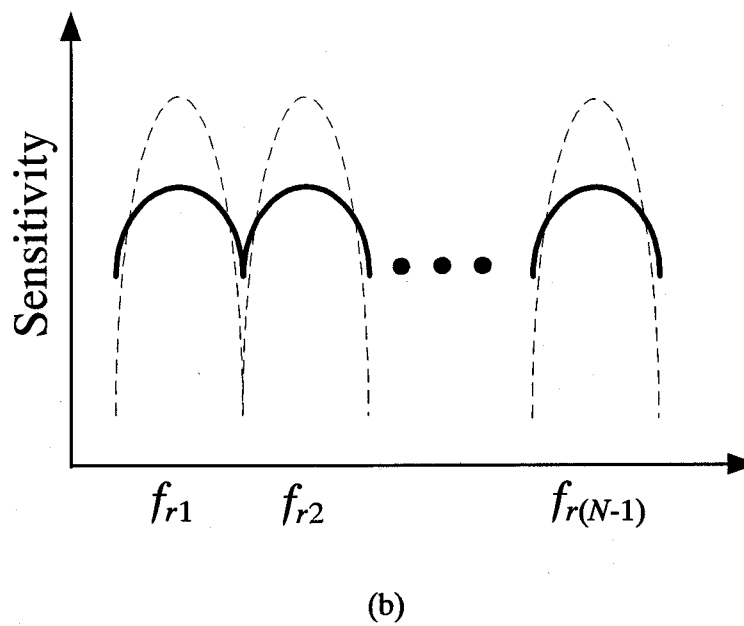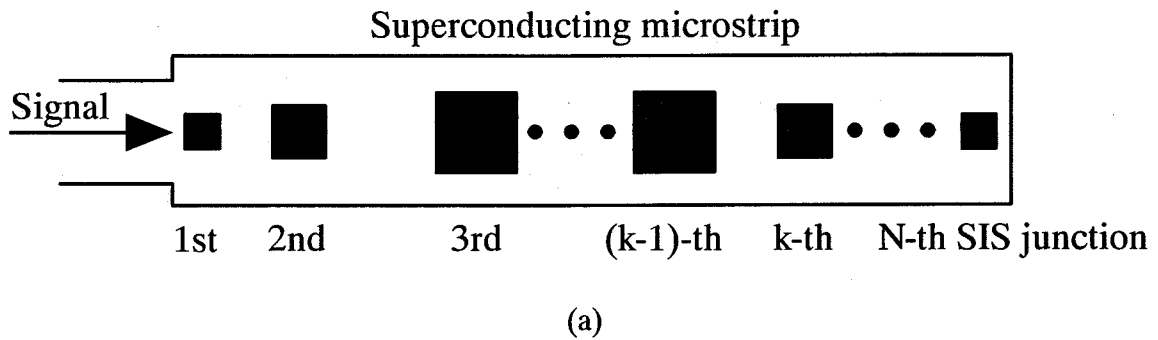
Superconducting microstrip

Signal → ■ ■ ■ • • • ■ ■ • • • ■

1st 2nd   3rd   (k-1)-th k-th N-th SIS junction

(a)

Sensitivity

f_{r1} f_{r2} $f_{r(N-1)}$

(b)

Figure 4.1 (a) Schematic representation of an inhomogeneous distributed junction array with N junctions. (b) Resonance property of the inhomogeneous distributed junction array. The receiver sensitivity becomes less dependence on frequency compared with the homogeneous distributed junction array.
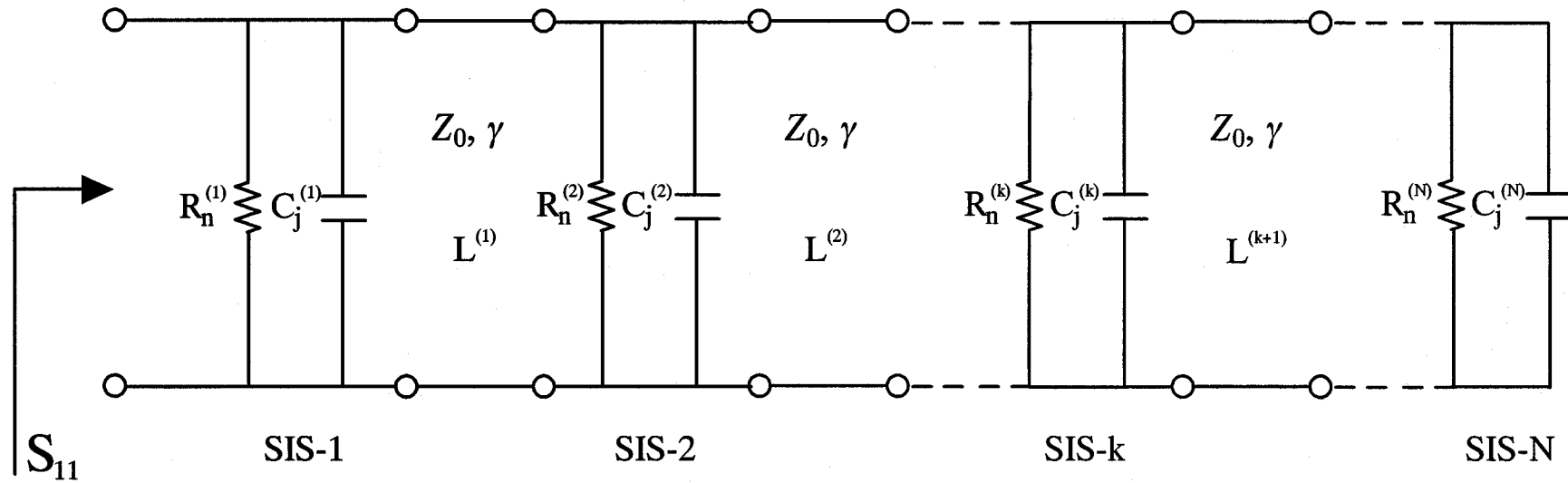
Figure 4.2 Simplified equivalent circuit of an inhomogeneous distributed junction array. Tuning inductances are represented by microstrip with the characteristic impedance of Z_0 and propagation constant of γ. The geometrical capacitance C_j and spacing L are optimized so that the reflection coefficient of an S-parameter, S_{11}, is minimized using Microwave Design System (MDS).
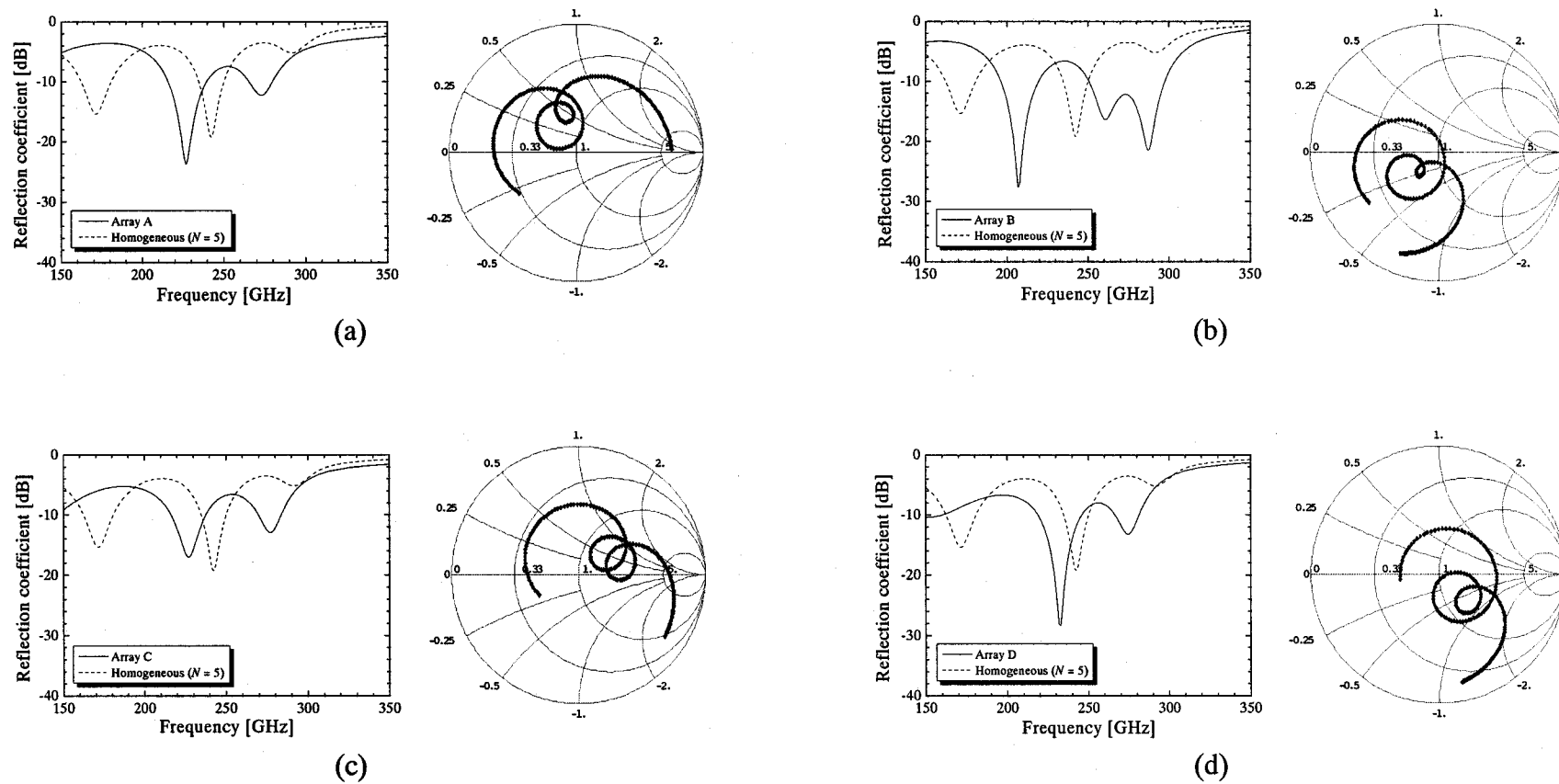
Figure 4.3 Reflection coefficient of S-parameter, S_{11}, and Smith chart of the RF impedance normalized to the equivalent normal-state resistance for the optimized inhomogeneous distributed junction arrays with five junctions. (a) Array A; (b) Array B; (c) Array C; and (d) Array D. Junction critical current density is 3.0 kA/cm^2 in both arrays. N is the number of junctions in the array.
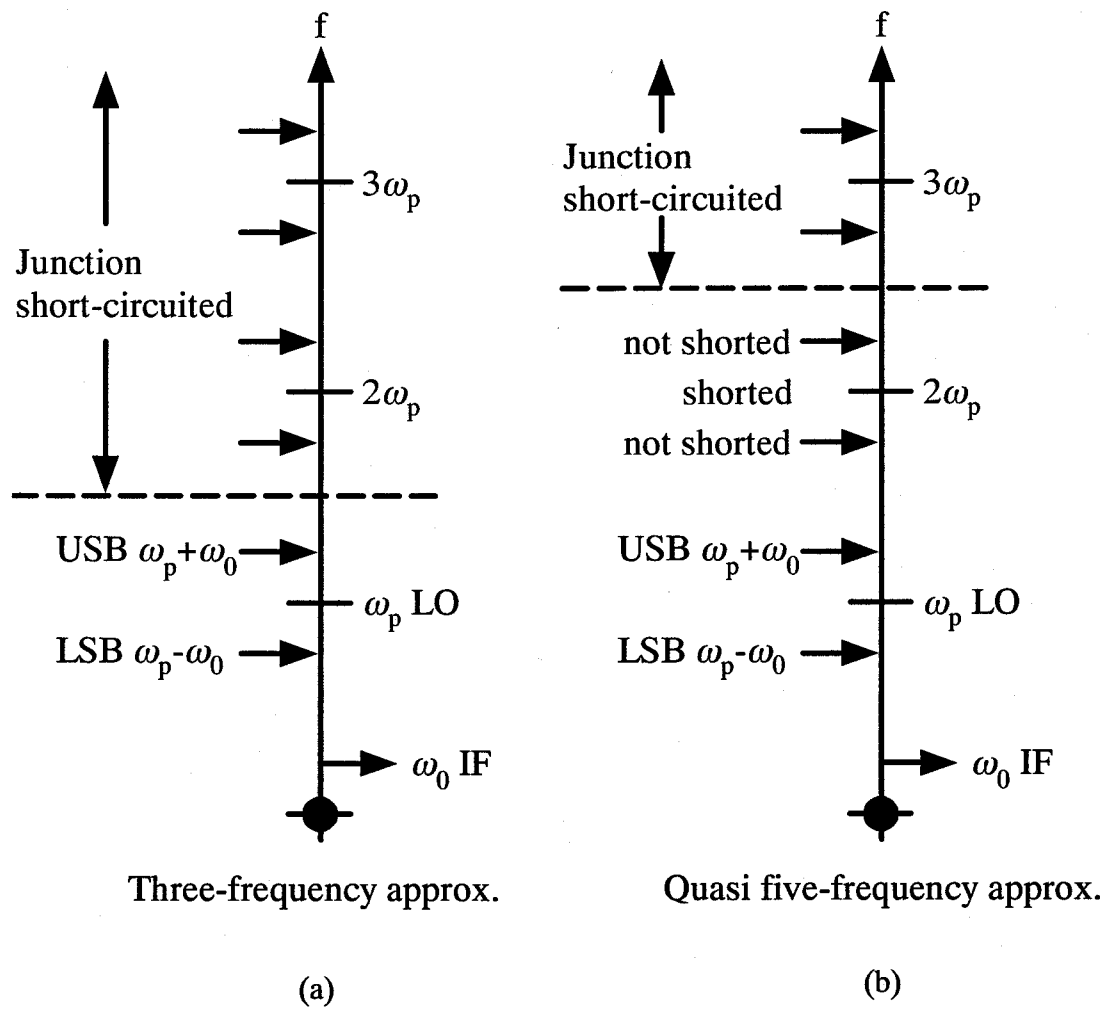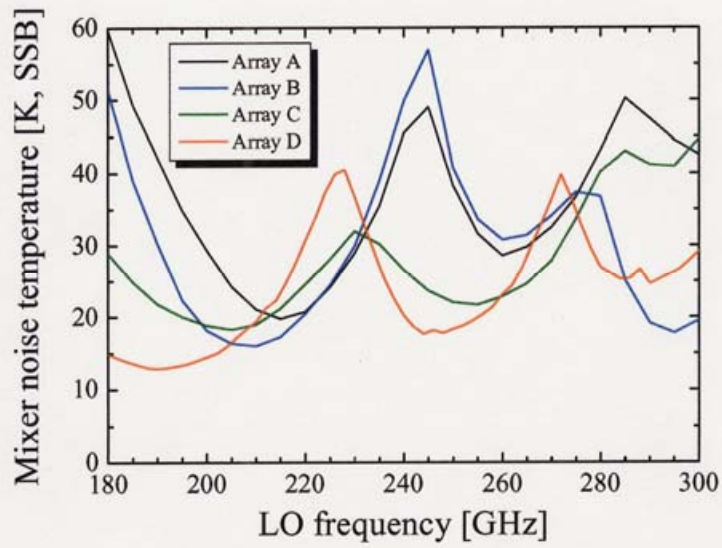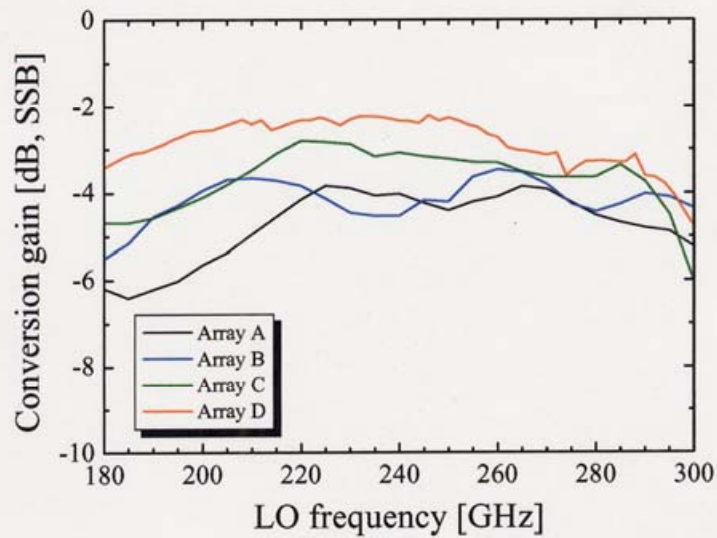
Figure 4.4 Embedding impedance diagram indicating which frequencies are short-circuited for the two approximations: (a) three-frequency, (b) quasi five-frequency.

(a)

(b)

Figure 4.5 Calculated mixing properties for four types of inhomogeneous distributed junction arrays (Array A, Array B, Array C, and Array D) as a function of LO frequency. (a) Mixer noise temperature; (b) Conversion gain. Array D is the most excellent receiver performance.
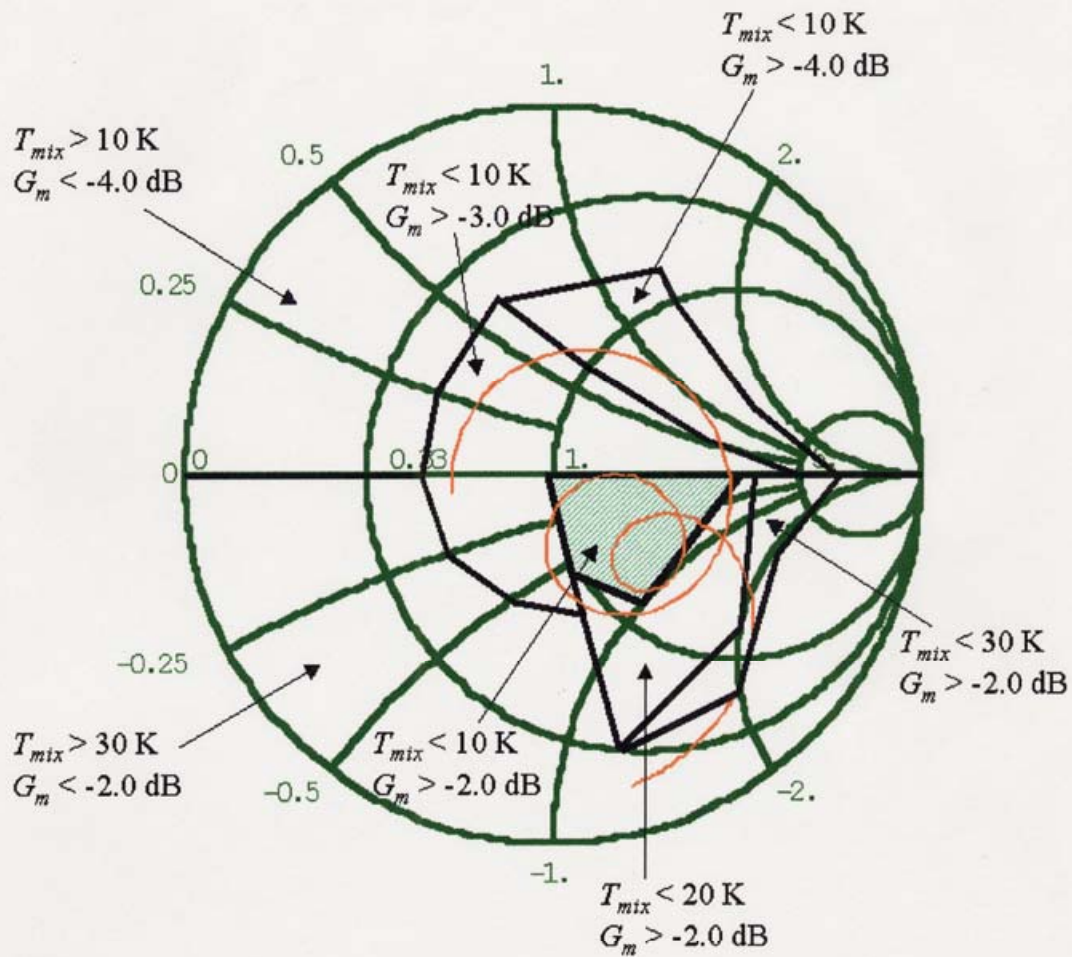
79

Figure 4.6 Calculated mixer noise temperature and conversion gain at 240 GHz for single-junction SIS mixers to the RF terminating impedance. In the region with a hatch, the mixer shows the most excellent receiver performance. The input impedance locus (red line) for Array D exists in the optimal region for single-junction SIS mixers.
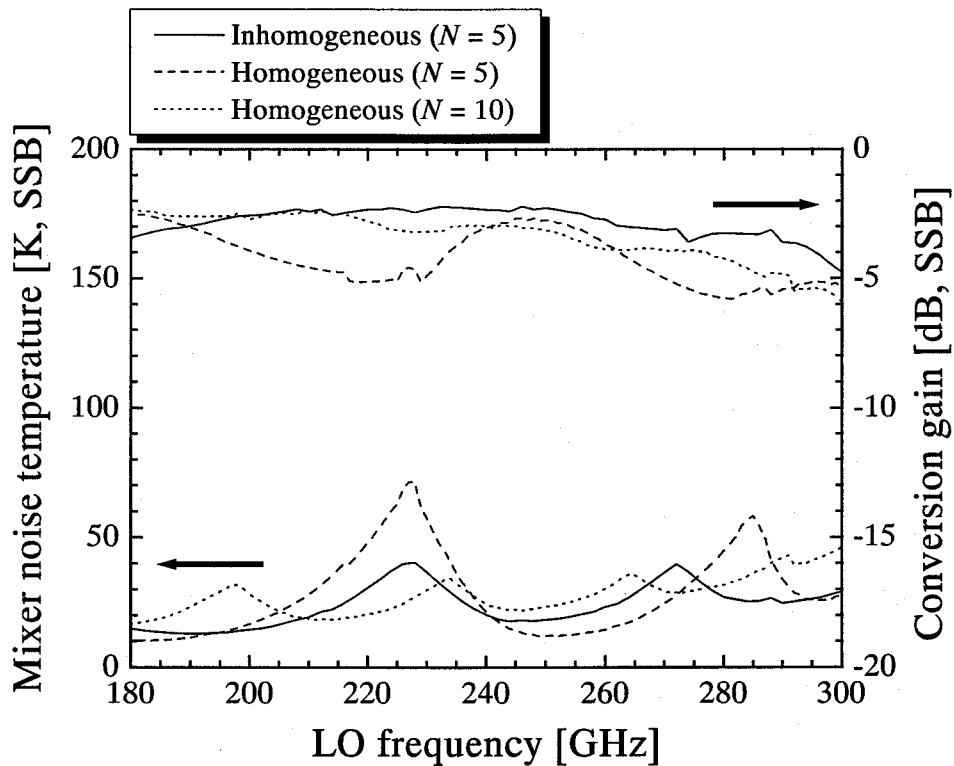
Figure 4.7 Calculated mixer noise temperature and conversion gain for inhomogeneous and homogeneous distributed junction arrays with five junctions and homogeneous distributed junction array with ten junctions as a function of frequency in the range from 180 GHz to 300 GHz. Junction critical current density Junction critical current density is 3.0 kA/cm².

GND DC/IF Path

Waveguide
(Port 1)

75-Ω microstrip
(Port 2)

A-A

Waveguide probe
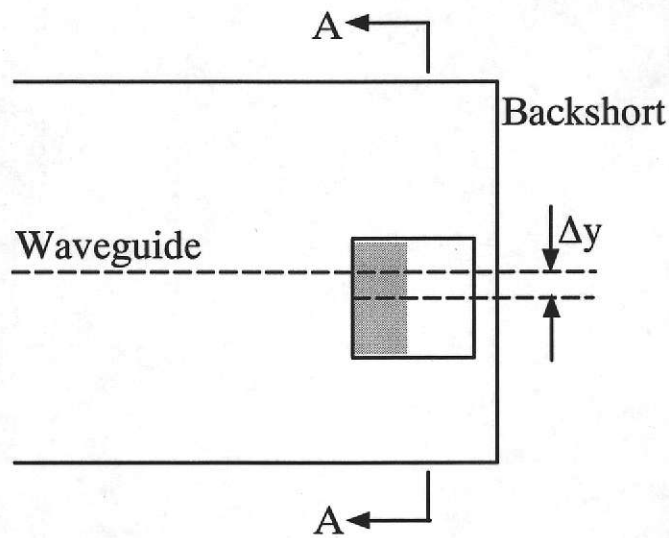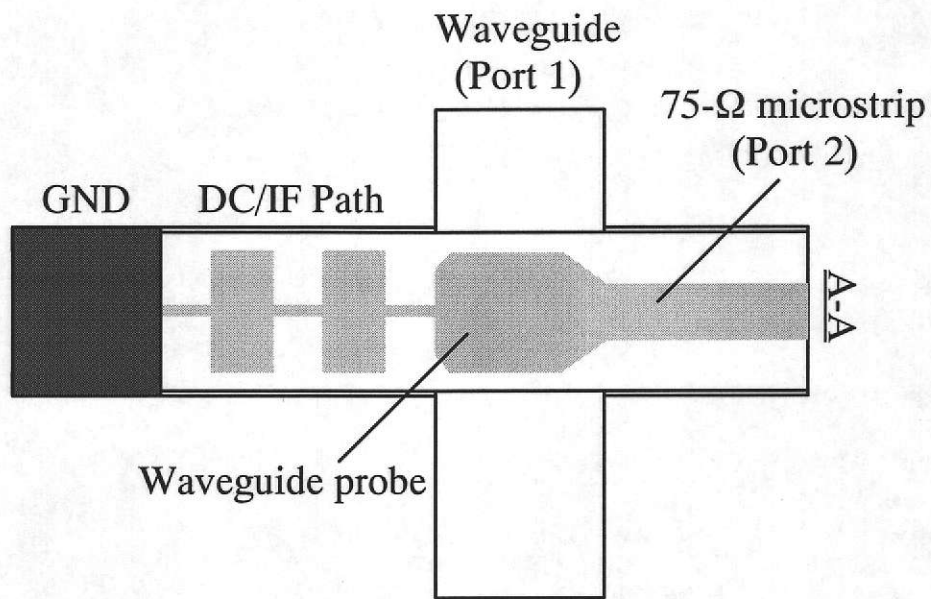
A

Backshort

Waveguide

Δy

A

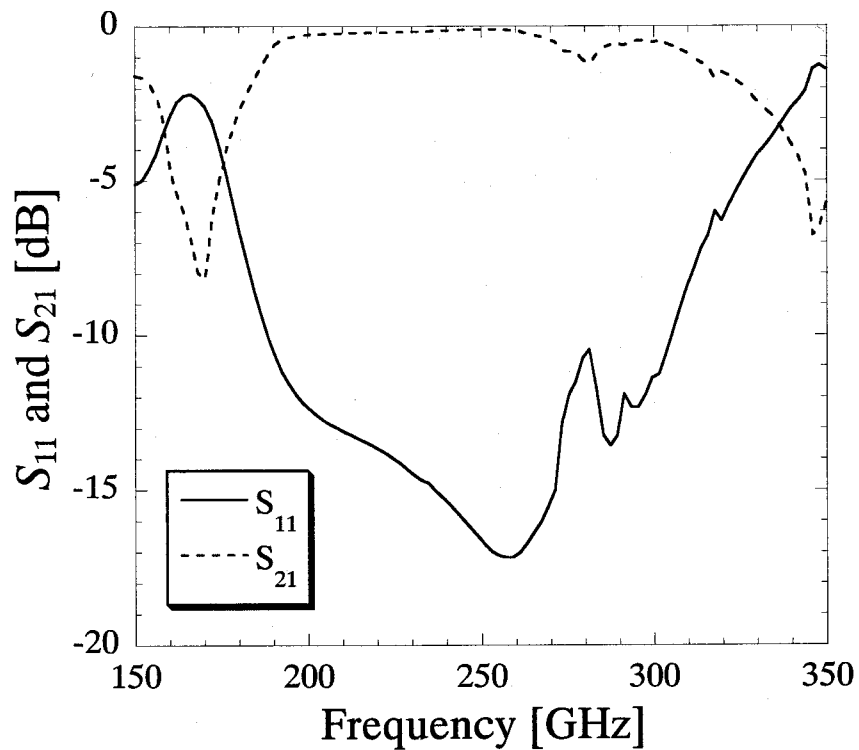Figure 4.8 Cross-sectional view of the waveguide-to-microstrip transition.

Figure 4.9 Calculated S-parameter of a two-port structure as a function of frequency. S_{11} (solid line) shows the reflection coefficient at port 1, and S_{21} (dashed line) shows the transmission coefficient from port 1 to port 2.
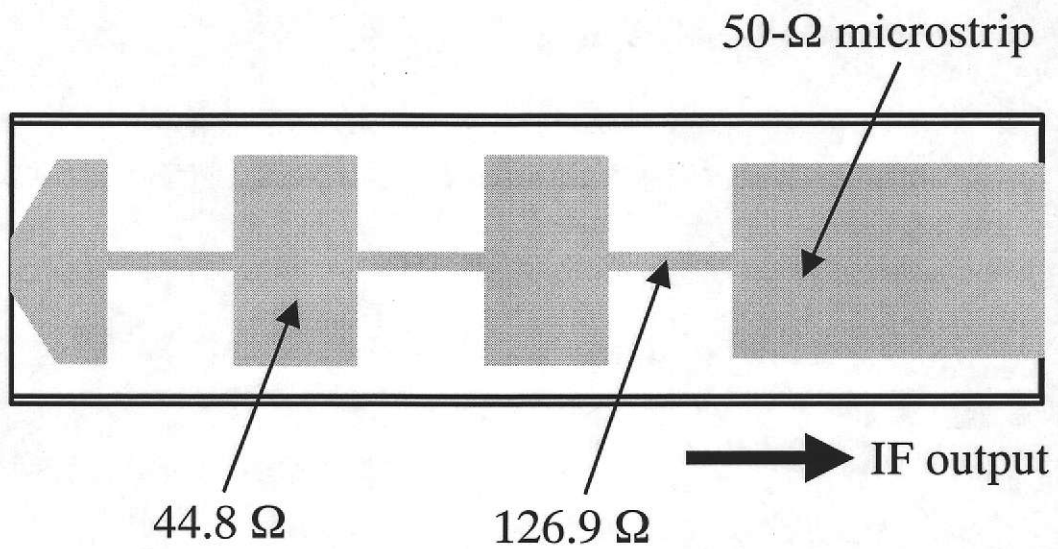
Figure 4.10 Schematic layout of the RF choke filter, scaled from the design of Shi in Ref. [8], for the 190-300 GHz band SIS mixer.
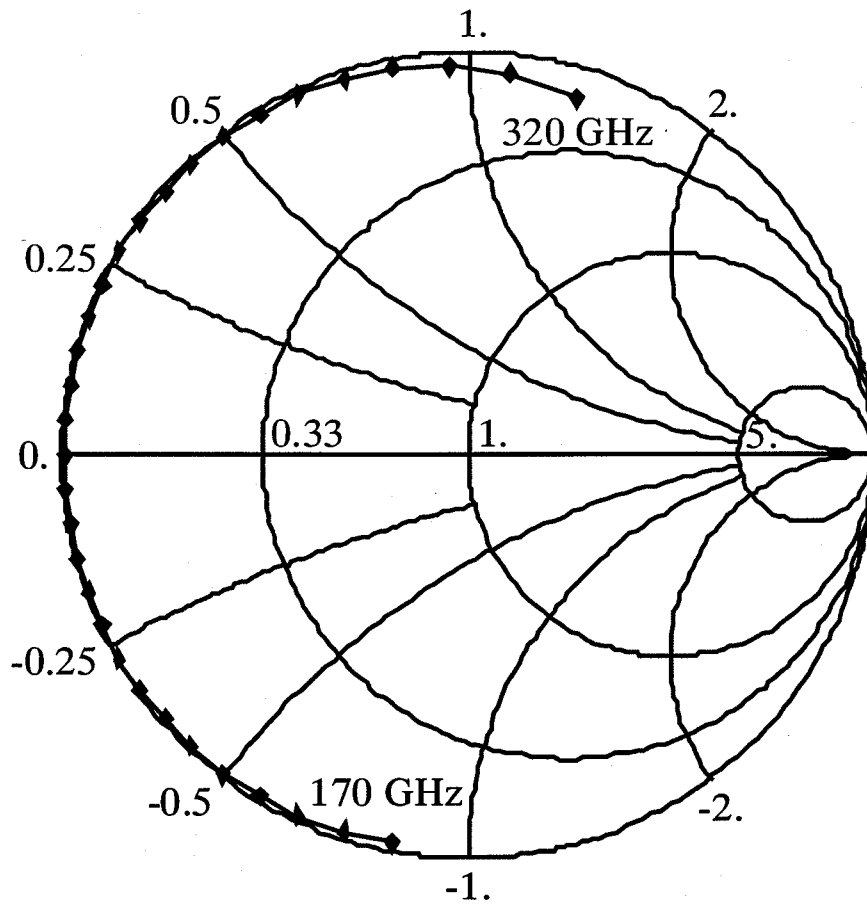
Figure 4.11 Input impedance of the RF choke filter normalized to 27 Ω for 190-300 GHz band SIS mixer in the frequency range from 170 GHz to 320 GHz.
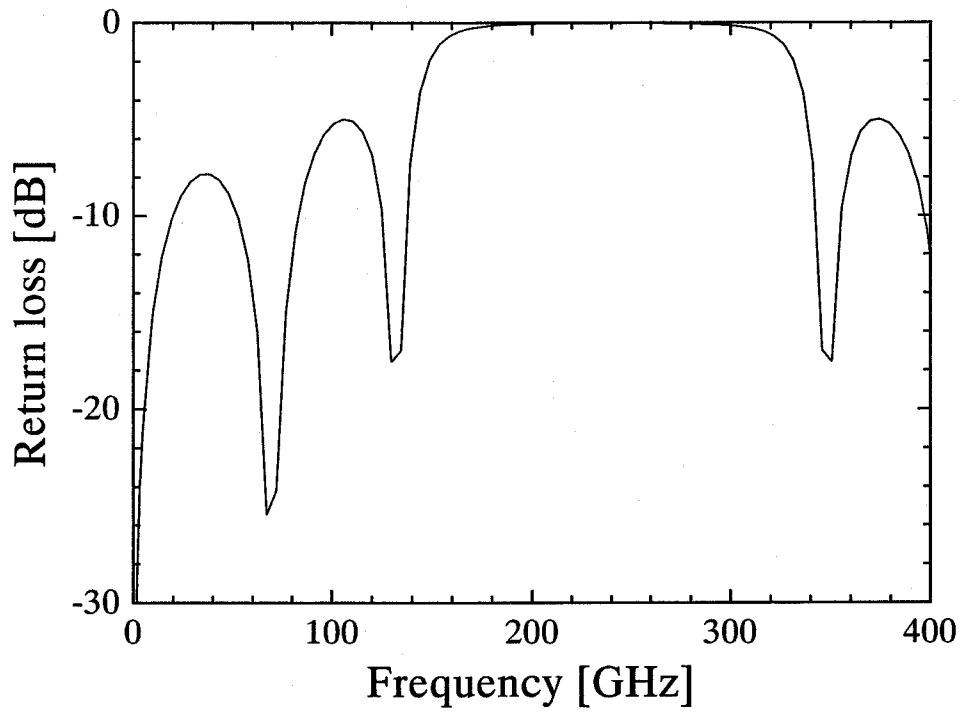
Figure 4.12 Calculated frequency dependence of the return loss of the choke filter for the 190-300 GHz band SIS mixer.

W.G.

Probe

Chip slot

Transformers   RF choke filter

GND

IF Port

Chip slot

IF/DC return

Inhomogeneous
distributed junction array

Quartz substrate
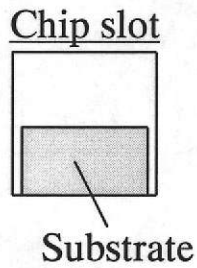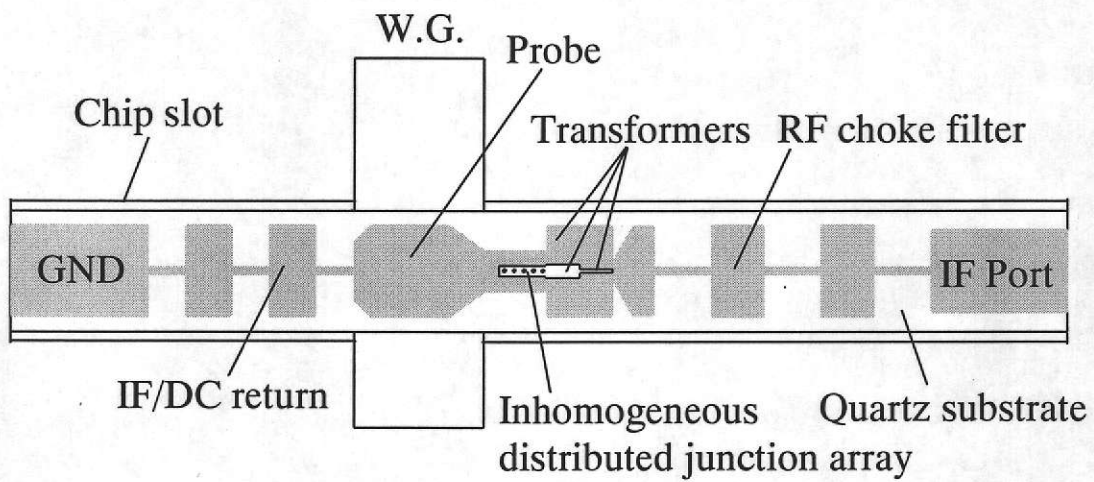
Substrate

W.G. : 1.039 mm X 0.359 mm
Chip Slot : 0.359 mm X 0.359 mm
Substrate : 4.4 mm X 0.34 mm X 0.17 mm
Probe Offset : 0.076 mm
Backshort : 0.0567 mm

Figure 4.13 Schematic layout of the complete SIS mixer chip for the 190-300 GHz band
SIS mixer.
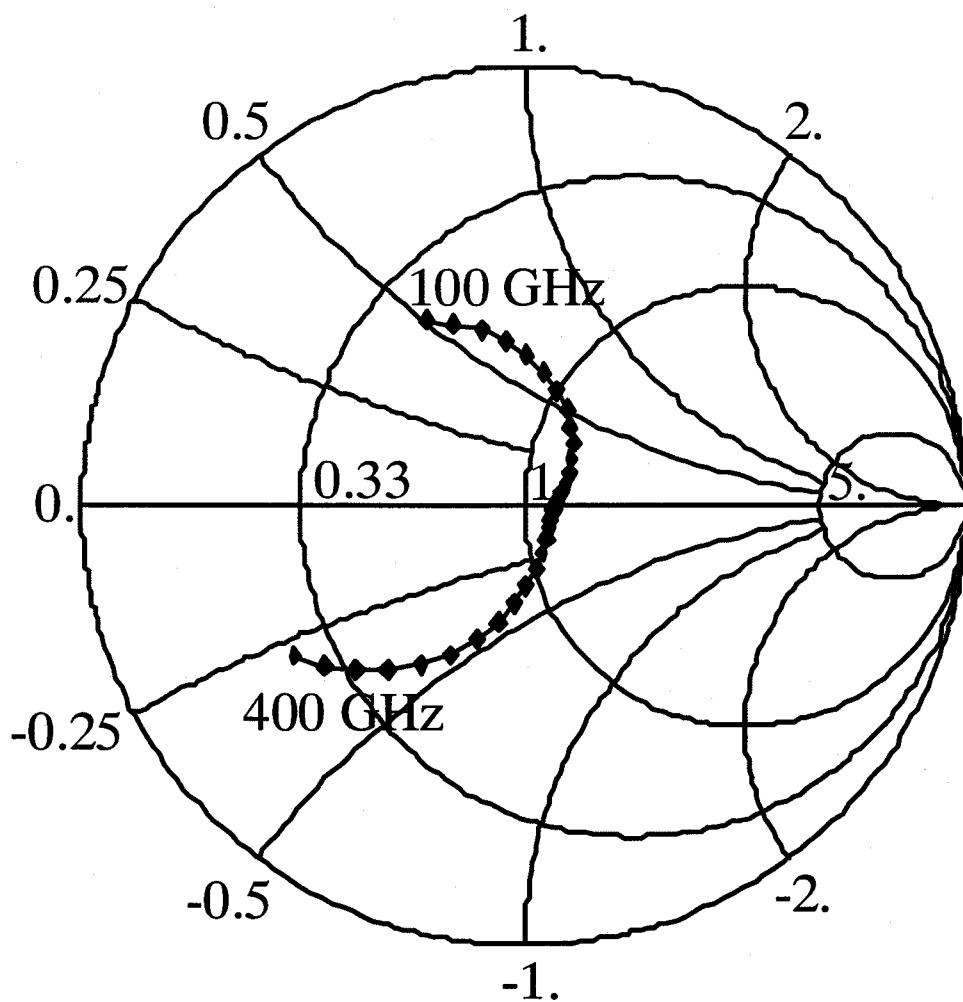
Figure 4.14 RF embedding impedance seen by the inhomogeneous distributed junction array. The RF embedding impedance was normalized to the normal-state resistance of 5 W on Smith chart.
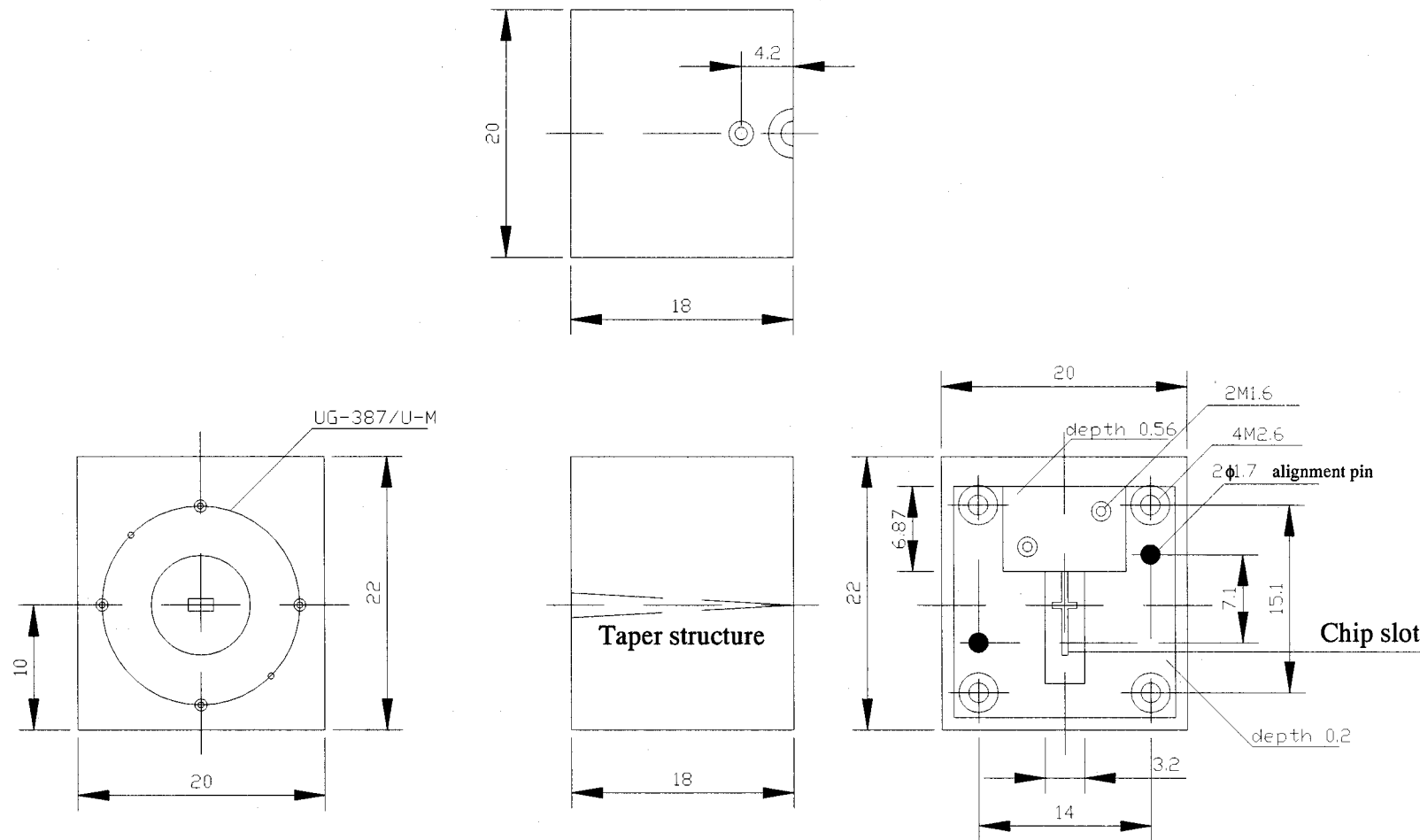
Figure 4.15 A drawing of a half part including the chip slot for the 190-300 GHz band SIS mixer block.
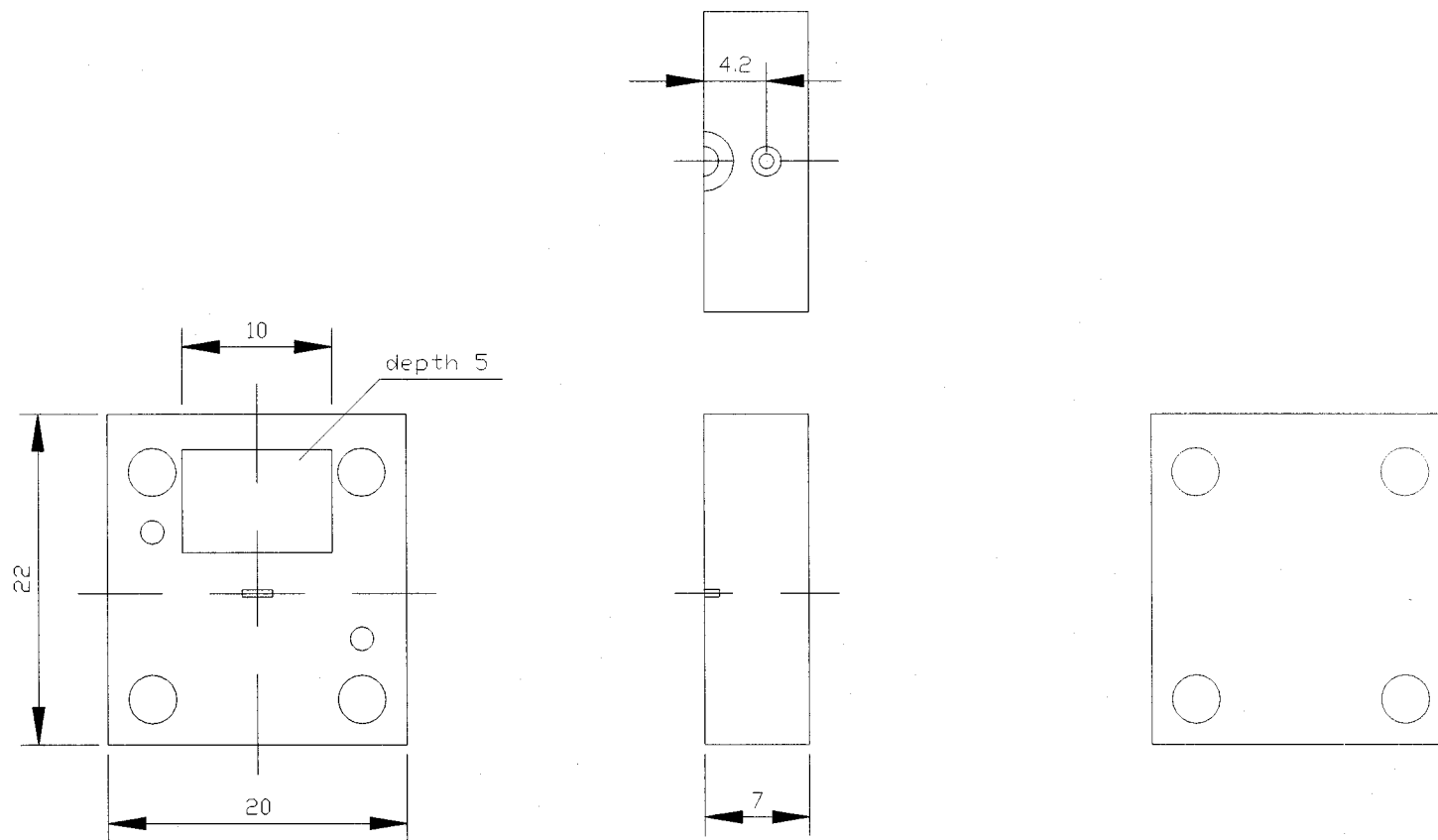
Figure 4.16 A drawing of a half part including the backshort cavity for the 190-300 GHz band SIS mixer block.

Taper structure
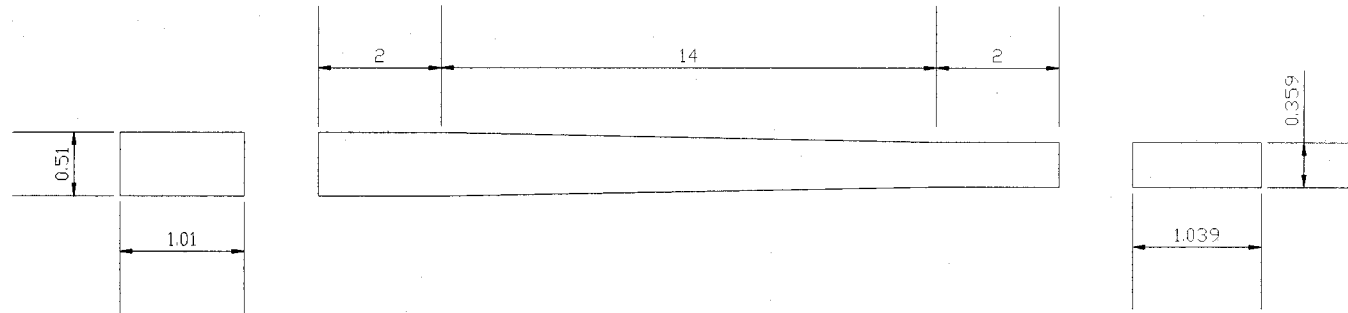
Chip slot
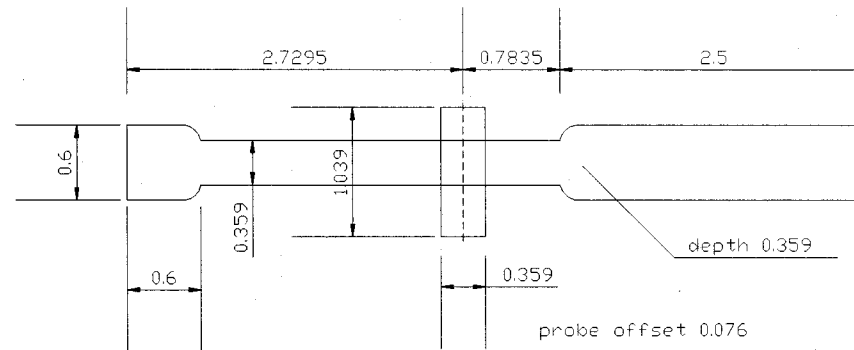
Figure 4.17 A drawing of the taper structure and the chip slot.
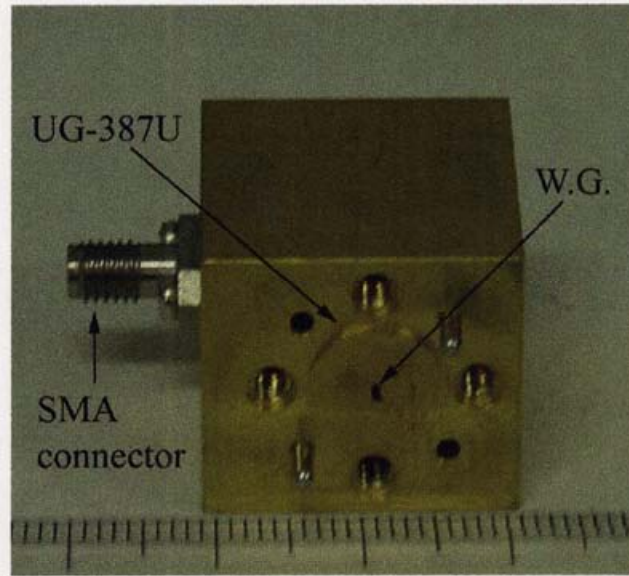
(a)
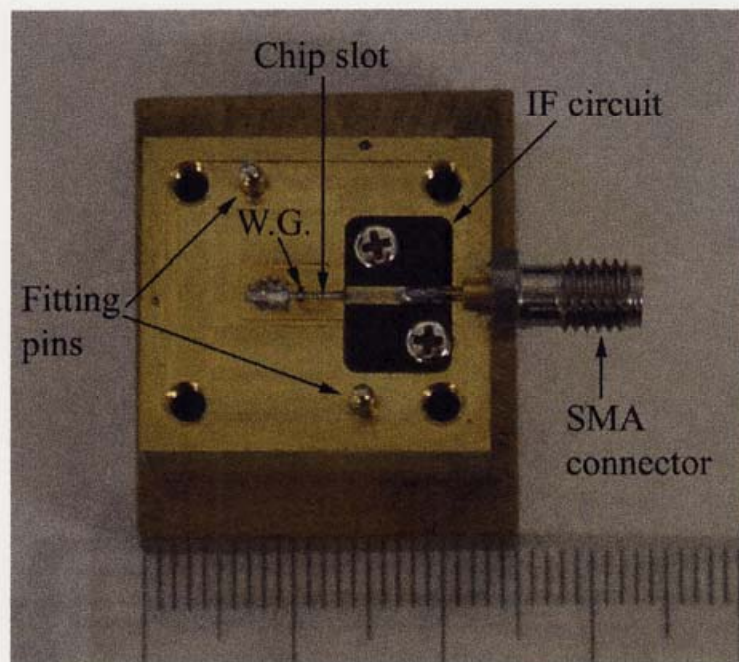
(b)

Figure 4.18 The photograph of the mixer block with side view (a) and inside view (b) for the 190-300 GHz band SIS mixer.

Table 4.1 Dimensions of junctions and spacings between all pairs of adjacent junctions.[a]

| Array	$A^{(1)}$	$A^{(2)}$	$A^{(3)}$	$A^{(4)}$	$A^{(5)}$	$L^{(1)}$	$L^{(2)}$	$L^{(3)}$	$L^{(4)}$
Inhomogeneous (Array A)	1.5	5.0	4.0	5.0	1.5	20.0	27.0	29.0	40.0
Inhomogeneous (Array B)	4.0	5.0	4.0	5.0	1.5	18.0	28.0	30.0	38.0
Inhomogeneous (Array C)	1.5	5.0	5.0	6.0	2.0	27.0	22.0	24.0	36.0
Inhomogeneous (Array D)	1.5	3.0	4.0	4.0	2.0	43.0	33.0	33.0	43.0
Homogeneous	1.5	1.5	1.5	1.5	1.5	67.0	67.0	67.0	67.0

a) A values are the dimensions of junctions in μm^2 and L values are the spacings between the respective pairs of adjacent junctions in μm.

Table 4.2 Dimensional parameters (units are in µm) of the waveguide-to-microstirp for 190-300 GHz SIS mixer.

Waveguide	1039 X 358
Chip slot	359 X 359
Substrate	340 X 170
Probe	$W_1/L_1 = 113/94$ $W_2/L_2 = 255/264$
DC/IF path	
high impedance line	$W/L = 19/113$
low impedance line	$W/L = 255/125$
Probe offset Δy	76

Chapter V

Fabrication of Nb/AlOx/Nb tunnel junction

5.1 Fabrication process

The photomask composed of three layers for the junction fabrication was designed with the aid of a commercial layout CAD software (LTL-100) [1]. The first layer is employed to pattern the trilayer (Nb/AlOx/Nb) including the waveguide probe, first quarter-wavelength impedance transformer, and RF choke filter. The second layer defines the junction pattern and the pattern of a dielectric layer (SiO_2/Al_2O_3) that is an insulating layer around junctions and that acts as the dielectric layer of the superconducting microstrip. The last layer fixes the pattern of the wiring layer, which functions as the conductor of the superconducting microstrips and again the RF choke filter connecting the top Nb layer and part of the base Nb layer.

The Nb/AlOx/Nb tunnel junctions were fabricated on a crystalline-quartz wafer with 35 mm in diameter and 0.3 mm in thickness in the clean-room facility of Nobeyama Radio Observatory (NRO), Japan. The fabrication process was basically a SNEP (Selective Niobium Etching Process) incorporating anodization around junctions in order to suppress the leakage current [2]. The outline of the fabrication process is completely illustrated in Fig. 5.1.

The trilayer of Nb/AlOx/Nb was formed by dc sputtering and thermal oxidation in an oxygen atmosphere without breaking vacuum. The Nb and Al were sequentially deposited in the sputtering room. The critical current density of junctions in the wafer is controlled by the pressure of the oxygen gas and oxidation time. For the 190-300 GHz

band SIS mixer, the Al was oxidized in a load-locked room with a 350-mTorr 10%O_2/Ar mixture for 30 min. The thickness of the base and counter Nb were 200 and 100 nm, respectively, and the thickness of the AlO_x was around 1 nm.

After the lift-off of the photoresist, a 70-nm SiO_2 layer was deposited on the whole wafer by RF sputtering to prevent the surface of the top Nb of junctions from being oxidized in the later anodization process. An SIS-junction mesa was formed by reactive ion etching (RIE) with CF_4. In order to avoid short-circuits at the junction edges, the periphery of the junctions were heavily anodized (~ 100 nm) and then 270-nm SiO_2 and 90-nm Al_2O_3 layers were deposited sequentially. Here the Al_2O_3 layer was employed to protect the SiO_2 layer from the next etching process (just before the wiring-layer deposition).

After the lift-off of the photoresist, the 70-nm SiO_2 layer on SIS junctions was removed by the RIE, and Ar plasma cleaning was performed to remove an oxidized layer of the surface of the counter Nb. Finally, the wiring Nb layer having a thickness of 675 nm was deposited and patterned.

After the fabrication process was completed, the wafer was firstly diced into several blocks with a (DISCO) dicing machine. The diced wafer was glued upside down on glass plate and its backside was then polished down to the desired thickness (170 μm for 190-300 GHz band SIS mixer) with a lapping machine. The polished wafer was finally diced into SIS mixer-chips, and the mixer chip was installed into a mixer block. For this designed photomask one fabrication will yield forty-two pieces of 90-180 GHz band SIS mixer-chips, sixty-six pieces of 190-300 GHz band SIS mixer-chips, and ninety pieces of 300-500 GHz band SIS mixer-chips.

5.2 DC characteristics

In the photomask, seven single-junctions with a dimension of 5×5, 3×3, 2×2, 1.75×1.75, 1.5×1.5, 1.25×1.25 and 1.0×1.0 μm^2 were arranged for estimating the critical current density and the reduction of the junction size due to the etching process during junction definition. The critical current density can be theoretically derived by V. Ambegaokar and A. Baratoff [3];

$$J_c = \frac{1}{R_n A}\left[\frac{\pi \Delta(T)}{2e}\right]\tanh\frac{\Delta(T)}{2kT}$$

$$\rightarrow \frac{\pi}{4}\frac{V_g}{R_n A} = \frac{\pi V_g}{4}\left(\frac{\sqrt{1/R_n}}{\sqrt{A}}\right)^2 \quad \text{for } T \approx 0\text{K}$$

(5.1)

where A is the dimension of a junction. Knowing the relation between $(1/R_n)^{1/2}$ and $A^{1/2}$, the critical current density can estimate by (5.1). The reduction of the junction size was examined by taking the fact that $R_n A$ should be constant, which means that $(1/R_n)^{1/2}$ should be a linear function of the length of one side of a junction square. Figure 5.2 shows the data and a linear fit for all single-junctions with the same recipe for junction patterning. Extrapolation of the linear fit indicates an over etch of 496 nm. In the design of the photomask, a margin of 200 nm was added to the length of one side of a junction square in the designed SIS mixers in advance by predicting the reduction of the junction size. Hence, the total reduction of the length of one side of a junction square in the SIS mixers can be estimated as 296 nm.

Figure 5.3 shows an optical micrograph of the 190-300 GHz inhomogeneous distributed junction array with five junctions. The DC I-V curve is shown in Fig. 5.4. The critical current density and normal-state resistance were 3.1 kA/cm^2 and 6.2 Ω, respectively. The discrepancy between the fabricated and the designed values of the normal-state resistance can be explained by the fact that the dimensions of the

fabricated junctions are a little less than those of the designed ones. Taking the reduction of 296 nm in the length of one side of a junction square into consideration, the relation is consistent. The extremely small sub-gap leakage current and strong nonlinearity were observed in the I-V characteristic, in which the ratio of the sub-gap resistance at 2.0 mV to the normal-state resistance was around 20 at 4.2 K.

References

[1] LTL-100, *An IC Layout System by Integrated Silicon Systems Inc.*, USA.

[2] T. Noguchi, A. Sakamoto, and S. Ochiai, "Fabrication of sub-micron SIS junctions", *Tech. Rep. IEICE*, **93**, 43 (1994).

[3] V. Ambegaokar and A. Baratoff, "Tunneling between superconductors", *Phys. Rev. Lett.*, **10**, 486 (1963).

1. Base electrode patterning

2. Tri-layer deposition

3. Lift-off and SiO$_2$ deposition

4. Junction patterning

5. Counter electrode etching and anodization

6. SiO$_2$ and Al$_2$O$_3$ deposition

7 Lift-off, SiO$_2$ etching and wiring layer deposition

8. Wiring layer patterning

9. Wiring layer etching and lift-off

Photoresist   Nb   AlOx   SiO$_2$

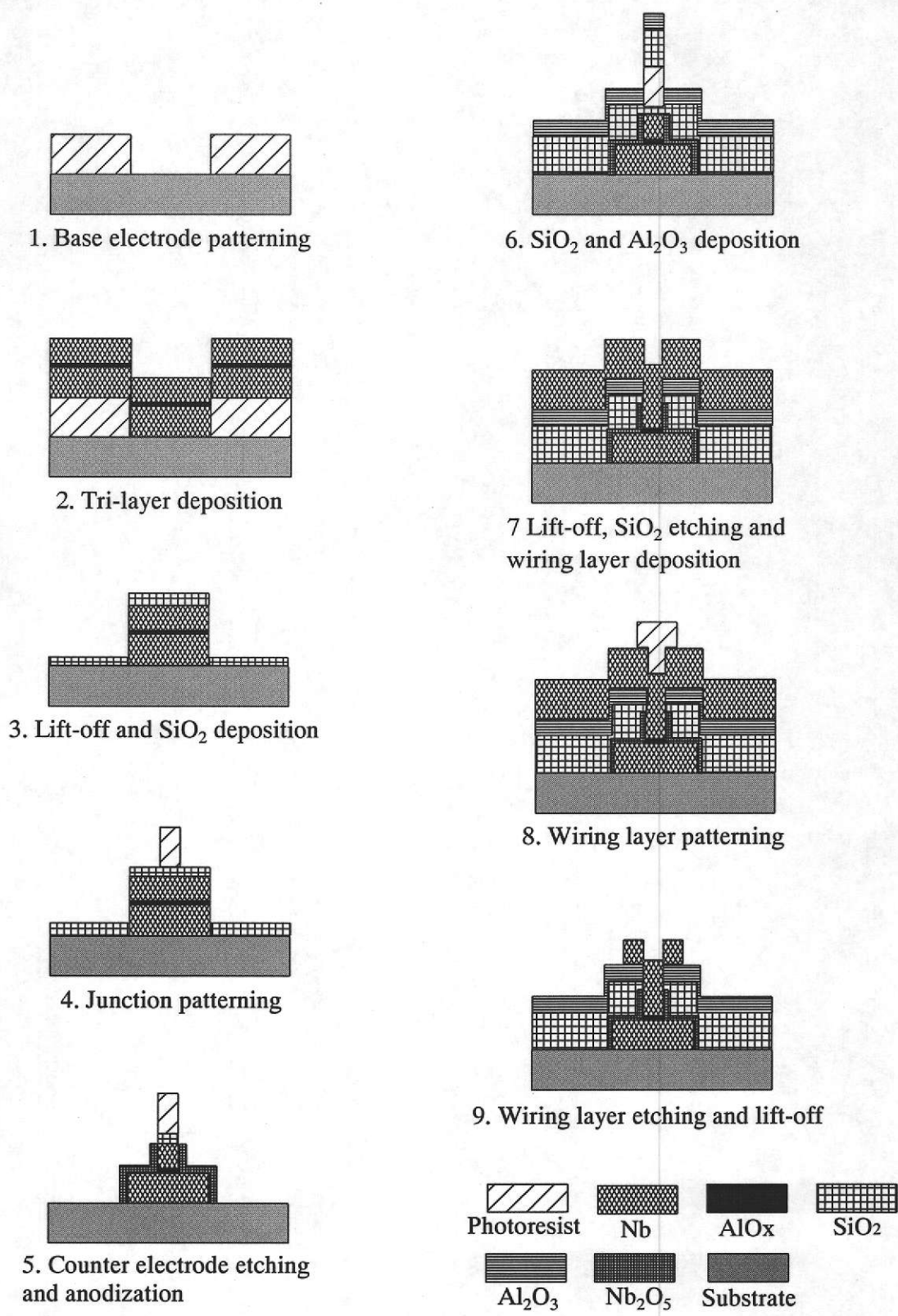Al$_2$O$_3$ Nb$_2$O$_5$ Substrate

Figure 5.1 Outline of the fabrication process of SIS junctions in the clean-room facility of Nobeyama Radio Observatory (NRO).
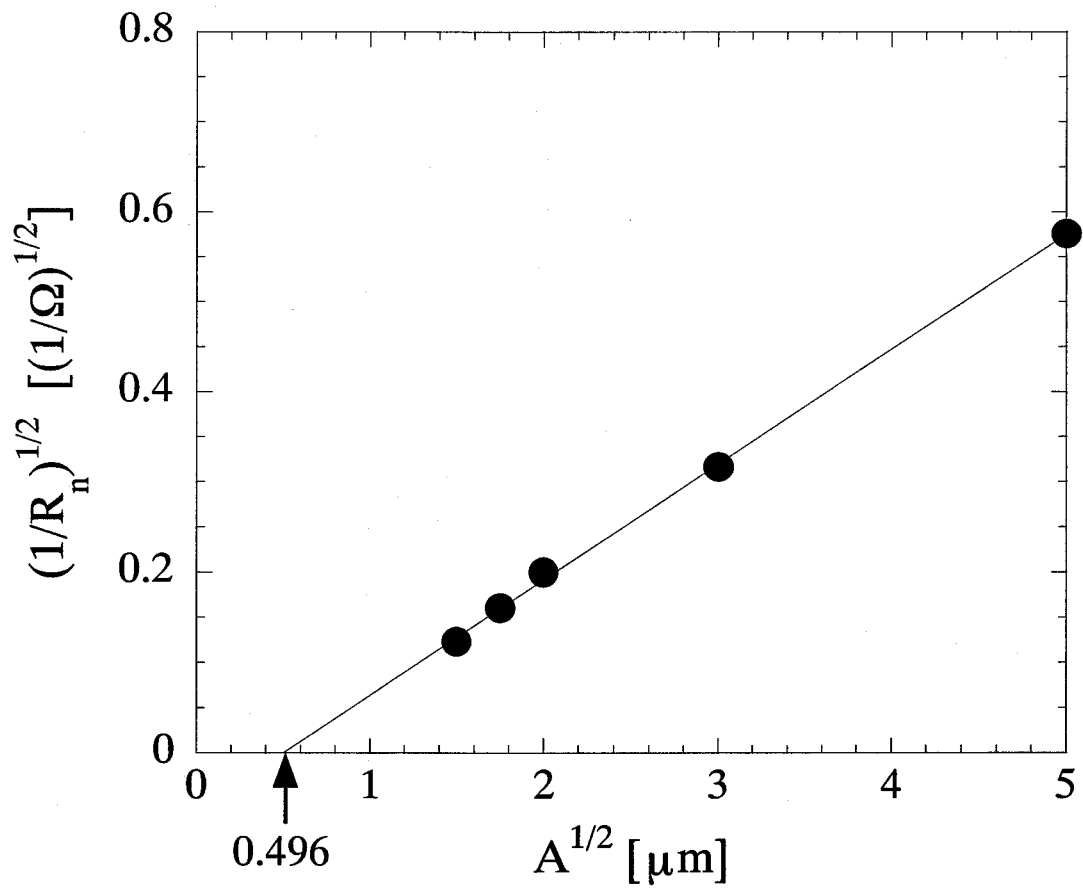
Figure 5.2 Estimation of the over etch for fabricated Nb/AlOx/Nb junctions. The junction area shrinks about 496 nm per dimension.

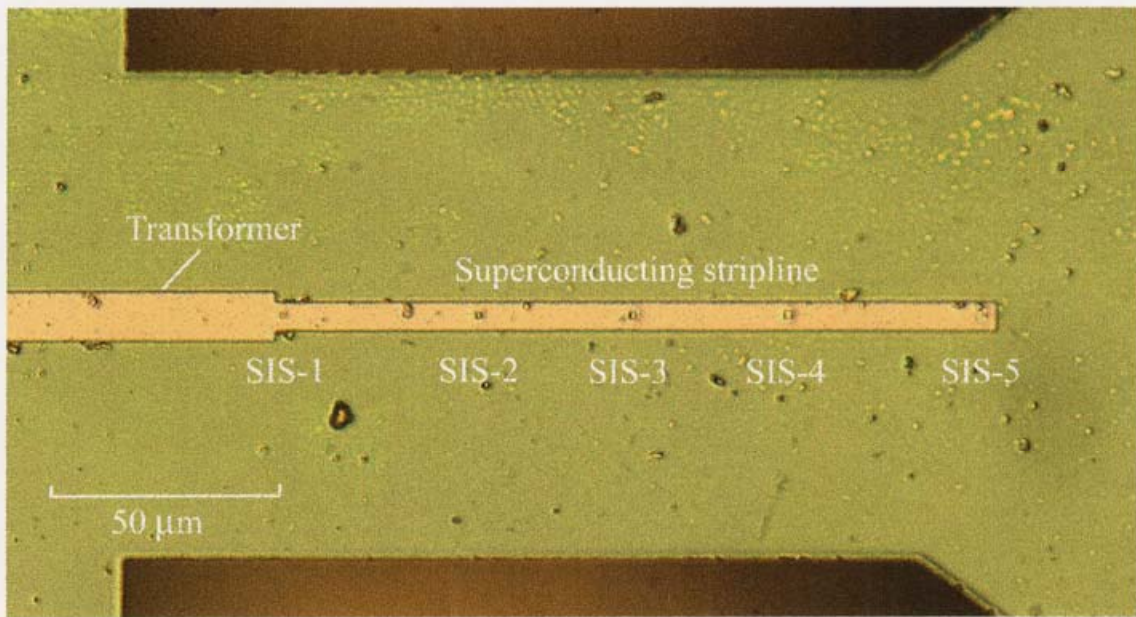Figure 5.3 An optical micrograph of the Nb/AlOx/Nb SIS mixer with the inhomogeneous distributed junction array. Five junctions are distributed along the superconducting microstrip.
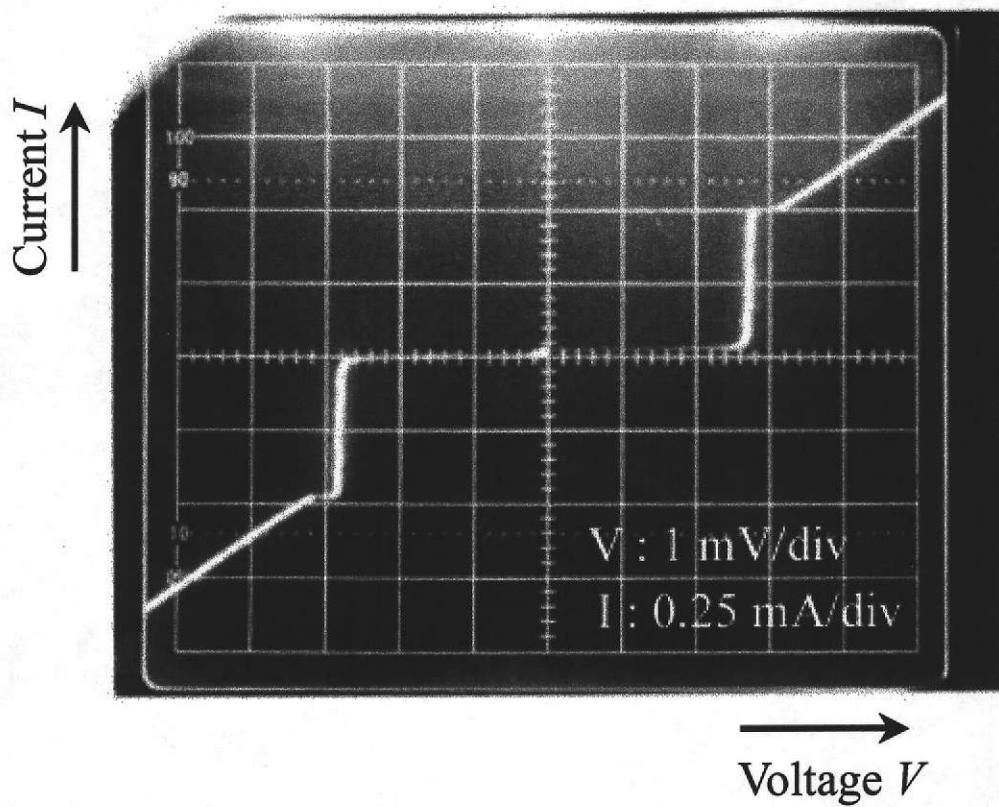
Figure 5.4 I-V characteristic of the 190-300 GHz band SIS mixer. The horizontal scale is 1 mV per division, and the vertical scale is 0.25 mA per division. The current density measured from the I-V curve and the junction size is 3.1 kA/cm^2.

Chapter VI

Experimental results of receiver performance

6.1 Introduction

In this chapter the experimental results of waveguide SIS mixers with inhomogeneous distributed junction arrays are presented. On the basis of design described in chapter IV, a few SIS mixers at different frequency bands were constructed and tested. One is the 110-180 GHz band SIS mixer, which was measured only in a very limited frequency range for lack of local oscillator source. The other one is the 190-300 GHz band SIS mixer, in which the receiver performance was measured by both a Fourier transform spectrometer (FTS) and heterodyne measurements. Detailed heterodyne measurements were made across the frequency range from 190 to 284 GHz.

6.2 Y-factor method

Noise temperature can be used to specify the noise generated in any two-port. Figure 6.1 shows a linear two-port terminated at its input by a source impedance Z_s, and at its output by a load Z_L. The two-port has a transducer conversion gain G_t, defined as the power delivered to the load Z_L divided by the power available from the source Z_s. The temperature of the input termination is T_{in}. The noise power P_L in a bandwidth B delivered by the input termination and the two-port to the load is

$$P_L = G_t k \left(T_{in} + T_N \right) B,$$ (6.1)

where T_N is the two-port's noise temperature.

The receiver shown in Fig. 6.2 has two terminations and a switch connected to its input

and a power meter to its output. The terminations have different noise temperature. T_{hot} is the "hot" termination, the one at the higher temperature. T_{cold} is the "cold" termination, which is at lower temperature. The "power meter" is used to indicate relative power levels and therefore need not be a power measuring device. It can, for example, be an uncalibrated detector and precision attenuator.

The measurement is made by first switching the cold termination to the receiver input. The output power is

$$P_{cold} = kG_t (T_{cold} + T_{RX})B,$$
(6.2)

where T_{RX} is the receiver noise temperature. The hot termination is then switched to the input, and the noise output power is

$$P_{hot} = kG_t (T_{hot} + T_{RX})B.$$
(6.3)

Dividing (6.3) by (6.2) obtains

$$Y = \frac{P_{hot}}{P_{cold}} = \frac{T_{hot} + T_{RX}}{T_{cold} + T_{RX}},$$
(6.4)

which depends only on the hot- and cold-load temperatures and the ratio of the output powers. The receiver noise temperature T_{RX} is found by solving (6.4):

$$T_{RX} = \frac{T_{hot} - Y T_{cold}}{Y - 1}$$
(6.5)

This is called the Y-factor method.

6.3 Receiver noise measurements for 110-180 GHz band SIS mixer

6.3.1 Mixer layout

An SIS mixer with an inhomogeneous distributed junction array was designed in the frequency range from 110 to 180 GHz, which covers a full band of the WR-7 waveguide, according to the method as described in chapter IV [1]. The number of

junctions, the width of the superconducting microstrip and the critical current density of a junction set to be five, 8.0 μm and 2 kA/cm^2, respectively. The dimensions of junctions and spacings between all pairs of adjacent junctions are listed in Table 6.1, and the calculated reflection coefficient at the input port of the inhomogeneous distributed junction array as a function of frequency is shown in Fig. 6.3. The equivalent normal-state resistance of the array is 7.7 Ω.

The conversion gain is extremely sensitive to the IF load resistance R_{IF} as shown in Fig. 6.4. According to an analysis by Shi *et al.* [2], the optimum R_{IF}/R_n value is found to lie between 0.5 and 1.5 at low frequencies (around 100 GHz). In the inhomogeneous distributed junction array, the R_{IF}/R_n value becomes very large if the IF termination of 50 Ω, which is the input impedance of the following IF amplifier, is adopted. The larger R_{IF}/R_n value will cause the lower output coupling efficiency and conversion gain at around 100 GHz. Therefore the IF termination of 30 Ω and the two-stage IF impedance transformer in order to match the impedance of 50 Ω of amplifier were adopted in the 110-180 GHz band SIS mixer. Figure 6.5 shows the measured return and insertion losses of the IF circuit. At 1.4 GHz, the IF circuit showed a poor match, wronger than -10 dB in the return loss.

The mixer chip is essentially scaled-up 190-300 GHz band SIS mixer, with a scaling factor of 1.8. A corrugated horn and cross-guided coupler with the output port of a WR-8 waveguide were used as a feed horn and for coupling the RF signal with LO signal.

The 110-180 GHz band SIS mixer was fabricated according to the fabrication process described in chapter V. The critical current density and the normal-state resistance of the fabricated mixer were 2.8 kA/cm^2 and 7.0 Ω, respectively. Figure 6.6

shows the DC I-V characteristic. The ratio of the sub-gap resistance at 2.0 mV to the normal-state resistance is around 14 at 4.2 K.

6.3.2 Measurement set-up

Figure 6.7 sketches the configuration of the measurement set-up for the 110-180 GHz band SIS mixer. The RF signal enters the cryostat through a 1-mm thick Teflon vacuum window and an infrared heat filter at 77 K, and is fed to a corrugated horn. The RF signal was coupled to the LO signal through a 20-dB cross-guided coupler and was then guided to the mixer block, which had been cooled to 4.2 K. A Gunn oscillator of 94-115 GHz and a doubler with a Gunn oscillator of 65-73 GHz were used as the LO source. A DC bias was supplied to the SIS junctions through a commercial bias tee. The IF output signal was firstly amplified by a HEMT amplifier cooled to around 20 K, which is able to amplify over 500 MHz wide centered at 1.5 GHz, through an isolator, and it was further amplified by a post-amplifier at room temperature. The IF signal was finally fed to a power meter through an adjustable attenuator in order to calibrate the IF output power and a band-pass filter. The equivalent input noise temperature of the overall receiver can measure by the Y-factor method using room temperature (295 K) and liquid-nitrogen-cooled (77 K) loads as RF signal sources.

Prior to carrying out Y-factor measurements, the linearity of the measurement set-up should be examined in order to acquire a reliable Y-factor. Using a precise step (1 dB) attenuator to calibrate the measured Y-factor gives more reliable results.

6.3.3 Experimental results of the 110-180 GHz band SIS mixer

The IF-output-power characteristics to hot and cold loads, along with the DC I-V

characteristics with and without LO of the 110-180 GHz band SIS mixer as a function

of bias voltage, are exhibited in Figs. 6.8a-c for three different LO frequencies of 115,

130 and 140 GHz, respectively. When LO power was applied, the photon-assisted

tunneling steps with a spacing of $hf/2e$ were clearly visible, for example, it was 0.58 mV

intervals at 140 GHz. In the case of the response at the 140 GHz, a maximum Y-factor

of 4.2 dB was obtained at the bias voltage of 2.3 mV and corresponded to a double

sideband (DSB) receiver noise temperature of 55 K, which is about eight times as large

as the quantum noise temperature.

The overall noise temperature of the receiver system was measured on the first

photon step below the gap voltage at several frequencies from 100 to 146 GHz. The

DSB receiver noise temperature is plotted in Fig. 6.9 as a function of LO frequency. No

corrections were made for losses in front of the receiver. The degradation of the receiver

noise temperature in the lower frequencies is because of the degradation of the input

coupling efficiency in the waveguide-to-microstrip transition.

It is found from Fig. 6.9 that the receiver noise temperature is relatively large over

the range of frequencies shown. It is well known that the receiver noise temperature can

separate into three major components: noise temperature due to input losses T_{in}, mixer

noise temperature T_{mix}, and IF noise temperature divided by the mixer conversion gain

T_{IF}/G_m. Figure 6.10 shows the noise temperature, $T_{in} + L_{RF}T_{mix}$, in front of the IF

network as a function of LO frequency, where L_{RF} is input losses. The noise temperature

in front of the IF network is less than 25 K in the frequency range from 110 to 146 GHz.

This value is as large as that of the conventional SIS mixer published up to present. The

remained noise temperature, which is the difference between the receiver noise

temperature and the noise temperature in front of the IF network, is the contribution

from the mixer conversion gain and the IF network. The noise temperature of the HEMT amplifier used in this measurement was around 20 K, which is larger than the typical noise temperature of IF amplifier. In addition to the large noise temperature of the HEMT amplifier, it can be considered that the conversion gain of the mixer extremely degraded [3]. The mixer conversion gain is influenced by the RF input and IF output coupling efficiencies, whereas the mixer noise temperature only by the input coupling efficiency. Therefore large noise temperature of the receiver system is possibly resulted from the involvement of the poor HEMT amplifier and IF circuit with two-stage IF transformer.

Figure 6.9 also shows the DSB receiver noise temperature of an SIS mixer with PCTJ. The PCTJ was designed at the critical current density of 4 kA/cm^2 and $\omega R_n C_j$ product of 4, but the fabricated one was the critical current density of 2.7 kA/cm^2. Although the large receiver noise temperature of PCTJ is observed in Fig. 6.9 because of the poor matching between the source impedance and the input impedance of PCTJ, the bandwidth performance of PCTJ is comparable with that of the inhomogeneous distributed junction array because those have the almost same critical current density. It is clearly visible in Fig. 6.9 that the broader bandwidth than that of PCTJ can be obtained in the inhomogeneous distributed junction array.

It was experimentally proven that SIS mixers with inhomogeneous distributed junction arrays have extremely broadband performance. The DSB receiver noise temperature less than 80 K was obtained in the frequency range from 114 to 146 GHz and the minimum noise temperature of 55 K was obtained at 140 GHz. In this experiment, no data was obtained above 146 GHz because no LO source was available.

6.4 Receiver noise measurements for 190-300 GHz band SIS mixer

6.4.1 Input coupling efficiency of the SIS mixer

6.4.1.1 Fourier transform spectroscopy

Knowing the information of the tuning bandwidth prior to the measurement of receiver noise temperature is very invaluable. The tuning characteristic can be evaluated by Fourier transform spectrometer (FTS) using the SIS mixer as a direct detector. FTS is a standard technique for broadband low-resolution spectroscopy in the near-infrared and has recently been used in the submillimeter-wave regime of the spectrum, for example, the measurement of submillimeter-wave atmospheric opacity spectra [4].

The FTS consists of a Martin-Puplett interferometer using wire grids as polarizers and an Hg arc lamp as a broadband radiation source [5]. A schematic diagram and photograph of the FTS system are shown in Fig. 6.11 and Fig. 6.12, respectively. The FTS was designed to optimize millimeter- and submillimeter-wave efficiencies with a large beam size of 75 mm in diameter and a short optical path to minimize diffraction losses. One of the corner reflectors of the FTS was driven continuously by a magnetic coil and controlled by a He-Ne sub-interferometer. The sub-interferometer signal was also used as a sampling clock of the detector signal. Scan speed was set to about 15 mm/sec with forward and backward scans centered at zero path difference. The scan length was ±16.5 mm. A frequency resolution of 0.5 cm^{-1} was achieved when the interferogram was apodized and Fourier transformed. The temperature of the FTS was stabilized at 20 °C for stable movement of the corner reflector and to minimize fluctuation of the offset signal of the FTS. One set of scans took approximately 4 seconds and 10 consecutive scans were integrated to give a sufficient signal-to-noise ratio.

The SIS mixer was cooled to 4.2 K by unpumped liquid helium in a cryostat and was set in front of the Teflon vacuum-window. In the measurements, the mixer was voltage-biased at a constant value just below the gap voltage and was used as a direct detector. The current was modulated by scanning the movable mirror. In the principle of video detection, the tunneling current can be observed when the input radiation, which is generated from the Hg arc lamp, is applied to the detector through the corrugated horn. The current as the video signal was read out from current monitor of DC bias circuit, and then the interferogram was generated with the information of the path-length difference. The FTS response as a function of frequency can be obtained by performing the Fourier transformation to the interferogram. The useful bandwidth is determined by the sensitivity of the detector and the frequency dependence of the optical system.

6.4.1.2 Results and discussion

The FTS response is directly related to the input coupling efficiency of the RF signal to the mixer. It is well-known that the shape of the FTS response as a function of frequency strongly correlated to the receiver noise temperature as a function of frequency and that the minimum receiver noise temperature can be obtained at the frequency where the maximum peak of the FTS response is observed.

Figure 6.13 shows the measured FTS response and the calculated input coupling efficiency of the inhomogeneous distributed junction array. Since an SIS used as a direct detector is a photon-counting device rather than a frequency-independent power detector, a correction for the change in responsivity, which has a $1/f$ dependency over the frequency range of interest, is necessary. In this plot the vertical scale of the measured FTS data was adjusted to give the best match to the calculated coupling

efficiency. The measured FTS response is in moderate agreement to the calculated input coupling efficiency. It is found from the FTS data that the 3-dB bandwidth is from 193 to 276 GHz and the low noise performance will be obtained in the frequency range. Especially, the best noise temperature can be expected at frequencies around 210 and 240 GHz.

The comparison of the FTS responses of the inhomogeneous and homogeneous distributed junction arrays with five junctions are shown in Fig. 6.14. The homogeneous distributed junction array was fabricated on the same wafer with the inhomogeneous distributed junction array. Therefore it can be supposed that the critical current density and the shrinkage in the length occurred in the junction definition are identical in both arrays. Although the sharp dips were observed in the homogeneous distributed junction array at frequencies around 210 and 280 GHz, where the receiver noise temperature would extremely increase, those are considerably improved in the inhomogeneous distributed junction array as predicted in the theoretical analysis.

6.4.2 Receiver noise measurement for 190-300 GHz band SIS mixer

6.4.2.1 Measurement set-up and IF circuit

The measurement set-up is fundamentally similar to that for the 110-180 GHz band SIS mixer. The photograph of the measurement system is shown in Fig. 6.15. The RF signal was quasi-optically coupled to the LO signal through a 50-μm thick Mylar film as a beam splitter and a corrugated horn, which was connected to the mixer block, through a 25-mm thick Mylar film as a vacuum window. The Mylar film has the refractive index of 1.69. The calculated transmissivity of the beam splitter and the vacuum window is shown in Fig. 6.16. A doubler with a Gunn oscillator at 77-117 GHz

and a tripler with Gunn oscillator at 86-90 GHz and 88-96 GHz were used as LO sources. A permanent magnet was attached to a side wall of the mixer block in order to suppress the Josephson current. The strength of the magnetic field is about 650 Gauss at the junctions. The IF signal was amplified by a HEMT amplifier cooled to around 20 K without an IF impedance transformer. The IF port of the SIS mixer chip was directly connected to the IF circuit with a 50-Ω microstrip by Al wire bonding. Figure 6.17 shows the measured return and insertion losses of the IF circuit. The result showed a good match, better than -15 dB in the return loss and -0.1 dB in the insertion loss, in the frequency range of 1-2 GHz.

6.4.2.2 Noise performance and discussion

The noise temperature was estimated by the standard Y-factor method using the black body radiation on 295-K and 77-K loads as the RF signal source. The IF responses to hot- and cold-loads as a function of bias voltage and the DC I-V characteristics with and without LO are exhibited in Fig. 6.18(a)-(c) for three different LO frequencies of 210, 230, and 260 GHz, respectively. Photon assisted tunneling steps can be clearly observed in three LO-pumped DC I-V curves. A 4-dB reference curve, which is the IF output power for the 295-K input in association with an IF attenuation of 4 dB, is also presented to calibrate the ratio of the two IF output-power levels. The figure indicates that excellent noise performance is obtained at 210 GHz, and that good noise performance is achieved at 230 and 260 GHz. In the case of 210 GHz (Fig. 6.18a), maximum Y-factor of 4.3 dB was obtained at a bias voltage of 2.1 mV. This gives a DSB receiver noise temperature of 47 K, which is approximately five times as large as the quantum limited noise, ~ $5hf/k$.

The IF-frequency dependence of the mixer noise temperature and the conversion gain would seriously affect the receiver noise temperature. The bandwidth characteristic of IF output was measured by using the spectrum analyzer at a fixed LO frequency of 210 GHz. Figure 6.19 shows the IF-frequency dependence of receiver noise temperature. The serious increase of the receiver noise temperature was not found in the frequency range from 1.1 to 1.7 GHz, excluding around 1.6 GHz. The degradation of the receiver noise temperature at 1.6 GHz was due to the used isolator inserted between the mixer and the HEMT amplifier. It was found that the IF bandwidth of the SIS mixer mainly depended on the gain bandwidth of the HEMT amplifier.

It is of great significance in the development of SIS mixer to estimate the necessary LO power level to pump the junction [6]. The required LO power can be estimated by comparing the theoretical calculation and measured I-V curve. The LO power can be derived by the following equation,

$$P_{LO} = \frac{V_{LO}^2}{2R_{in}} \approx \frac{1}{2R_n} \left(\frac{\alpha h f}{e} \right)^2, \tag{6.6}$$

where V_{LO} and R_{in} are the LO voltage across the junction and the input resistance of the mixer, respectively. This equation suggests that the required LO power increases in proportion to the square of the signal frequency and inversely proportional to the normal-state resistance. In published experimental values, the observed P_{LO} is in the range from 1 nW to 30 μW [7]. The lower values of P_{LO} are a great convenience for SIS mixers, especially at terahertz frequencies. Figure 6.20 shows the photon-assisted tunneling step measured at 210 GHz and the calculation values of the first photon-assisted tunneling step when setting α to 0.8, 0.9, and 1.0. It is found from Fig. 6.20 that the height of the photon-assisted tunneling step calculated in the case which

set the value of α to 0.9 fits measured value most. Since the normal-state resistance of the inhomogeneous distributed junction array is 6.2 Ω, the required LO power to pump the array can be estimated as 49 nW using (6.1). This value is substantially same for the conventional SIS mixers with high critical current densities, and this type of mixer would be able to pump enough by superconducting local oscillators such as Josephson oscillators and flux-flow oscillators (FFO) [8, 9].

The receiver noise temperature and FTS response as a function of frequency are shown in Fig. 6.21. These measurements were performed using a corrugated feed horn with WR-4 waveguide (1.01-mm wide and 0.51-mm high). It was found that the bandwidth characteristic of the receiver noise temperature was in good agreement with that of the FTS response. The DSB receiver noise temperature of $5hf/k$ was obtained in the frequency range from 202 to 270 GHz and the minimum receiver noise temperature was 47 K at 210 GHz.

One may think that the SIS mixer with the inhomogeneous distributed junction array is inferior to that with the homogeneous distributed junction array reported by Shi et al. [10], which shows about four times the quantum limited noise in the minimum receiver noise temperature. The receiver noise temperature of the SIS mixer with the inhomogeneous distributed junction array, however, is less dependent on frequency in the band for the sacrifice of the minimum receiver noise temperature, whereas that of the homogeneous distributed junction array extremely fluctuates in the band. The frequency-independent performance of the receiver will be quite useful in the practical application such as astronomical and atmospheric observations.

The degradation of the receiver noise temperature and FTS response at lower frequencies was mainly caused by the degradation of the input coupling efficiency in

the waveguide-to-microstrip transition, as shown in Fig. 4.8. The receiver performance, especially the input coupling efficiency, is sensitively varied to the position of the waveguide probe. Figure 6.22 shows the receiver noise temperature and FTS response in case that the probe position is shifted 10 μm toward to the IF port from the position obtained the result in Fig. 6.21. The FTS responses were normalized to each maximum value. It is found that the operation band was shifted toward to lower frequency region, also the noise temperature slightly increased over the band, and this indicates that a difference from the designed position of the probe brings the degradation of the input coupling efficiency.

In the measurements performed using the WR-4 corrugated feed horn, however, degradation of the receiver noise temperature and FTS response was found above 270 GHz. In order to find the cause of the degradation, a noise temperature due to input losses T_{in}, mixer noise temperature T_{mix}, and conversion gain G_m were estimated using standard measurement techniques [11]. The shot-noise produced by the linear resistance of the I-V curve above the gap voltage is used to calibrate the IF system (Appendix C). From this calculation, the IF system noise of $T_{IF} = 10.4$ K was obtained. Using this value, the mixer noise temperature and conversion gain can be estimated from the measured IF responses to hot- and cold-loads at each frequency. T_{in} can be determined by the intersecting lines technique [12, 13] (Appendix C). In this technique receiver IF output powers are measured for each load temperature of 77 K and 295 K as a function of LO power level. Varying the LO power has the effect of varying the mixer conversion gain. Figure 6.23 shows the results at LO frequency of 210 GHz for the procedure of the intersecting lines technique as an example. The IF output power is plotted against the load temperature. The straight line connecting two points plotted for

77 K and 295 K is extrapolated to the negative region of the load temperature axis for each LO power level. As shown in Fig. 6.23, the extrapolated lines intersect almost at a single point. The temperature corresponding to this intersecting point is the input noise temperature due to input losses, which is about 20 K. The input noise temperature obtained in the same way as a function of frequency is shown in Fig. 6.24. In the figure, the noise contribution by Mylar films using as the beam splitter and the vacuum window is also shown.

Figure 6.25 shows the estimated noise contribution as well as the calculated mixer noise temperature and conversion gain as a function of frequency. In the calculation of mixer noise temperature and conversion gain, the dimensions of junctions used those of the fabricated mixer. The calculation results are in reasonable agreement with the measured data. The disagreement between the calculated and measured conversion gain at lower is due to excluding the input losses in the calculation. It was found that the mixer noise temperature was still low at frequencies above 270 GHz, and that less than 26 K (DSB) in the frequency range from 200 to 282 GHz. The noise temperature due to input losses, however, considerably increased at frequencies above 270 GHz as shown in Fig. 6.24. It can be considered for the reason that the additional losses are occurred in the WR-4 waveguide, in which at frequencies above 270 GHz, the electromagnetic wave is impossible to propagate with TE_{01}-mode only and undesirable modes occur [14]. Therefore, the receiver noise temperature and FTS response were measured using the WR-3 corrugated horn, which shows a lower loss than WR-4 corrugated horn at frequencies above 270 GHz, in stead of the WR-4 corrugated horn. The results are shown in Fig. 6.26 (Fig. 6.21 is overlapped for the comparison). It was found that the receiver noise temperature and the FTS response were greatly improved at frequencies

above 270 GHz by using the WR-3 corrugated horn. If the RF input circuit and mixer block scaled by a smaller value than that used in this work, and the WR-3 corrugated horn are available, the receiver performance will be more improved.

A DSB receiver noise temperature about five times as large as the quantum limited noise was obtained in the frequency range from 202 to 284 GHz by using WR-4 and WR-3 corrugated horns. From the above discussion, it is apparent that the SIS mixer itself with the inhomogeneous distributed junction array has a quite broad bandwidth at least from 200 to 284 GHz, in spite of its low critical current density. The frequency limit for this SIS mixer can not be clearly recognized since the frequency is usually limited by the RF input circuit, which includes a waveguide, a feed horn and a waveguide probe. If those limitation do not exist or can be removed by improving the RF input circuit, the SIS mixer will operate in the bandwidth from 190 to 300 GHz predicted by the theoretical analysis.

Finally, the receiver noise performance for the IF amplifier network with 2 GHz bandwidth centered at 6 GHz is shown in Fig. 6.27 as a function of LO frequency. The receiver noise temperature for the IF frequency of 6 GHz increased about twice as compared with that for the IF frequency of 1.4 GHz. The SIS mixer with the inhomogeneous distributed junction array has a large output capacitance, as discussed in Chapter IV. Therefore, the degradation of the output coupling efficiency to the IF amplifier is considered as the main cause of the degradation of the receiver noise in the case of the IF frequency of 6 GHz.

6.5 Conclusions

The results of the receiver performance of the 110-180 GHz and 190-300 GHz

bands SIS mixers were described experimentally and analytically in this chapter. The 110-180 GHz band SIS mixer showed the DSB receiver noise temperature less than 80 K in the frequency range from 114 to 146 GHz, but no data was obtained above 146 GHz because no LO source was available. The contribution of the IF network for the 110-180 GHz band SIS mixer was analyzed quantitatively. From the analysis, it was found that the noise temperature of the used IF amplifier was larger than 20 K, which is about four times as large as the typical value, and the conversion efficiency was degraded due to the IF circuit, in which the large return loss was observed. The mixer itself showed the low-noise and broadband performance.

The 190-300 GHz band SIS mixer showed the DSB receiver noise temperature of $5hf/k$ in the frequency range from 202 to 284 GHz using WR-4 and WR-3 corrugated horns. The large increase of noise occurred in the homogeneous distributed junction array disappeared in the mixer. The experimental results for the 190-300 GHz band SIS mixer were analyzed quantitatively by breaking down the receiver noise temperature into the contributions due to the input noise, mixer noise, and IF system. It can be concluded that the bandwidth of the SIS mixer with the inhomogeneous distributed junction array was mainly dominated by that of the RF input circuit such as the input waveguide and the waveguide-to-microstrip transition.

References

[1] M. Takeda and T. Noguchi, "Performance of inhomogeneous distributed junction arrays", *Applied Superconductivity*, 167, 639 (1999).

[2] S. -C. Shi, J. Inatani, T. Noguchi, and K. Sunada, "Analytical predictions for the

optimum operating conditions of SIS mixers", *Int. J. Infrared & Millimeter Waves*, **14**, 1273 (1993).

[3] M. Takeda, S. Asayama, T. Noguchi, and H. Ogawa, "Broadband SIS mixers with inhomogeneous distributed junction arrays", *in Proc. 9th Int. Conf. Terahertz Electronics*, in press.

[4] D. H. Martin, "Polarizing (Martin-Puplett) interferometric spectrometers for the near- and submillimeter spectra", *Infrared and Millimeter Waves*, **6**, Subsidiary of Harcourt Brace Jovanovich (1982).

[5] H. Matsuo, A. Sakamoto, and S. Matsushita, "FTS measurements of submillimeter-wave atmospheric opacity at Pampa la Bola", *Publ. of the Astronomical Society of Japan*, **50**, 359 (1998).

[6] V. P. Koshelets, Russian Academy of Sciences, Moscow, Russia, personal communication (2001).

[7] J. R. Tucker and M. J. Feldman, "Quantum detection at millimeter wavelengths",

[8] A. Kawakami, Y. Uzawa, and Z. Wang, "Josephson array oscillators with microstrip resonators", *IEEE Trans. Applied Superconductivity*, **7**, 3126 (1997).

[9] V. P. Koshelets, S. V. Shitov, L. V. Filippenko, H. Golstein, T. de Graauw, W. Luinge, H. Schaeffer, and H. van de Stadt, "First implementation of a superconducting integrated receiver at 450 GHz", *Appl. Phys. Lett.*, **68**, 1273 (1996).

[10] S. -C. Shi, T. Noguchi, J. Inatani, Y. Irimajiri, and T. Saito, "Experimental results of SIS mixers with distributed junction arrays", *IEEE Microwave and Guided Wave Lett.*, **8**, 381, (1998).

[11] D. P. Woody, R. E. Miller, and M. J. Wengler, "85-115 GHz receiver for radio astronomy", *IEEE Trans. Microwave Theory Tech.*, **33**, 90 (1985).

[12] R. Blundell, R. E. Miller, and K. H. Gundlach, "Understanding noise in SIS receivers", *Int. J. IR & MM Waves*, **13**, 3 (1992).

[13] Q. Ke and M. J. Feldman, "A technique for noise measurements of SIS receivers", *IEEE Trans Microwave Theory Tech.*, **42**, 752 (1994).

[14] M. Takeda and T. Noguchi, "A 200-285 GHz waveguide SIS mixer with an inhomogeneous distributed junction array", *IEEE Trans. Microwave Theory Tech.*, **50** (2002), in press.
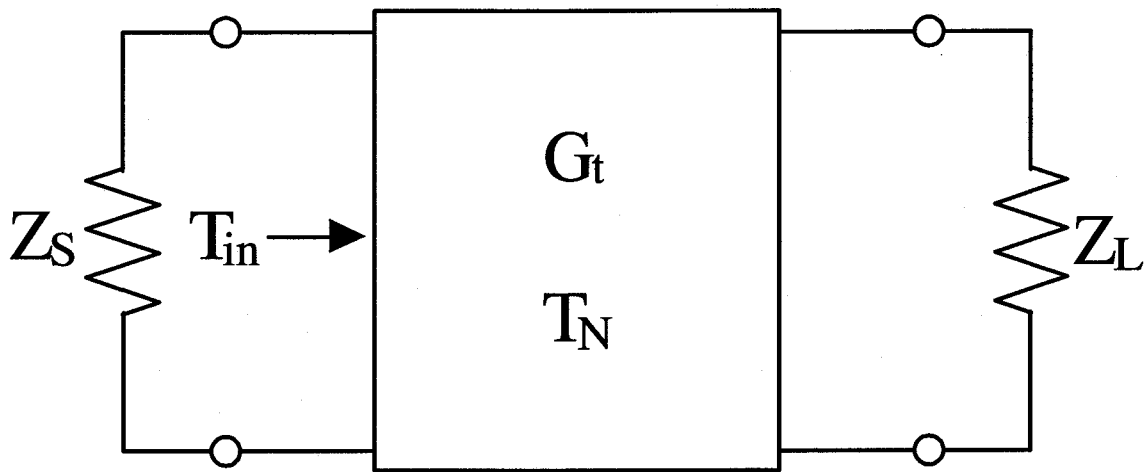
Figure 6.1 General model of terminated two-port.
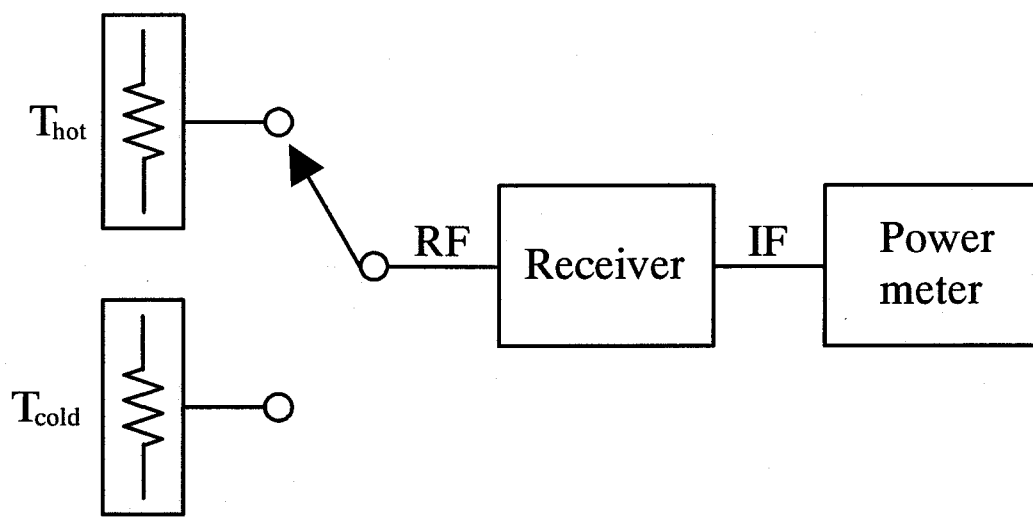
Figure 6.2 Noise-temperature measurement system.
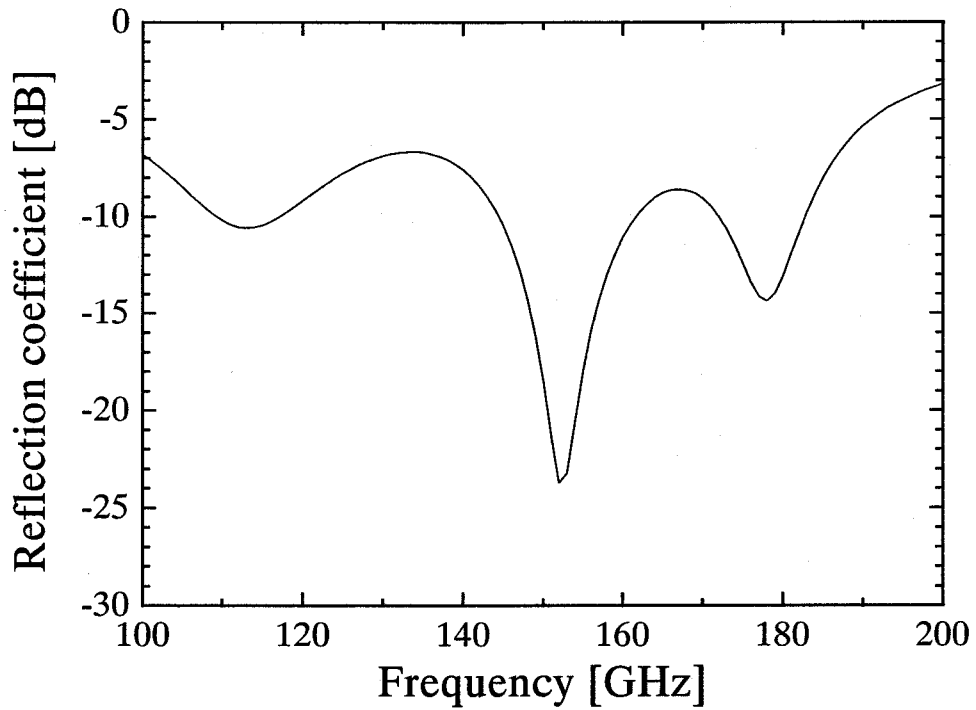
Figure 6.3 Calculated reflection coefficient at the input port of the inhomogeneous distributed junction array with five junctions. The dimensions of junctions and the spacings between every two junctions were optimized in the frequency range from 110 GHz to 180 GHz. The critical current density is 2.0 kA/cm^2.
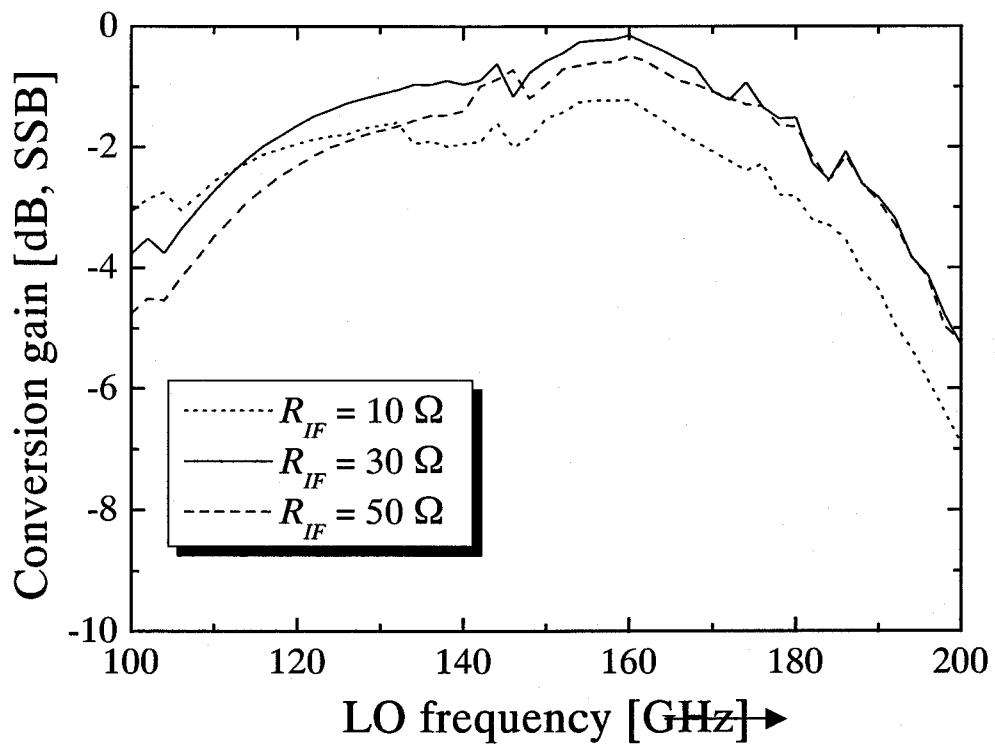
Figure 6.4 Calculated dependence of the conversion gain on the IF termination.
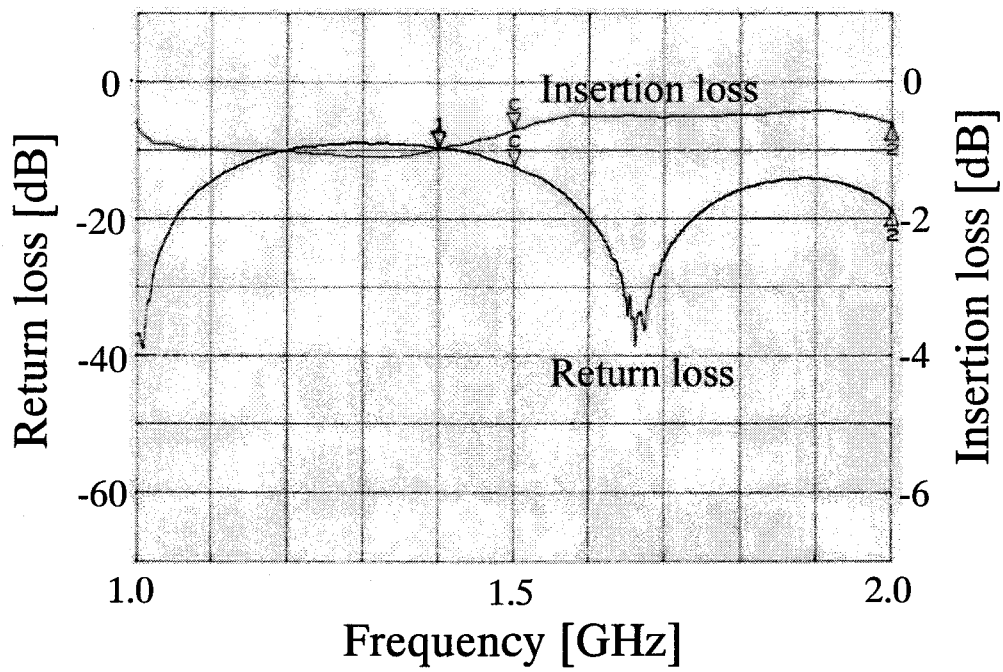
Figure 6.5 Return loss and insertion loss of the IF circuit for 110-180 GHz band SIS mixer.
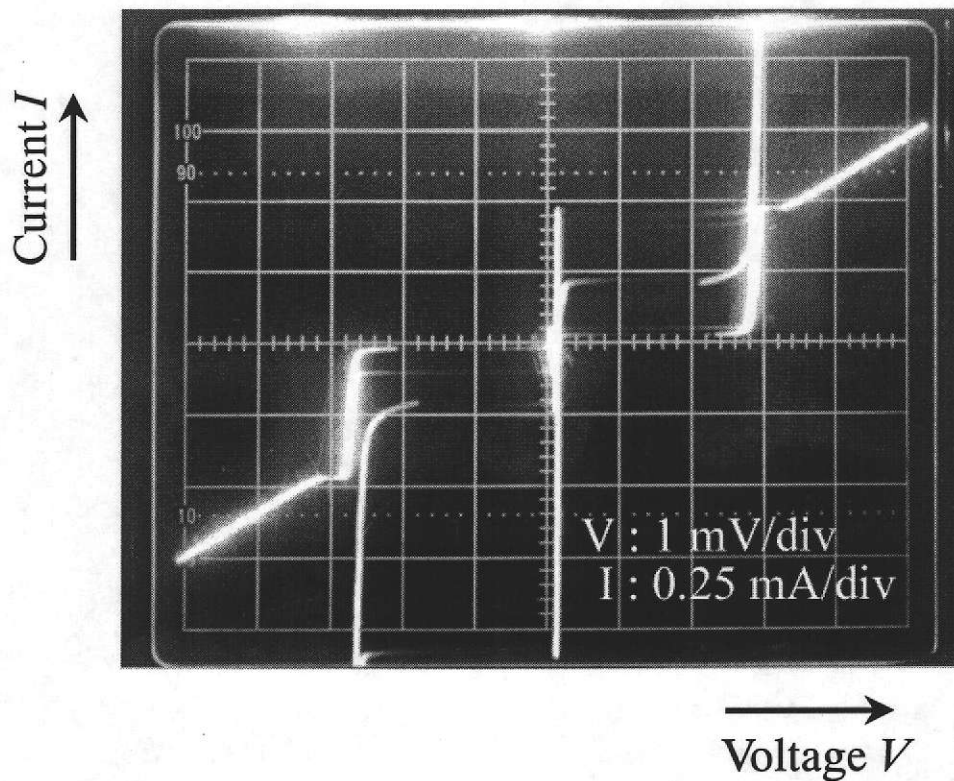
Figure 6.6 DC I-V characteristic of the 110-180 GHz SIS mixer. The horizontal scale is 1 mV per division, and the vertical scale is 0.25 mA per division. The current density measured from the I-V curve is 2.8 kA/cm^2.
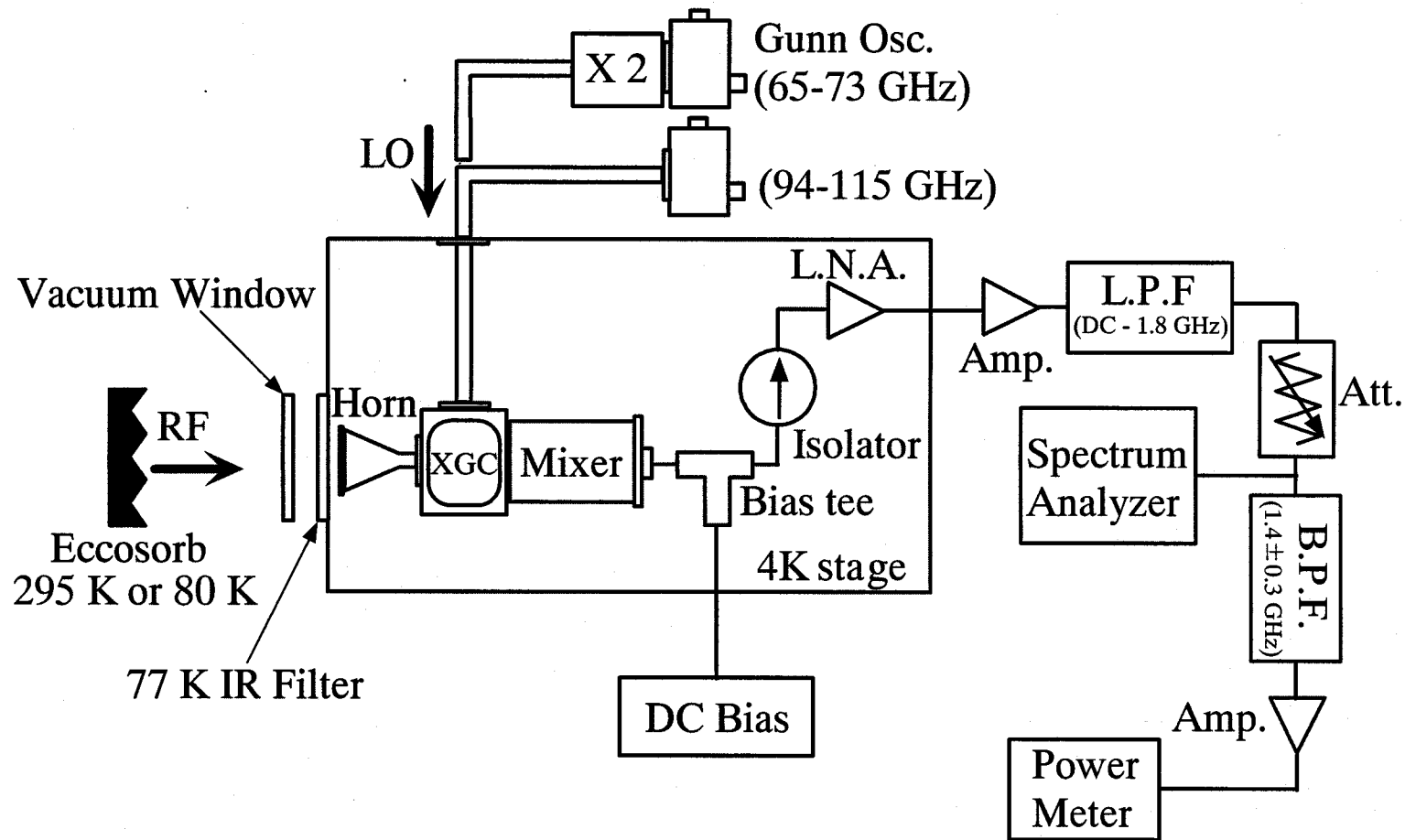
Figure 6.7 Schematic layout of the measurement set-up for 110-180 GHz band SIS mixer.
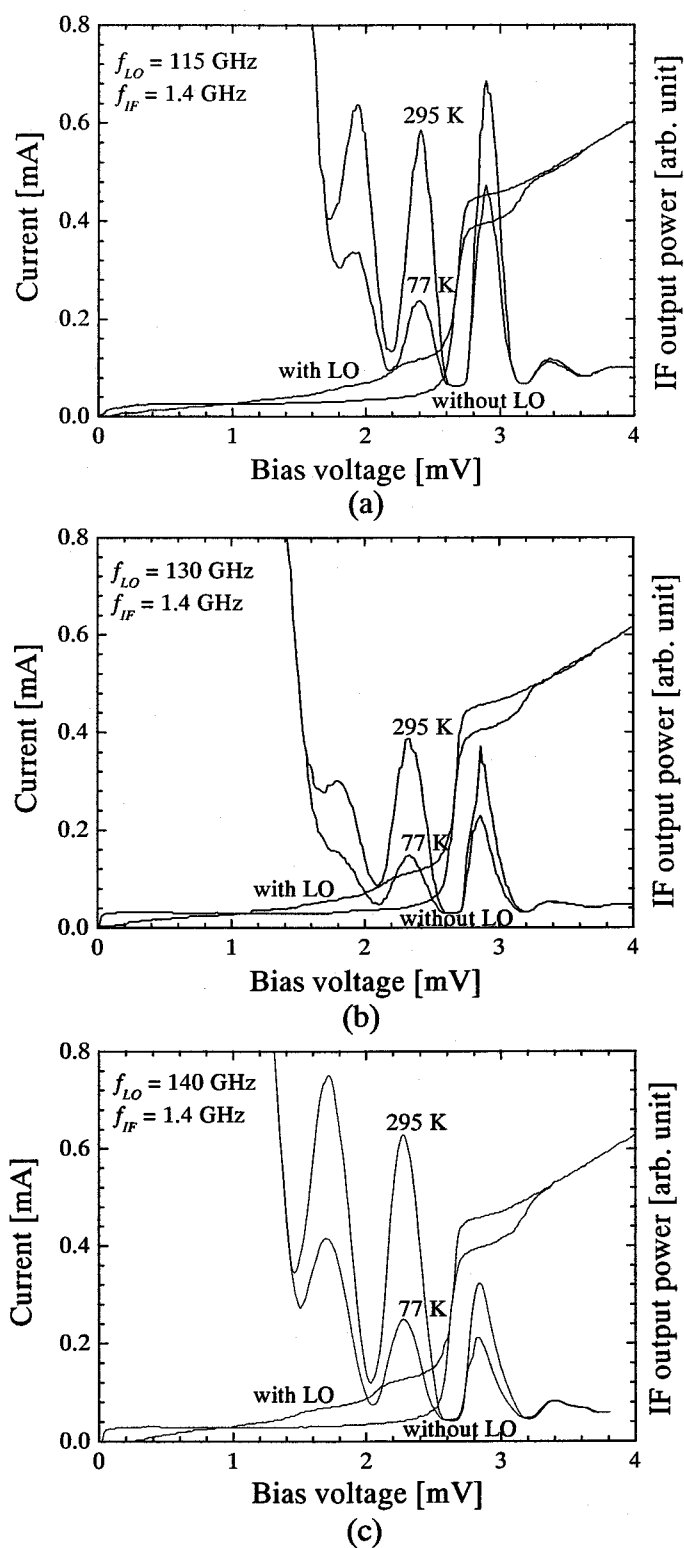
Fig. 6.8 DC I-V characteristics of the inhomogeneous distributed junction array with and without LO at (a) 110 GHz, (b) 130 GHz, and (c) 140 GHz. Also shown is the receiver's IF output powers as a function of bias voltage, for both hot (295 K) and cold (77 K) input loads.
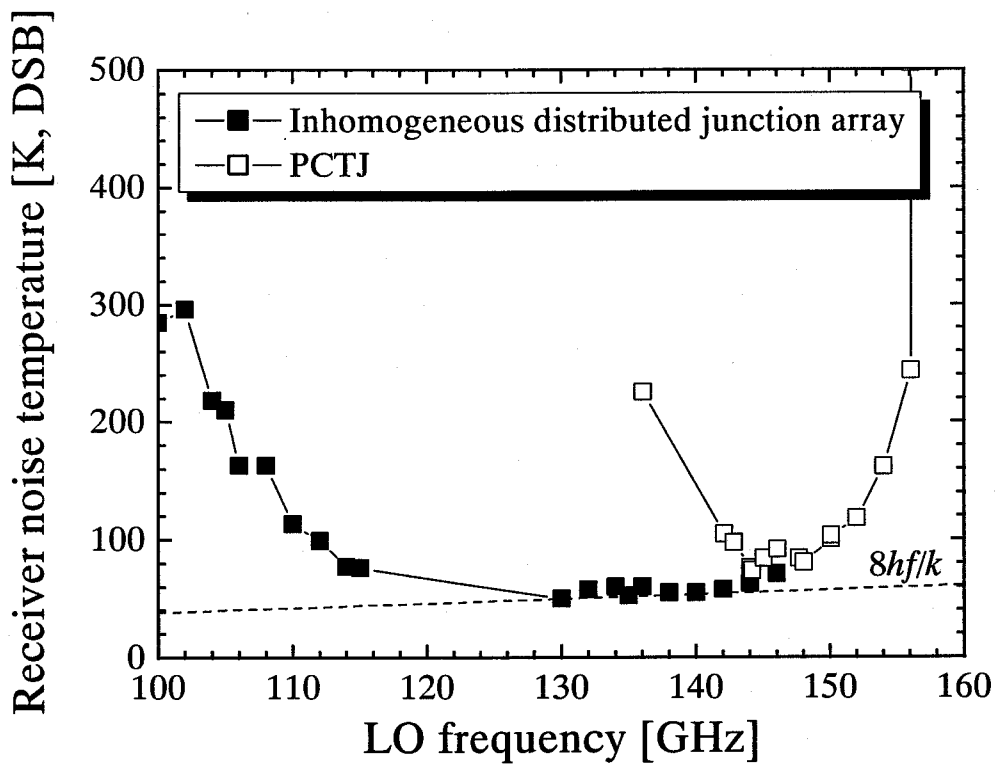
Figure 6.9 DSB receiver noise temperature as a function of frequency for the SIS mixers with the inhomogeneous distributed junction array and two-junction tuning circuit. In the experiment of the inhomogeneous distributed junction array, no data was obtained above 146 GHz because no LO source was available.
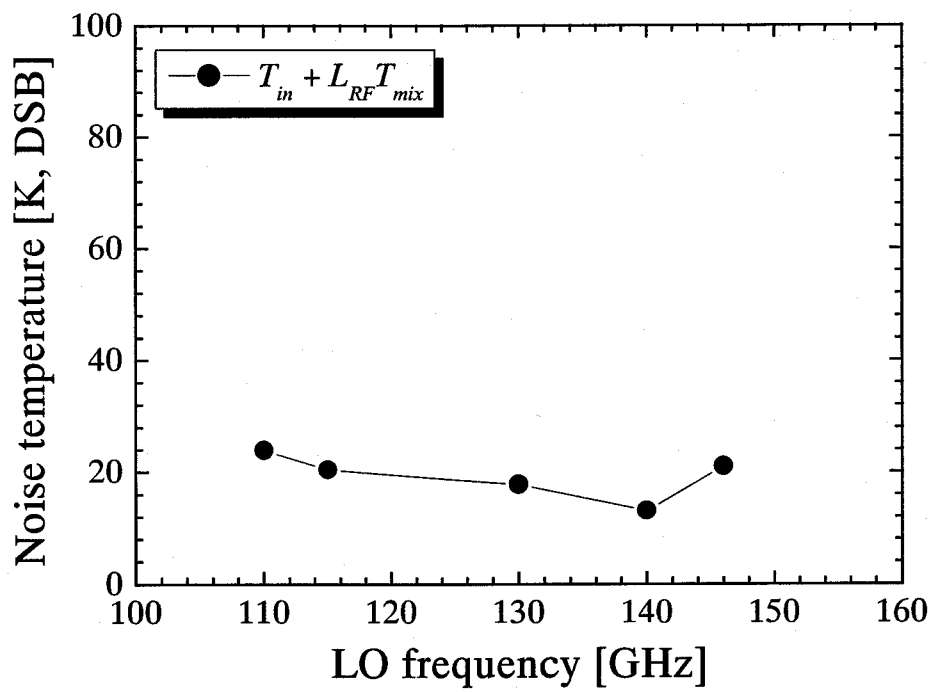
Figure 6.10 Noise temperature in front of the IF network as a function of frequency.
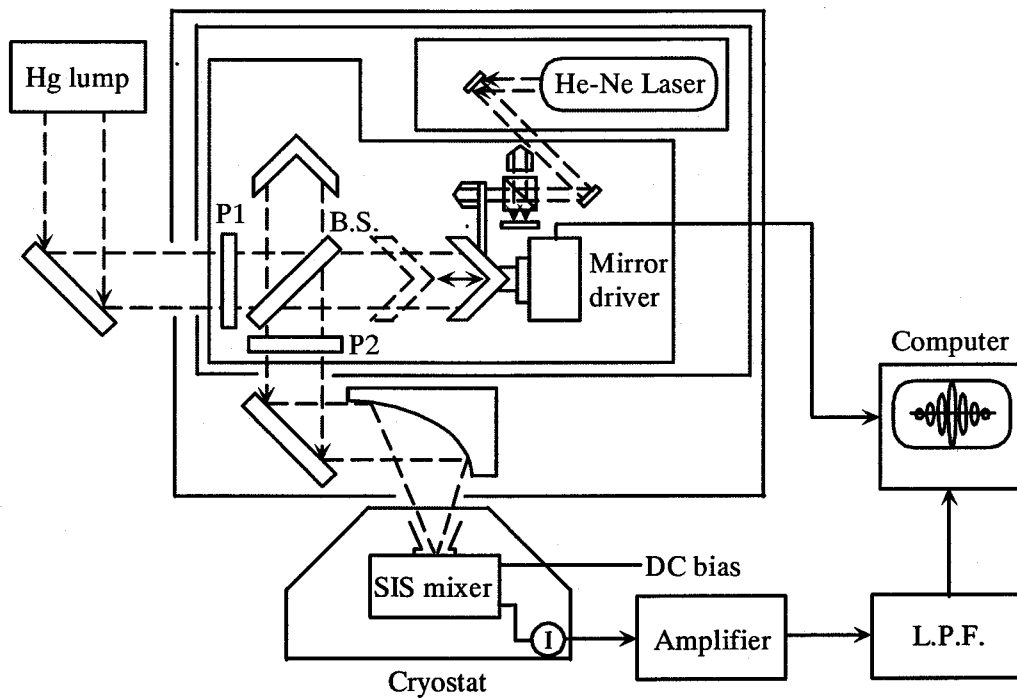
Figure 6.11 Schematic diagram of the FTS. The interferometer is a standard Martin-Puplett type with a polarizing beam splitter (B.S.), two polarizers (P1, P2), and two corner reflectors. One of the corner reflectors is driven continuously by a magnetic coil, which is controlled using the He-Ne laser fringes of a sub-interferometer.
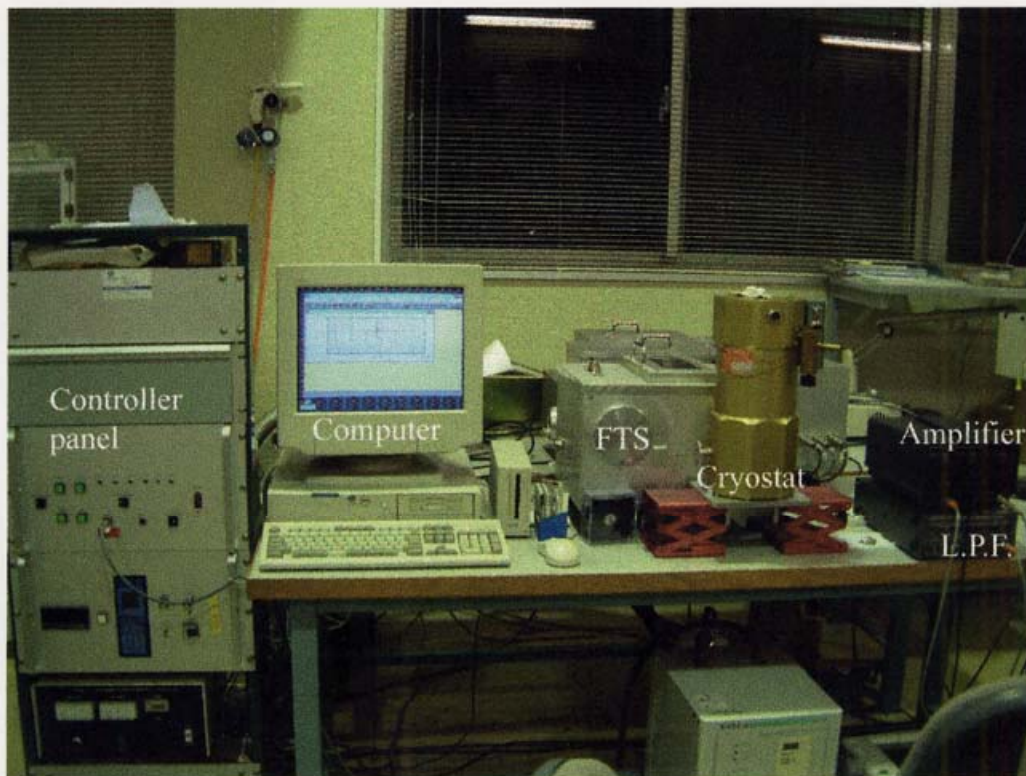
Figure 6.12 Photograph of the FTS system.
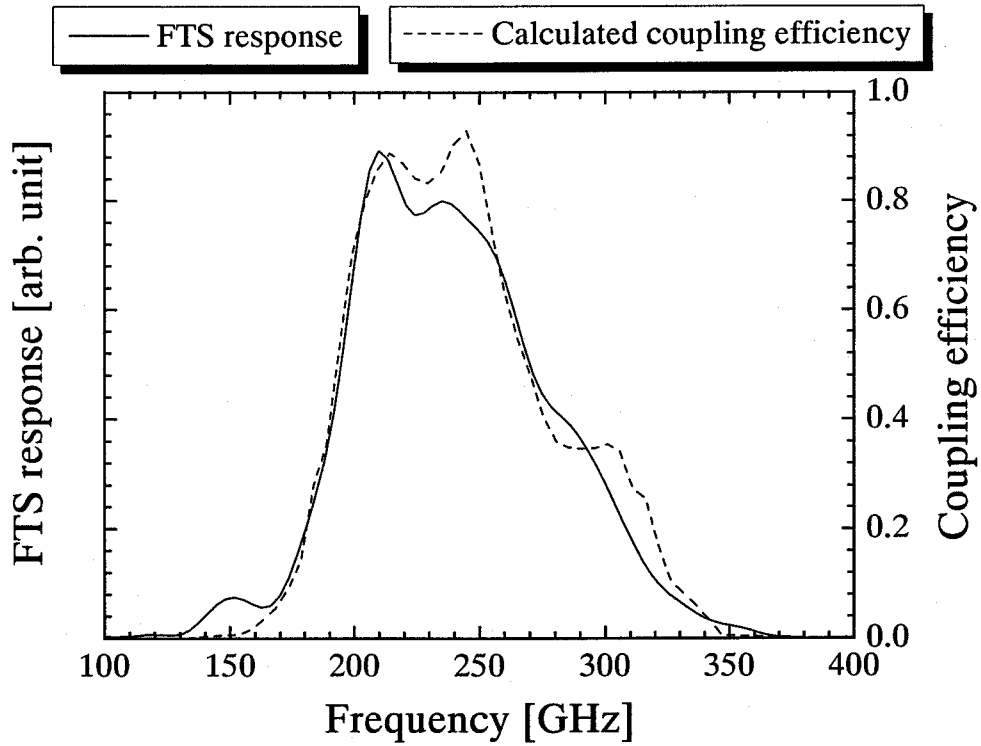
Figure 6.13 FTS response of the receiver. Also shown is calculated input coupling efficiency using actual parameters obtained in DC measurements.
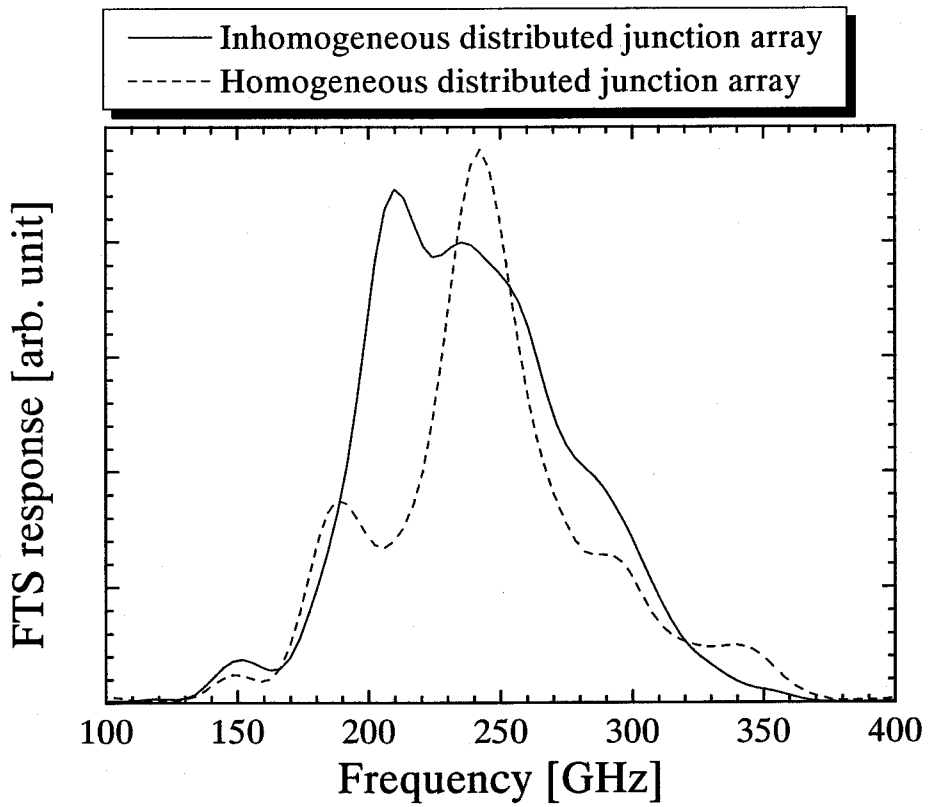
Figure 6.14 FTS responses of inhomogeneous and homogeneous distributed junction arrays as a function of frequency.
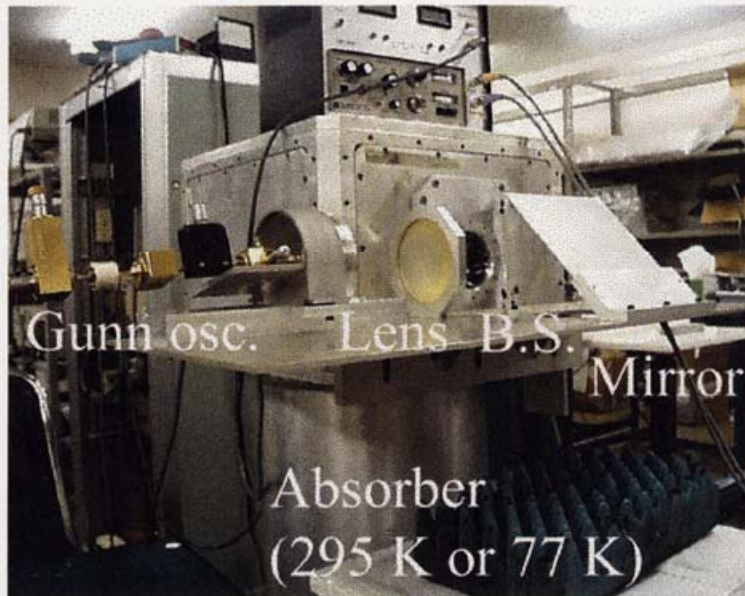
(a)
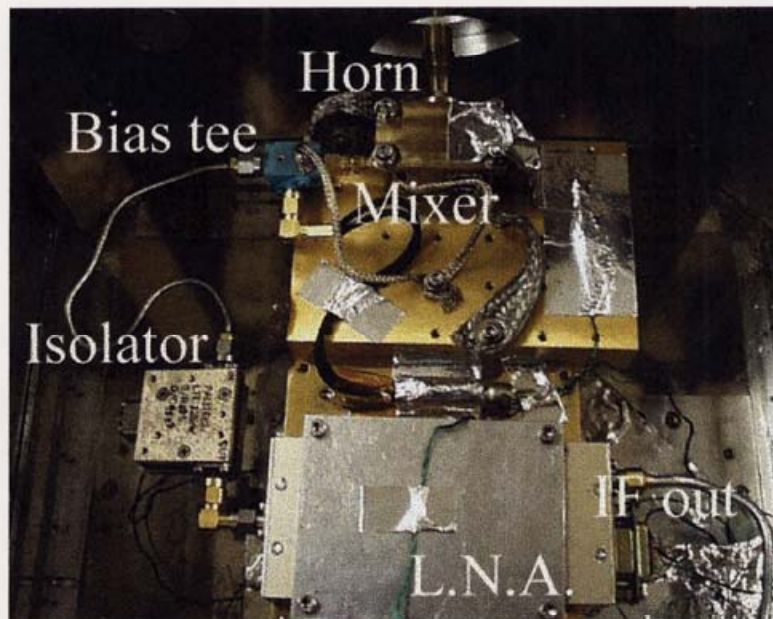
(b)

Figure 6.15 Photograph of the measurement system for the 190-300 GHz band SIS mixer. (a) LO injection scheme. (b) Inside of the 4-K refrigerator.
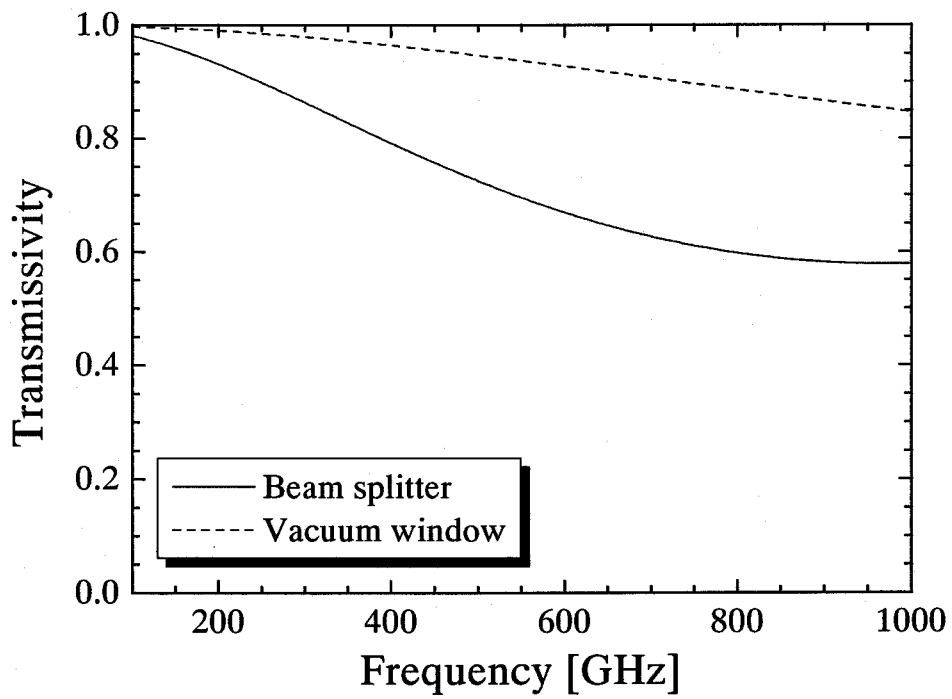
Figure 6.16 Calculated transmissivity of a beam splitter and a vacuum window. The beam splitter is a 50-μm thick Mylar film and the vacuum window is a 25-μm thick Mylar film.
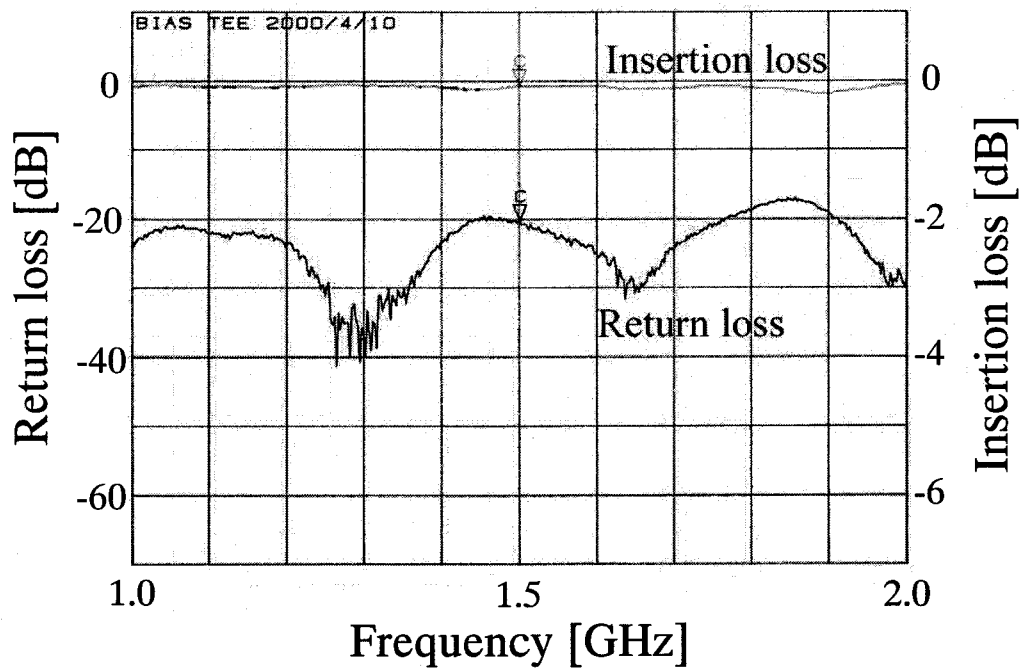
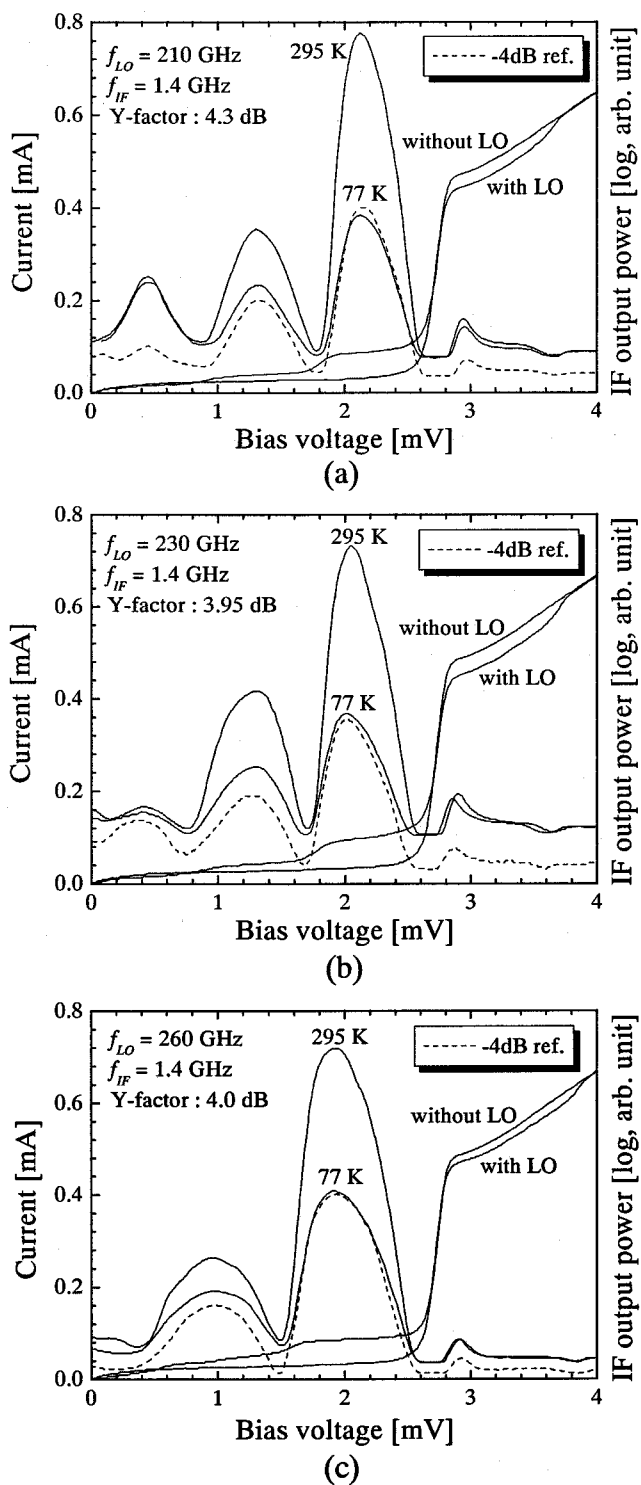Figure 6.17 Return loss and insertion loss of the IF circuit for 190-300 GHz band SIS mixer.
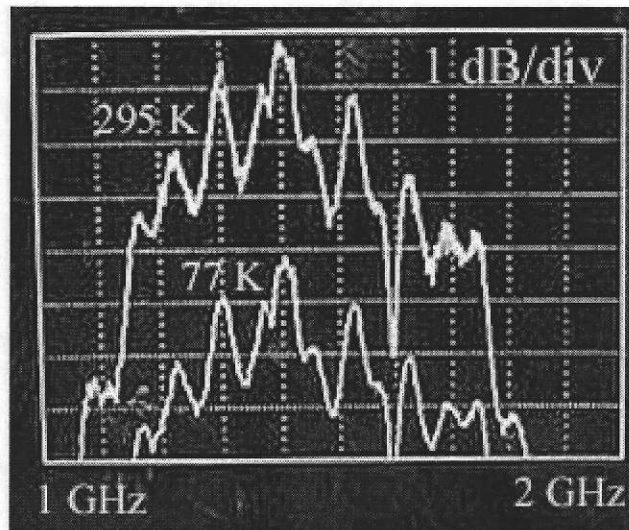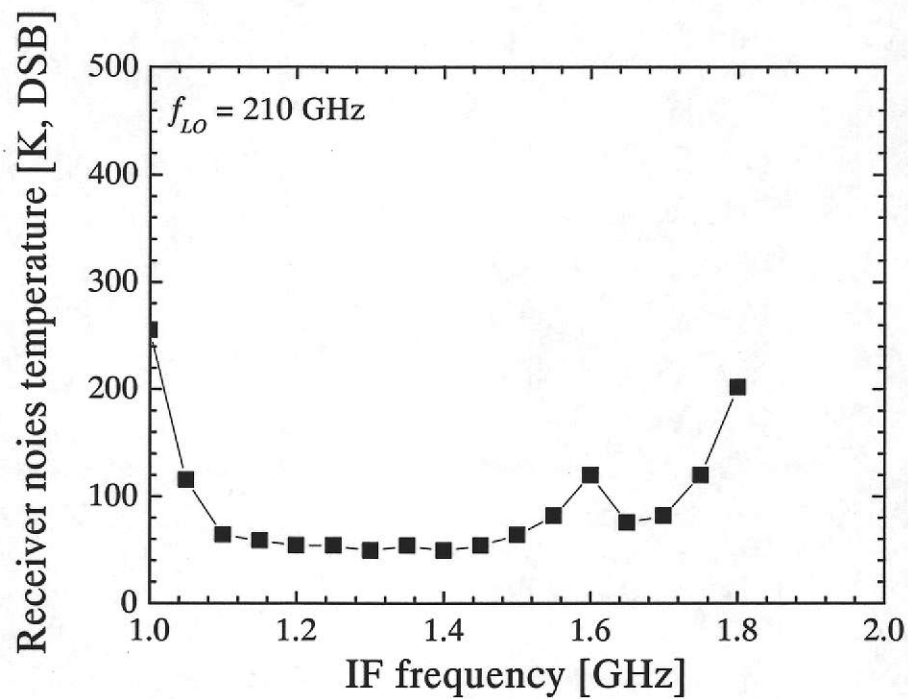
Figure 6.18 DC I-V characteristics of the inhomogeneous distributed junction array with and without LO at (a) 210 GHz, (b) 230 GHz, and (c) 260 GHz. Also shown is the receiver's IF output powers as a function of bias voltage, for both hot (295 K) and cold (77 K) input loads.

(a)

(b)

Figure 6.19 (a) Photograph of the output of the IF power as a function of IF frequency for hot- and cold- input loads. The frequency range is from 1.0 GHz to 2.0 GHz. (b) The IF frequency dependence of the receiver noise temperature at LO frequency of 210 GHz.
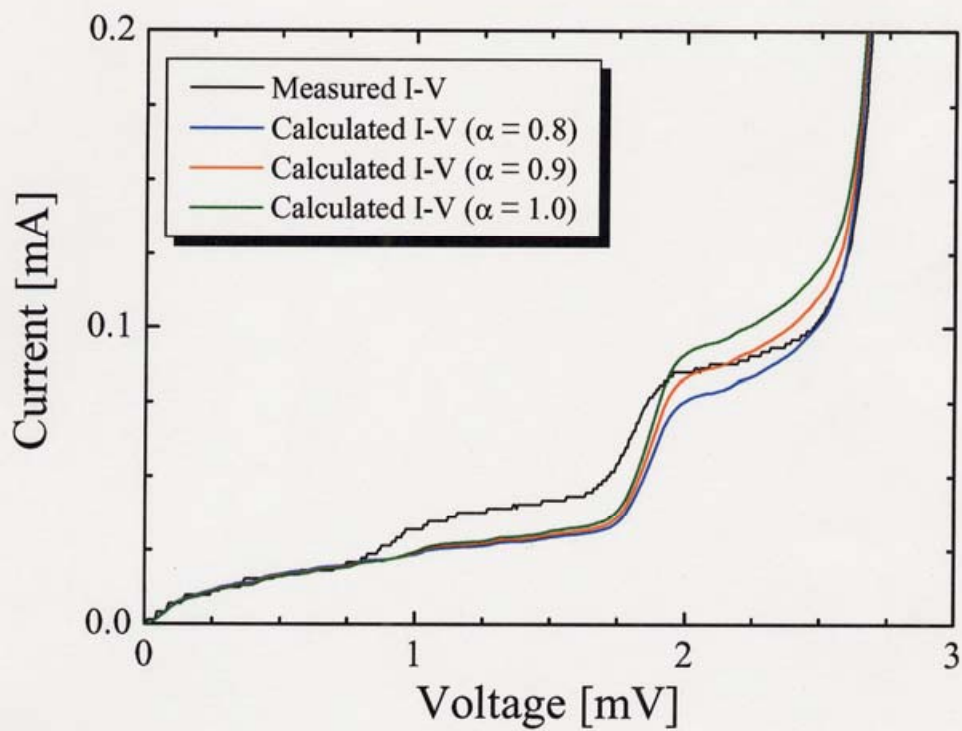
Figure 6.20 Comparison between the calculated and measured photon assisted tunneling step at 210 GHz. The height of the photon-assisted tunneling step in the case which set the value of α to 0.9 fits measured value most.
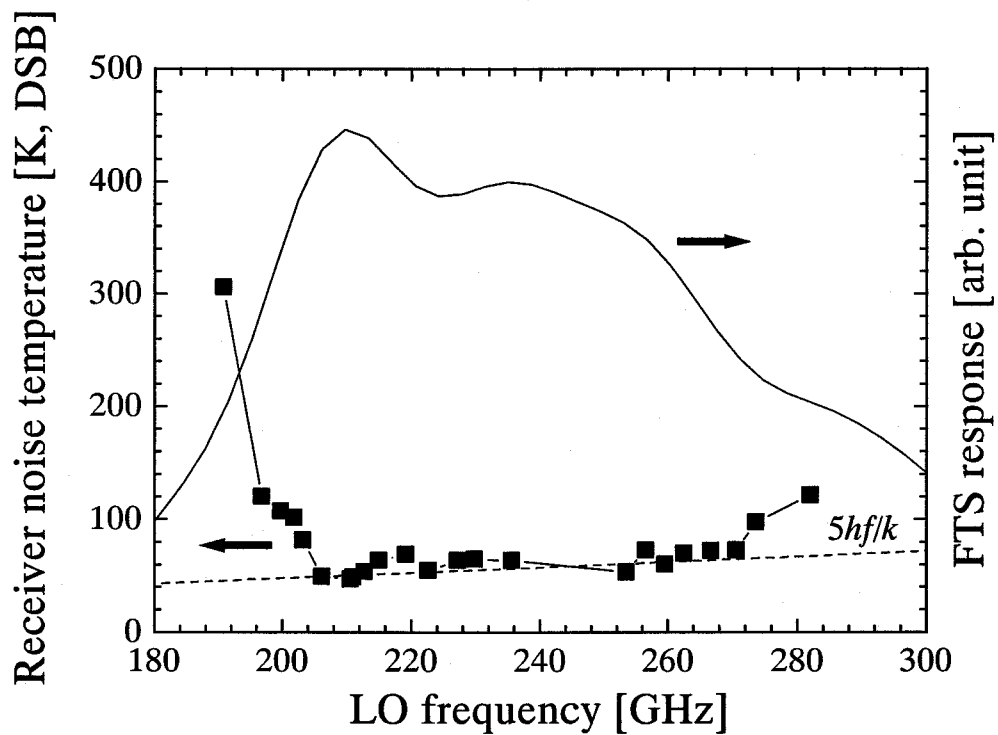
Figure 6.21 Receiver noise temperature and FTS response of the SIS mixer with the inhomogeneous distributed junction array using a corrugated feed horn with the output port of WR-4 waveguide as a function of frequency.
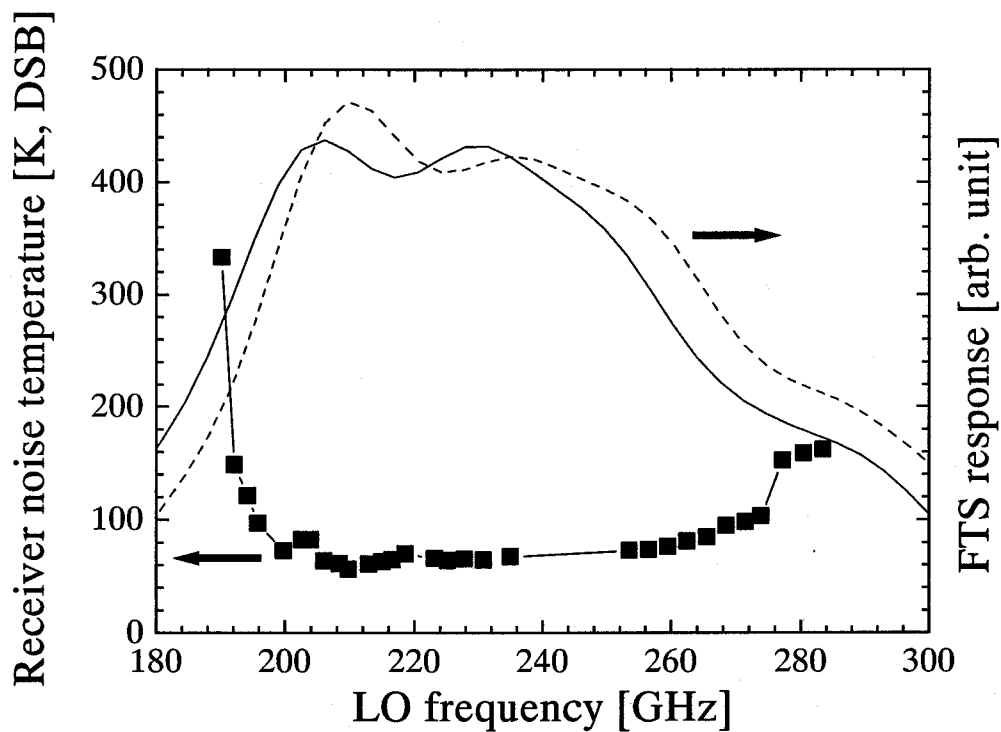
Figure 6.22 Variation of the receiver performance due to the offset of the position of the waveguide probe. When the probe was shifted 10 μm toward to the IF port, the receiver noise temperature and FTS response (solid lines) were obtained. For the comparison, the FTS response (dashed line) in Fig. 6.18 is also shown.
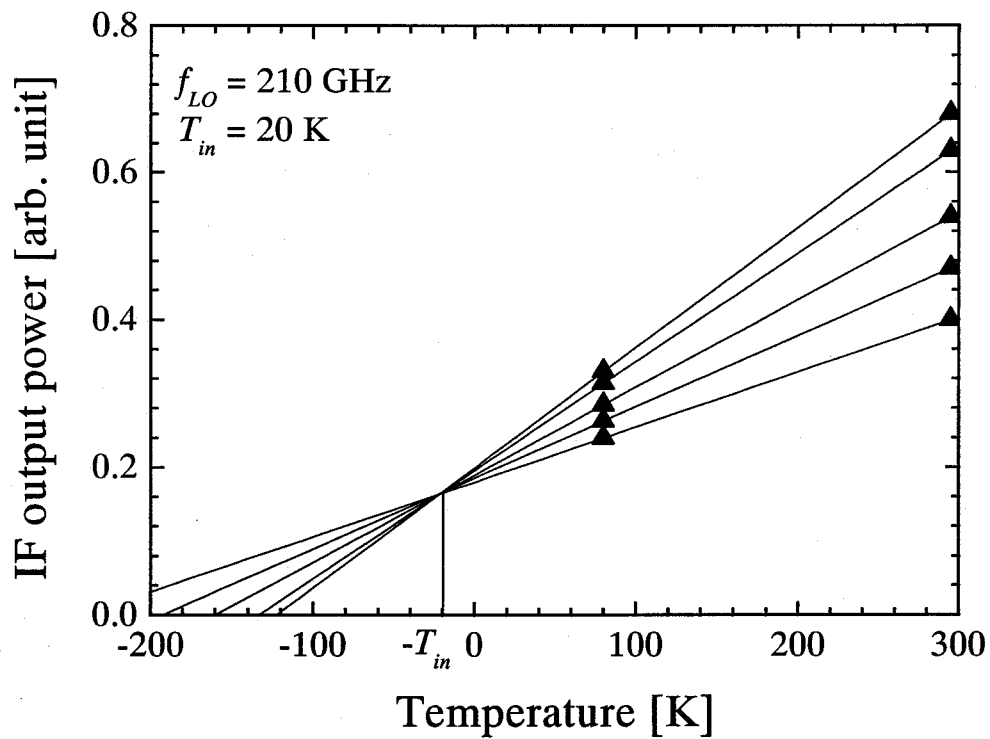
Figure 6.23 The IF output power at 210 GHz is plotted as a function of input load temperature for different values of LO power level.
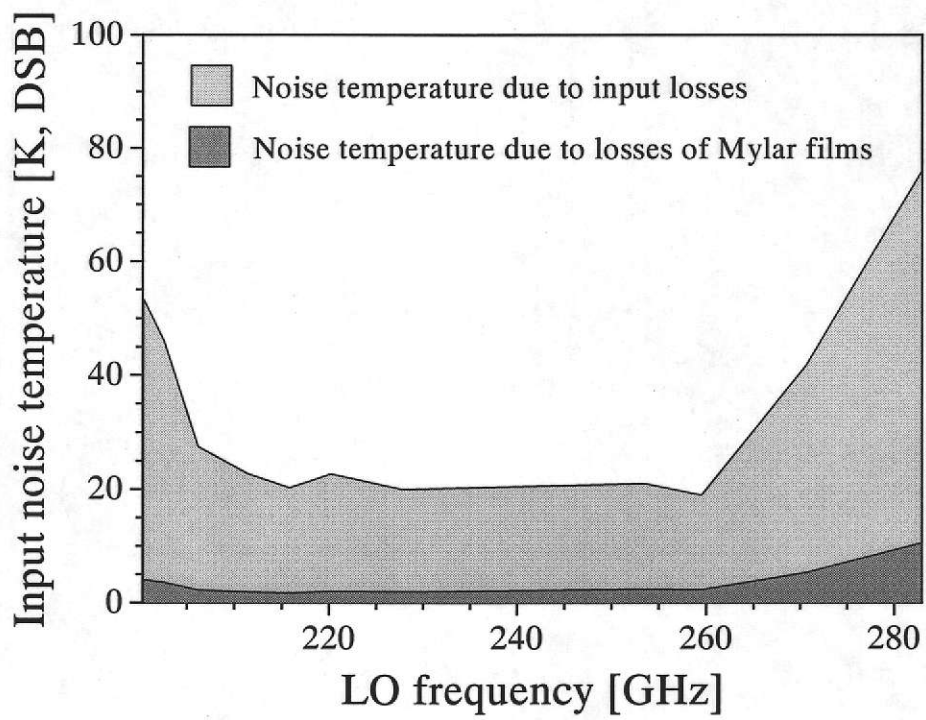
Figure 6.24 Noise temperature due to input losses as a function of frequency. The noise contribution by the Mylar films used as a beam splitter and a vacuum window is also shown.
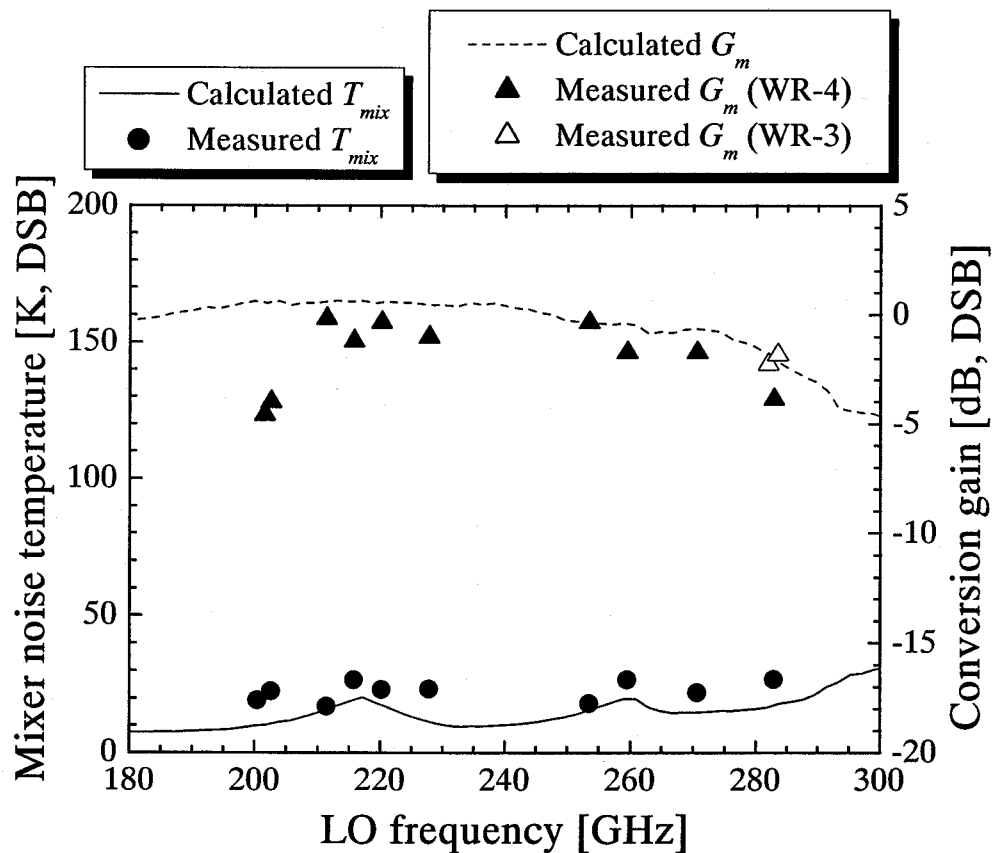
Figure 6.25 Mixer noise temperature, T_{mix}, and conversion gain, G_m, of the SIS mixer with the inhomogeneous distributed junction array measured using the WR-4 and WR-3 corrugated feed horns as a function of frequency. Comparison between the theoretical and experimental performance of the SIS mixer with the inhomogeneous distributed junction array is also shown.

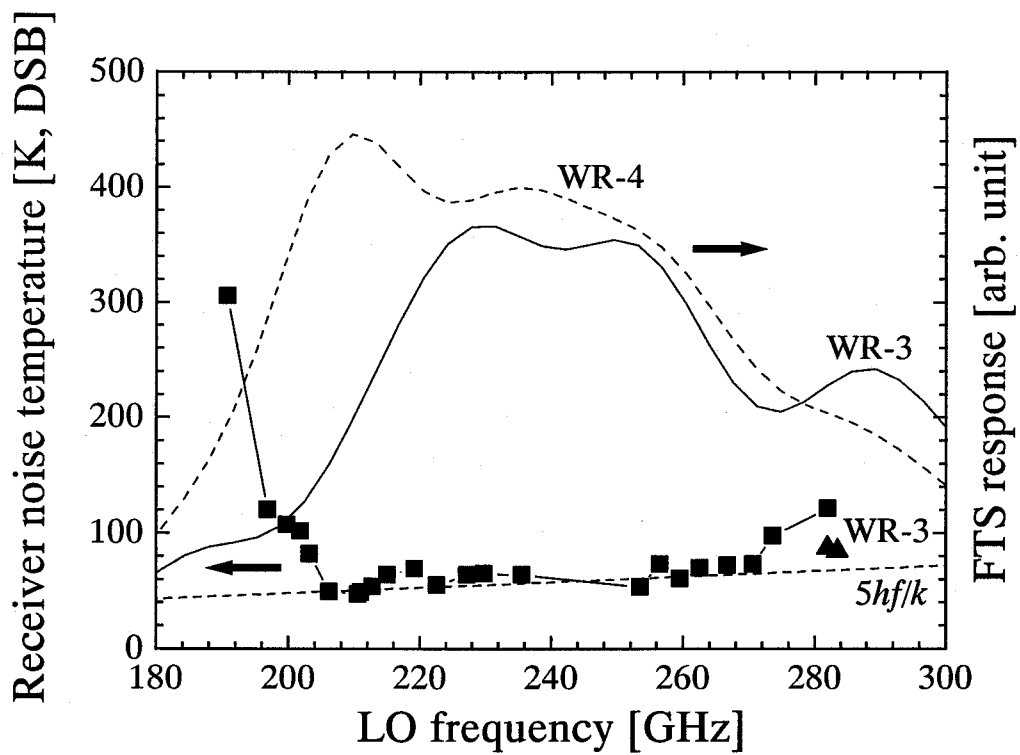Figure 6.26 Receiver noise temperature and FTS response of the SIS mixer with the inhomogeneous distributed junction array using a corrugated feed horn with the output port of WR-4 and WR-3 waveguides as a function of frequency.
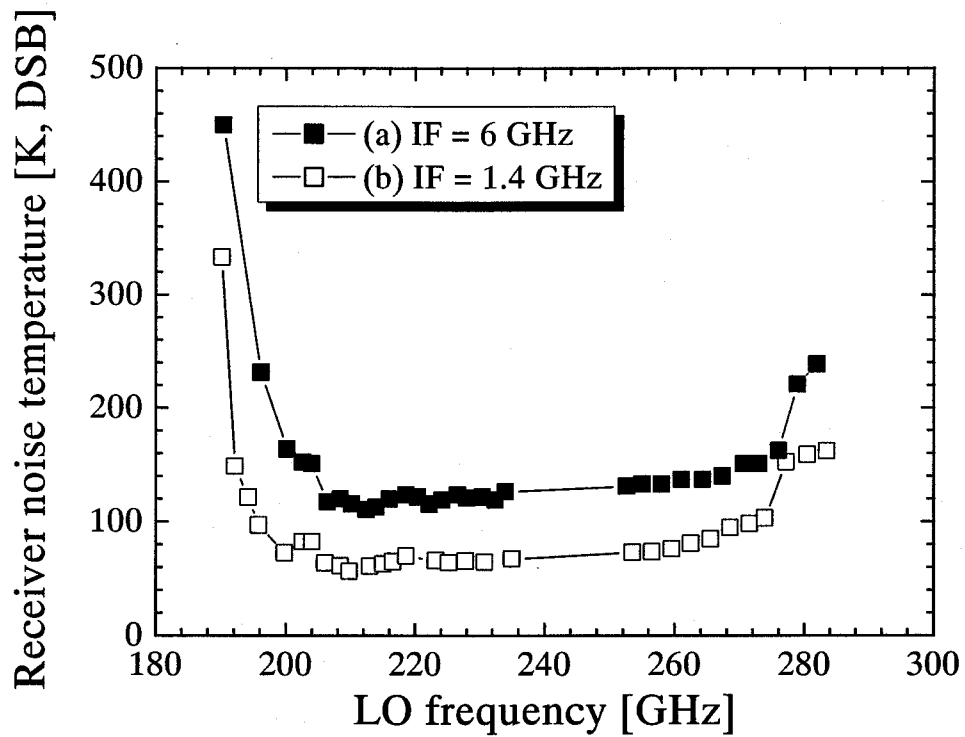
Figure 6.27 Receiver noise temperature as a function of LO frequency for two different IF amplifier. (a) 6-GHz center frequency, 2-GHz bandwidth. (b) 1.5-GHz center frequency, 0.5-GHz bandwidth.

Table 6.1 Optimized dimensions of junctions and spacings between pairs of adjacent junctions for an inhomogeneous distributed junction arrays in the frequency range from 110 GHz to 180 GHz.[a]

Array	$A^{(1)}$	$A^{(2)}$	$A^{(3)}$	$A^{(4)}$	$A^{(5)}$	$L^{(1)}$	$L^{(2)}$	$L^{(3)}$	$L^{(4)}$
Inhomogeneous	1.5	2.6	3.3	3.3	1.6	135	108	108	135

a) A values are the dimensions of junctions in μm^2 and L values are the spacings between the respective pairs of adjacent junctions in μm.

Chapter VII

Summary

This work aimed to achieve broadband SIS receivers in the millimeter and submillimeter wavelengths. In general bandwidth of SIS receivers is strongly dependent on the junction critical current density, as SIS receivers with broader bandwidth require a higher critical current density. Since a high critical current density has various disadvantages such as large sub-gap leakage current and a reduction of the yield of junctions in fabrication, it is desirable to develop SIS receivers that are capable of broadband operation with as low critical current density as possible. An SIS receiver with homogeneous distributed junction array, which consists of a number of junctions with identical dimensions homogeneously distributed on a superconducting microstrip, can be lowered the required critical current density to achieve a reasonable bandwidth in contrast with the conventional single-junction SIS receivers. However, it has been found that a large increase in receiver noise temperature at certain frequencies occurs in the SIS receiver. A new type of SIS receiver with an inhomogeneous distributed junction array was proposed in this work to overcome the problem. This mixer uses different dimensions for junctions and spacings between adjacent junctions. In the preceding chapters detailed descriptions and analyses were devoted to the development of waveguide-type SIS receivers with inhomogeneous distributed junction arrays in the millimeter wavelengths. The main results are summarized in this chapter. The future applications of the distributed junction arrays are also discussed.

Theoretical analyses

- Dimensions of junctions and spacings between the adjacent junctions were determined so as to minimize the reflection coefficient at the input port assuming simplified equivalent circuits of inhomogeneous distributed junction arrays.

- Extended quantum theory of mixing for the inhomogeneous distributed junction arrays were established based on quasi five-frequency approximation and the mixing properties were analyzed.

- The optimal range of input impedance of SIS mixers with distributed junction arrays have been concluded as 1.0~2.5 to the normalized resistance and -1.0~0 to the normalized reactance. The optimal range was well in agreement with that of single-junction SIS mixers.

- The calculation of mixing properties predicted that junction critical current density required to achieve a reasonable bandwidth could be lowered in distributed junction arrays in contrast with that in conventional single-junction SIS mixers.

- It was demonstrated that amplitude of noise increase observed at certain frequencies in the homogeneous distributed junction arrays was considerably reduced in the inhomogeneous distributed junction arrays. The number of junctions can be reduced in the inhomogeneous distributed junction arrays than that of homogeneous distributed junction arrays in order to achieve nearly the same mixing properties.

- The inhomogeneous distributed junction arrays with the critical current density of 2.0 kA/cm^2 and 3.0 kA/cm^2 were designed using Nb/AlOx/Nb tunnel junctions in 110-180 GHz and 190-300 GHz bands, respectively. The theoretically predicted mixer noise temperature was less than $3hf/k$ in the bands.

Design of a waveguide-type mixer chip and junction fabrication

- A waveguide-type SIS mixers with inhomogeneous distributed junction arrays is basically a scaled-up version of that using at NRO. The most characteristic feature of mixer-chip layout is to include a waveguide probe, which can provide excellent power coupling via a waveguide-to-microstrip transition. The RF and LO signals are transmitted from the input waveguide to a 75-Ω microstrip, and then coupled to the inhomogeneous distributed junction array via three stages of 1/4-wavelength impedance transformer.

- Two-stages of 1/4-wavelength impedance transformer were incorporated in an IF circuit of 110-180 GHz band SIS mixer to achieve the high conversion efficiency.

- Nb/AlOx/Nb tunnel junctions were fabricated on a crystalline-quartz wafer. The fabrication process was basically SNEP (Selective Niobium Etching Process), incorporating anodization to suppress the leakage current around junction. The DC I-V curves with the small sub-gap leakage current and strong nonlinearity were obtained in the junctions for 110-180 GHz and 190-300 GHz band SIS mixers.

Mixing experiments

- In the 110-180 GHz band SIS mixer, the DSB receiver noise temperature of 8hf/k was obtained in the frequency range from 130 to 146 GHz and the minimum noise temperature was 55 K at 140 GHz. It was found that the receiver noise temperature would be reduced by using the IF amplifier with smaller noise temperature and the IF circuit with lower insertion loss. In the frequencies above 146 GHz the receiver noise temperature could not measure because no LO source was available.

- The tuning bandwidth of the 190-300 GHz band SIS mixer were evaluated by using

a Fourier Transform Spectrometer (FTS). The result of FTS measurement of the fabricated inhomogeneous distributed junction array was in good agreement with the calculated coupling efficiency.

- It was found that the bandwidth characteristic in the inhomogeneous distributed junction array was less dependent on frequency compared with that in the homogeneous distributed junction array, as predicted in the theoretical analyses.

- The required LO power to pump the 190-300 GHz band SIS mixer was estimated by comparing the height of first-photon step in the calculated and measured I-V curves. The required LO power to pump the 190-300 GHz band SIS mixer was estimated as 49 nW, which is substantially same for the conventional SIS mixers.

- In the 190-300 GHz band SIS mixer, the DSB receiver noise temperature of $5hf/k$ was obtained in the frequency range from 202 to 284 GHz and the minimum noise temperature of 47 K was obtained at 210 GHz. The experimental results were analyzed quantitatively by breaking down the receiver noise temperature into the contributions due to the input noise, mixer noise, and IF network. It was found that the bandwidth of the inhomogeneous distributed junction array has been limited to that of the RF input circuit. From the comparison between the calculated and measured mixer noise temperature, it can be concluded that the mixer itself has the bandwidth of designed region, which is from 190 to 300 GHz. These facts indicate that SIS mixers with inhomogeneous distributed junction arrays are capable of broadband operation in spite of low critical current density.

Future applications

Millimeter- and submillimeter-wave SIS mixers with broadband characteristic are

needed in radio-astronomy projects such as the Atacama Large Millimeter Array (ALMA) and the Far Infrared and Submillimeter Space Telescope (FIRST) [1, 2]. For example, the ALMA covers the frequency range from 30 to 950 GHz in ten bands and the bandwidth of each band is mostly equivalent to the full band of a waveguide. It was described in Chapter III that the critical current density of SIS junctions must increase for broadband operation of SIS mixers and the further increase of current density is required in order to make SIS mixers operated in higher frequency. The highest frequency band (band 10) in the ALMA is from 787 to 950 GHz. For single-junction SIS mixers, the critical current density of 18 kA/cm^2, which corresponds to $\omega R_n C_j$ of 5.3 at 870 GHz, is required to cover this band. Although in such practical applications as ALMA, high yields in the fabrication of good-quality junctions are especially desired, it is actually quite hard to make high-quality junctions with a critical current density $> 10 \, \text{kA/cm}^2$.

If the SIS mixers with distributed junction arrays are adopted, the bandwidth of ALMA band 10 can easily be achieved keeping the critical current density of junctions less than 10 kA/cm^2, in which a quality ratio R_{sub}/R_n of SIS junction more than 10 can be satisfied. Figure 7.1 shows the receiver noise temperature in the frequency range from 700 to 1000 GHz of SIS mixers with distributed junction arrays with five junctions and single junction as an example. In both mixers the critical current density was assumed to be 8 kA/cm^2. Although ALMA band 10 is beyond the gap frequency of Nb (700 GHz), the calculation was performed without including losses due to the surface resistance of wiring layer, assuming that superconducting materials such as NbN or NbTiN with higher gap energy than that of Nb are available as the wiring layer. The inhomogeneous distributed junction array was designed according to the method

described in Chapter IV. The following two restrictions were imposed on the inhomogeneous distributed junction array. At first, a minimum dimension of junctions should be larger than 0.8 μm^2, which is minimum size produced by conventional optical lithography technique. Secondly, the dimensions of junctions must be determined so that the equivalent normal-state resistance of the inhomogeneous distributed junction array is greater than 3 Ω, which becomes easy to achieve a good impedance match with the source. The dimensions of junctions and spacing between adjacent junctions of the inhomogeneous distributed junction array are listed in Table 7.1. As shown in Fig. 7.1, the broadband performance is achieved in the SIS mixer with the inhomogeneous distributed junction array and the SSB receiver noise temperature is less than 170 K (~ 4*hf*/*k* at 910 GHz) in the frequency range from 700 to 1000 GHz, which covers the ALMA band 10 enough. Even if there are the above-mentioned restraint conditions, inhomogeneous distributed junction arrays will operate without large noise ripples enough to 1 THz. Above 1 THz, it is difficult to design inhomogeneous distributed junction arrays because the input impedance separates from the optimal range ($1 \le r \le 2.5$ and $-1 \le x \le 0$), unless the minimum dimensions of junctions becomes smaller than 0.8 μm^2, which can be achieved by a technique using electron-beam lithography, or the number of junctions is increased.

Moreover, the broadband performance of inhomogeneous distributed junction arrays is useful as superconducting direct detectors. The inhomogeneous distributed junction arrays as submillimeter-wave focal plane arrays based on the direct detectors have been investigated by the group of Matsuo *et al.* for the Atacama Submillimeter Telescope Experiment (ASTE) [3-5].

Finally, results of this work are plotted in Fig. 7.2 together with results of some of broadband SIS receivers that have been developed recently. This work successfully demonstrated the broadband performance of SIS mixers with inhomogeneous distributed junction arrays.

References

[1] http://www.alma.nrao.edu/

[2] http://Saturn.sron.nl/hifi/

[3] H. Matsuo, M. Takeda, T. Noguchi, S. Ariyoshi, and H. Akahori, "Development of submillimeter-wave camera for Atacama Submillimeter Telescope Experiment", *Advanced Technology MMW, Radio and Terahertz Telescopes, Proc. SPIE*, **4015**, 228 (2000).

[4] H. Matsuo, S. Ariyoshi, H. Akahori, M. Takeda, and T. Noguchi, "Development of submillimeter-wave camera for Atacama Submillimeter Telescope Experiment", *IEEE Trans. Appl. Superconductivity*, 11, 688 (2001).

[5] S. Ariyoshi, H. Matsuo, M. Takeda, and T. Noguchi, "Design of submillimeter-wave camera with superconducting direct detectors", *Proc. 12th Int. Symp. Space Terahertz Technology*, 183 (2001).
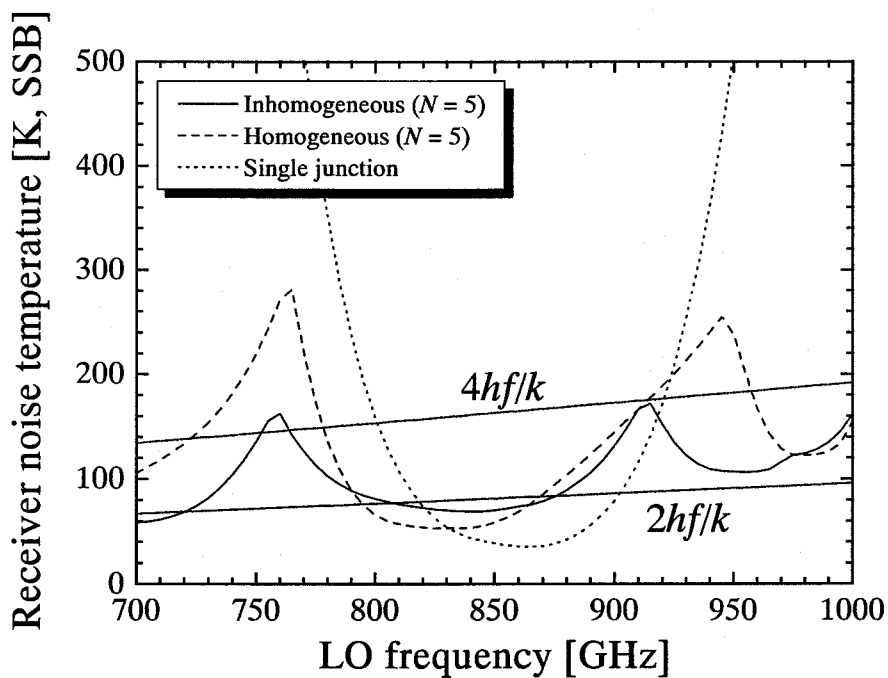
Figure 7.1 Calculated receiver noise temperature of SIS mixers with inhomogeneous (solid line), homogeneous (dashed line) distributed junction arrays, and single junction (dotted line) as a function of frequency of LO frequency. In every case, critical current density is assumed to be 8 kA/cm^2.
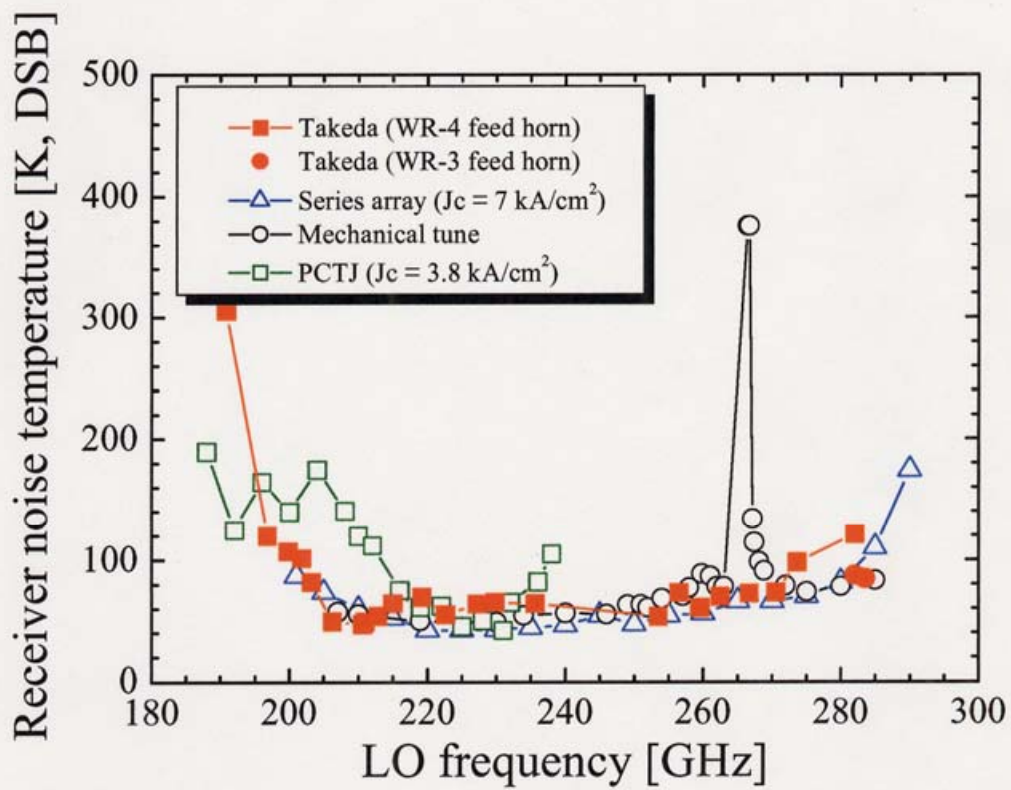
Figure 7.2 Results of this work and some of broadband SIS receivers recently developed.

Table 7.1 Dimensions of junctions and spacings between all pairs of adjacent junctions.[a]

Array	$A^{(1)}$	$A^{(2)}$	$A^{(3)}$	$A^{(4)}$	$A^{(5)}$	$L^{(1)}$	$L^{(2)}$	$L^{(3)}$	$L^{(4)}$
Inhomogeneous	0.8	2.0	1.5	2.0	1.0	6.2	6.2	7.3	7.3
Homogeneous	0.8	0.8	0.8	0.8	0.8	12.5	12.5	12.5	12.5

a) A values are the dimensions of junctions in μm^2 and L values are the spacings between the respective pairs of adjacent junctions in μm.

Appendix A.   Matrix characterization of networks

A.1 Chain matrix

An electrical network is an interconnection of electrical circuit elements according to some scheme. Associated with the network are terminals. When a voltage is applied across two terminals so that the current entering one terminal is equal to the current leaving the other terminal, the pair of terminals is called a port.

When the transfer property of a network is of interest, such as in a cascade connection, the chain matrix $[C]$ is often considered. In most cases consider the $(l+m)$-port network in Fig. A.1 where l and m are the number of input ports and output ports, respectively. Then the chain matrix is given as

$$\begin{bmatrix} V_1 \\ I_1 \end{bmatrix} = \begin{bmatrix} C_{11} & C_{12} \\ C_{21} & C_{22} \end{bmatrix} \begin{bmatrix} V_2 \\ -I_2 \end{bmatrix} \tag{A.1}$$

where C_{11}, C_{12}, C_{21}, and C_{22} are the $l\times m$ matrices. The chain matrix is often referred to as the ABCD matrix.

A.2 Series and parallel elements

The chain matrices representing series and shunt elements with impedances Z_s and Z_p shown in Figs. A.2a and b are given respectively by

$$[C] = \begin{bmatrix} 1 & Z_s \\ 0 & 1 \end{bmatrix} \tag{A.2a}$$

$$[C] = \begin{bmatrix} 1 & 0 \\ Z_p^{-1} & 1 \end{bmatrix} \tag{A.2b}$$

A.3 Transmission line

For a transmission line of length l and characteristic impedance Z0, the voltages and currents at each port shown in Fig. A.3 are related by the equations

$$V_1 = V_2 \cosh(\gamma l) + I_2 Z_0 \sinh(\gamma l)$$
$$I_1 = V_2 Z_0^{-1} \sinh(\gamma l) + I_2 \cosh(\gamma l)$$

(A.3)

where $\gamma = \alpha + j\beta$. α is the transmission loss per unit length and β is the phase constant. If the line is lossless, that is, $\alpha = 0$, then $\gamma = j\beta$ and $\sinh(\gamma l) = j\sin(\beta l)$ and $\cosh(\gamma l) = \cos(\beta l)$. The chain matrix of the transmission line is given as

$$[C] = \begin{bmatrix} \cosh(\gamma l) & Z_0 \sinh(\gamma l) \\ Z_0^{-1} \sinh(\gamma l) & \cosh(\gamma l) \end{bmatrix}.$$

(A.4)

If the line is open-circuited at one end, the input impedance is given as

$$Z = Z_0 / \tan(\gamma l).$$

(A.5)

If the line is short-circuited at one end, the input impedance is given as

$$Z = Z_0 / \cot(\gamma l).$$

(A.6)

From (A.2) the chain matrices of a shunt open stub and of a shunt short stub are given respectively by

$$[C] = \begin{bmatrix} 1 & 0 \\ Z_0^{-1} \tan(\gamma l) & 1 \end{bmatrix}$$

(A.7a)

$$[C] = \begin{bmatrix} 1 & 0 \\ Z_0^{-1} \cot(\gamma l) & 1 \end{bmatrix}.$$

(A.7b)

Appendix B.   Noise temperature of a linear two-port

B.1 Noise temperature of an attenuator

A two-port commonly used in receivers is a passive attenuator. For example, a transmission line between an antenna and a receiver always has some losses and can be considered to be an attenuator.

Figure B.1 shows an attenuator having a resistive source and load, at a physical temperature T. Because the attenuator and its terminations are in thermal equilibrium, the noise delivered to the load by the combined attenuator and source is equal to the noise that the load delivers to the attenuator and source. This noise level, in terms of noise temperature, is T.

$$T = G_t T + T_{a0}$$

(B.1)

where T_{a0} is the noise generated in the attenuator that is delivered to the load and G_t is the transducer gain (less than unity) of the attenuator. This situation is eminently sensible, since there is no fundamental difference between a termination and the output port of a matched attenuator with its input terminated. By referring T_{a0} to the input, we find the attenuator noise temperature T_{atn} to be

$$T_{atn} = \frac{T_{a0}}{G_t} = T\left(\frac{1}{G_t} - 1\right) = T(L - 1)$$

(B.2)

where $L = 1/G_t$, the loss factor.

B.2 Noise temperature of a cascade of stages

A receiver can be considered as a series connection of linear tow-ports. Figure B.2 shows the receiver divided into separate tow-ports. The noise temperature of the

two-ports are T_1, T_2, ..., T_n and transducer gains, G_1, G_2, ..., G_n.

The output noise of the N-th stage, the last in the cascade, is

$$T_{out} = G_n T_n + G_n G_{n-1} T_{n-1} + G_n G_{n-1} G_{n-2} T_{n-2} + \cdots + T_1 \prod_{m=1}^{n} G_m \qquad (B.3)$$

Dividing by the gain of the entire cascade (the product of the gains of the individual stages) gives the following result for the noise temperature of the cascade T_{nc}:

$$T_{nc} = T_1 + \frac{T_2}{G_1} + \frac{T_3}{G_1 G_2} + \cdots + T_n \prod_{m=1}^{n-1} \frac{1}{G_m} \qquad (B.4)$$

An important implication of (B.4) is that, in a cascade stages, each having gain greater than unity, the noise of the first few stages dominates the overall noise temperature.

Appendix C.   Noises in SIS receivers

C.1 Mixer noise temperature and conversion gain

Receiver and mixer performance are determined from I-V curves and measurements of the IF output (P_{IF}) with hot and cold loads held at mixer input. The P_{IF} is calibrated in terms of the equivalent Rayleigh-Jeans temperature at the IF amplifier input. This calibration and also a determination of the IF amplifier added noise are calculated using the linear portions of the I-V and P_{IF} curves. Equivalent circuit of a SIS receiver without LO is shown in Fig. C.1. Tunneling of quasiparticles gives rise to shot noise. For a junction biased where the current is a linear function of the voltage, the shot noise power density increases as the followings.

$$P_{av} = \frac{1}{4}R_d < \delta i_s^{\,2} > = \frac{R_d}{4}(2eI_{DC}) = kT_{eq}$$
(C.1)

where for $R_d = 50\ \Omega = R_N$

$$T_{eq} = \frac{eR_d}{2k}I_{DC} = \frac{e}{2k}V_{DC} = 5.8[K/mV] \cdot V_{DC}$$
(C.2)

Accordingly, the linear portion of the P_{IF} curve must have a slope of 5.8 K per mV when referred to the IF amplifier input (Fig. C.2). Now, P_{IF} is described as the following.

$$P_{IF} = kG_{IF}B(T_{IF} + T_{eq}) = kG_{IF}B\left(T_{IF} + \frac{e}{2k}V_{DC}\right)$$
(C.3)

From the slope of P_{IF} and position of zero shot noise point, we obtain T_{IF}, and BG_{IF} as the following.

$$BG_{IF} = \frac{P_0}{kT_{IF}}$$
(C.4)

Knowing T_{IF} and $G_{IF}B$, we can deduce some relationships between the conversion gain

G_m and mixer noise temperature T_{mix}.

From hot- and cold-loads measurement, we have

$$T_{RX} = T_{mix} + T_{IF}/G_m \qquad (C.5)$$

$$P_{hot} = [(295 + T_{mix})G_m + T_{IF}]kG_{IF}B \qquad (C.6)$$

Now, substitute expression (C.4) into expression (C.5), then we obtain

$$P_{hot} - P_0 = \frac{295 + T_{mix}}{T_{IF}} \cdot P_0 G_m \qquad (C.7)$$

Solve expression (C.4) for G_m, and substitute it into expression (C.6), then we obtain

$$P_{hot} - P_0 = \frac{295 + T_{mix}}{T_{RX} - T_{mix}} P_0 \qquad (C.8)$$

Solve expression (C.7) for T_{mix}, we obtain

$$T_{mix} = T_{RX}\left(1 - \frac{P_{hot}}{P_0}\right) - 295\frac{P_0}{P_{hot}} \qquad (C.9)$$

Solve expression (C.5) for T_{mix}, and substitute it into expression (C.6), then we obtain

$$G_m = \frac{T_{IF}}{295 + T_{RX}} \cdot \frac{P_{hot}}{P_0} \qquad (C.10)$$

C.2 Input noise

In a presence of an input section noise temperature T_{in}, the entire receiver noise temperature T_{RX}' may be as the following using expression (C.5),

$$T_{RX}' = T_{in} + L_{in}T_{RX} \qquad (C.11)$$

where L_{in} is the input section loss.

The T_{in} can be estimated using the intersecting lines technique. This involves making receive IF output power measurements for each load power level. Varying LO power has the effect of varying the mixer conversion loss. The intersecting lines techniques relies on the fact that the SIS mixer output noise temperature is largely

independent of mixer gain for low local oscillator power. Fig. C.3 shows a standard diagram of a heterodyne receiver. The receiver consists of three blocks: the RF input section, the mixer, and the IF amplifier. Cascading these blocks, the total output power P_T from the receiver when a matched load at temperature T is placed at the receiver input is given by

$$P_T = \left[\frac{T + T_{in}}{L_{in}} G_m + T^{out} + T_{IF} \right] kBG_{IF} \tag{C.12}$$

where we define the equivalent output noise temperature of the mixer

$$T^{out} \equiv G_m T_{mix} \tag{C.13}$$

In functional form, expression (C.12) simply states that $P_T(T)$ is a straight line. Equation (C.13) could also be written $P_T = (T+T_R)kBG_{IF}/(L_{in}/G_m)$, so that $P_T = 0$ for $T = -T_{RX}'$, which is a restatement of the graphical Y-factor method of determining T_{RX}.

Let us now assume that Tout is independent of the LO power, P_{LO}, for low LO power levels. Then in expression (D.3) only L_C will depend upon P_{LO}, and so P_T is independent of P_{LO} for some negative input load temperature $T = -T_X = -T_{in}$. Therefore the assumption implies that we can read $T_{in} = T_X$ directly from the intersection point on a graph like Fig. C.4. This is the "intersecting lines technique." Contributions to P_T are sketched in Fig. C.4.
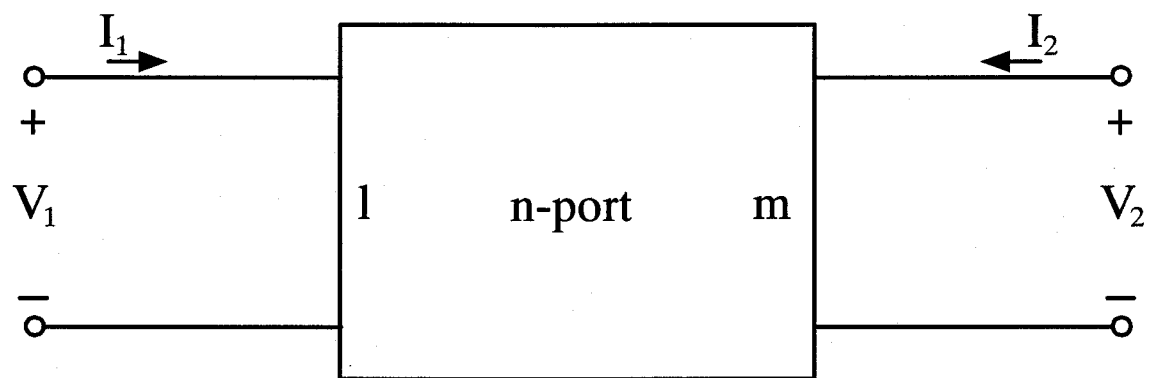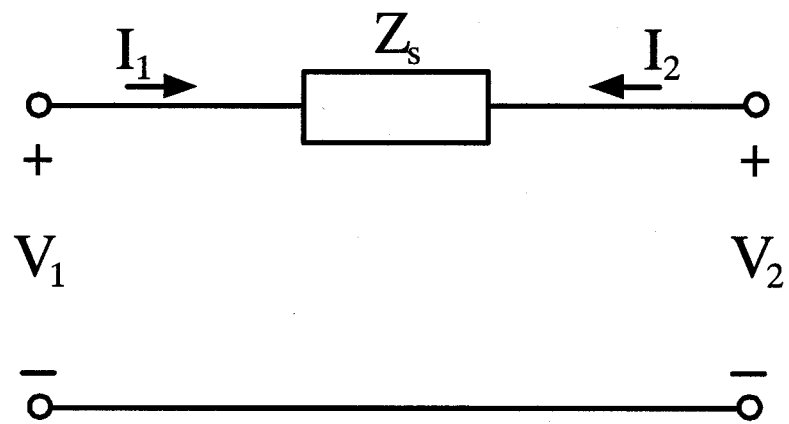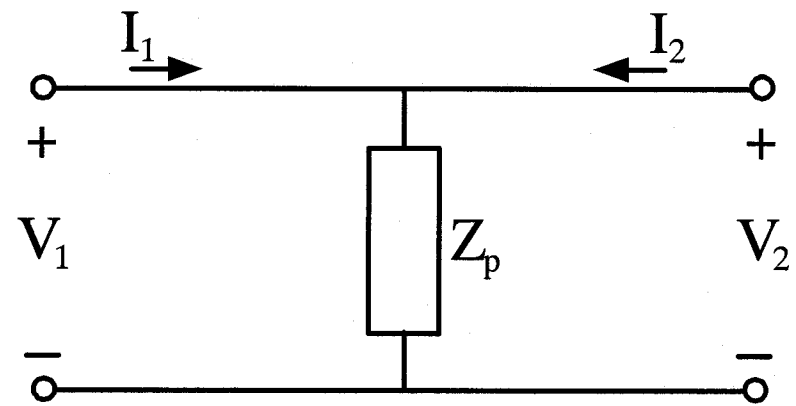
Figure A.1 The partitioned (*l+m*)-port network.

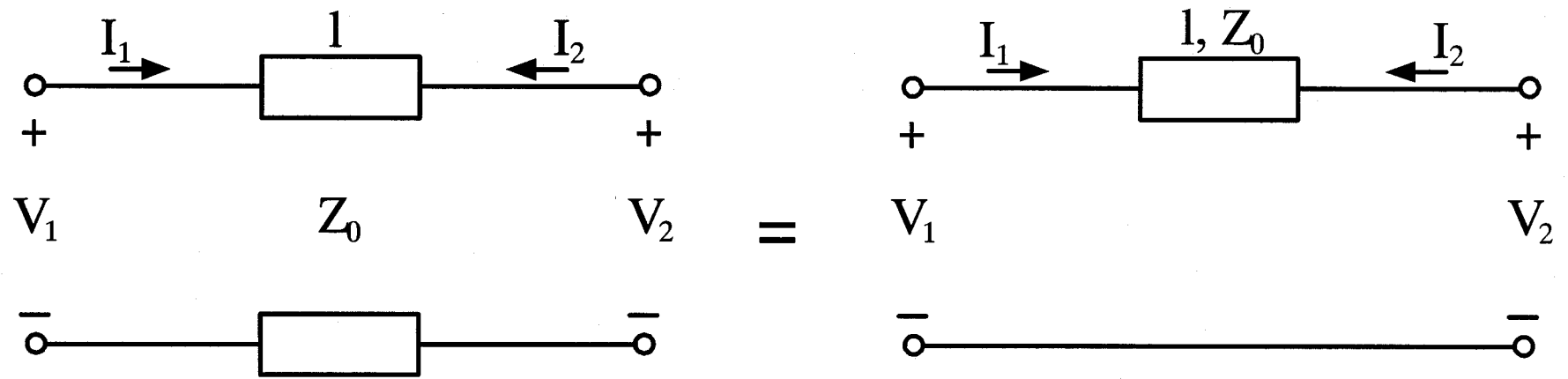Figure A.2 (a) A series element. (b) A parallel element.
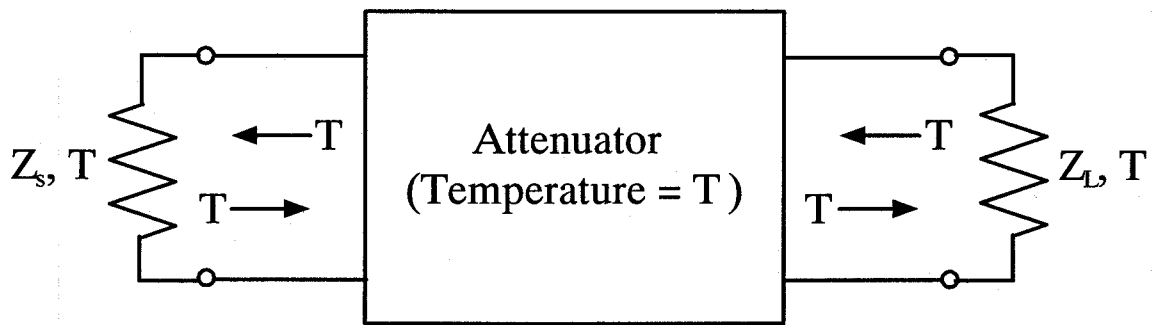
Figure A.3 A series transmission line.

Figure B.1 A terminated attenuator in thermal equilibrium. The noise delivered to each termination equals the noise that each termination delivers to the network.
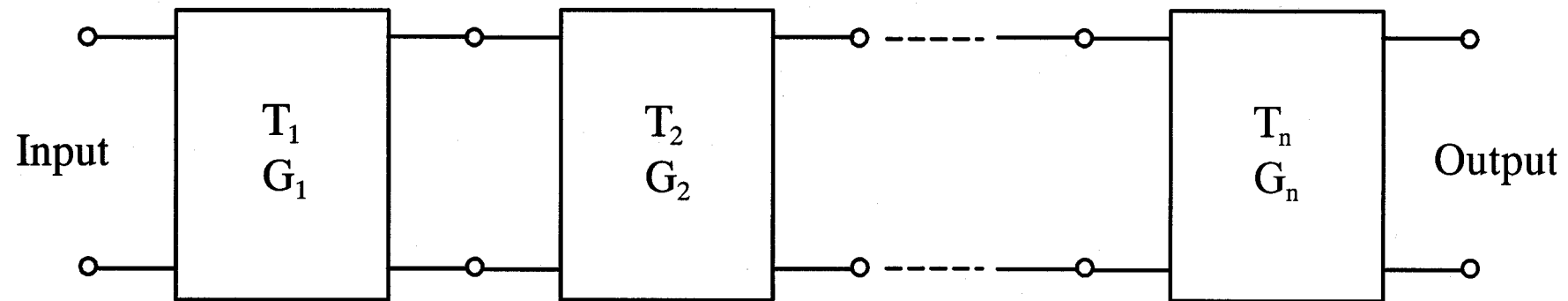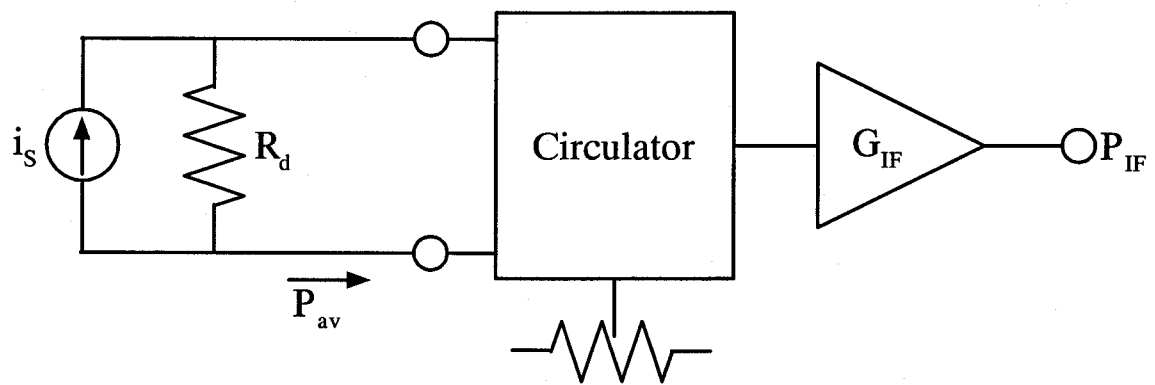
Figure B.2 Cascade of noisy two-port.

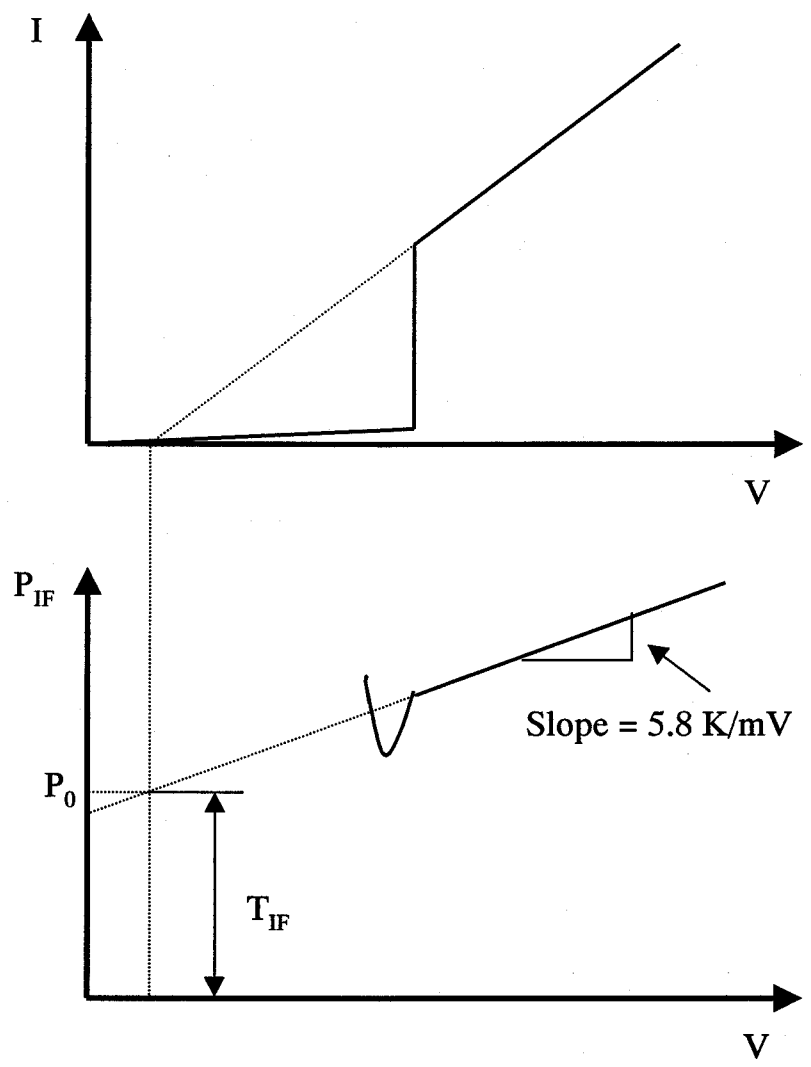Figure C.1 Equivalent circuit of an SIS receiver without LO power.

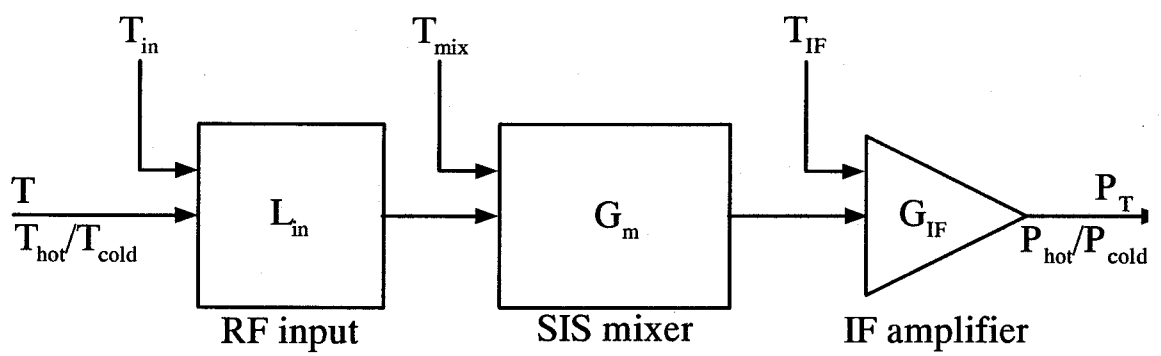Figure C.2 Typical I-V curve and the IF output of an SIS receiver.

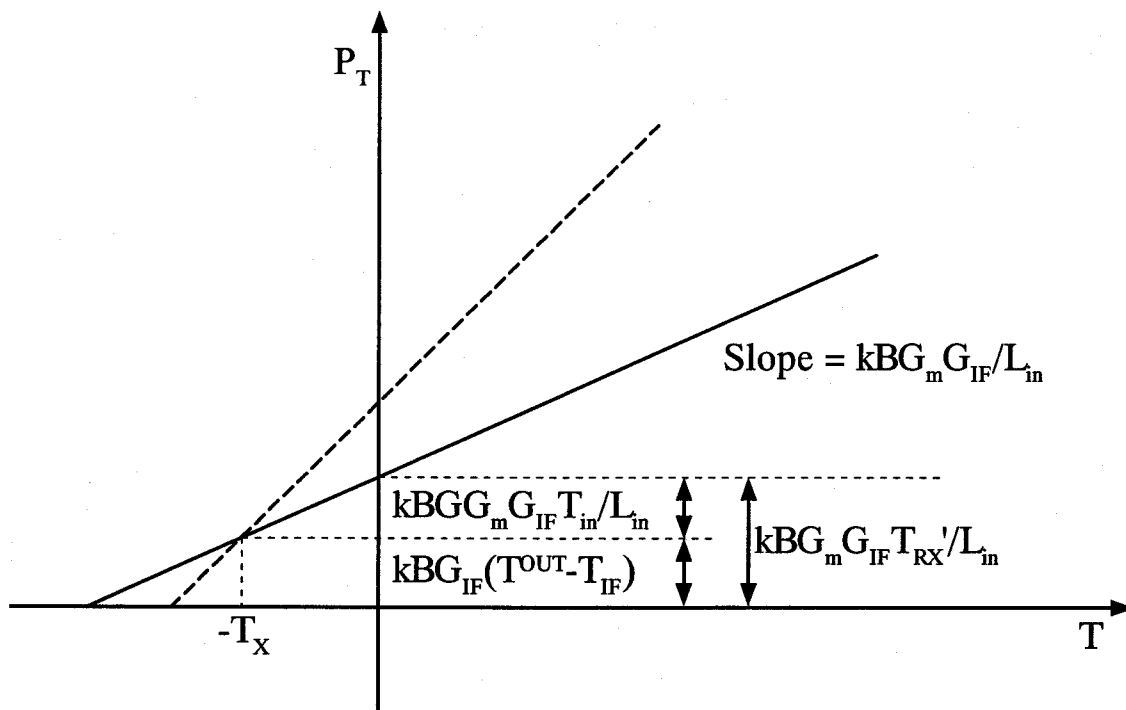Figure C.3 A standard block diagram of a heterodyne receiver.

Figure C.4 Contributions to the receiver output power for interpreting the intersecting lines technique are sketched.

Publication List

Papers

(1) <u>M. Takeda</u> and T. Noguchi, "Performance of inhomogeneous distributed junction arrays", *Appl. Superconductivity*, **2**, pp. 639-642 (1999).

(2) <u>M. Takeda</u>, T. Noguchi, and S. -C. Shi, "Predicted performance of superconductor-insulator-superconductor mixers with inhomogeneous distributed junction arrays", *Jpn. J. Appl. Phys.*, **39**, pp. 5095-5098 (2000).

(3) <u>M. Takeda</u> and T. Noguchi, "A 200-285 GHz waveguide SIS mixer with an inhomogeneous distributed junction array", *IEEE Trans. Microwave Theory Tech.*, **50** (2002), in press.

(4) H. Matsuo, S. Ariyoshi, H. Akahori, <u>M. Takeda</u>, and T. Noguchi, "Development of submillimeter-wave camera for Atacama Submillimeter Telescope Experiment", IEEE Trans. Appl. Superconductivity, **11**, pp. 688-691 (2001).

International Conference (first author) ·

(1) <u>M. Takeda</u> and T. Noguchi, "Performance of inhomogeneous distributed junction arrays", *4th European Conference on Applied Superconductivity* (EUCAS'99), Barcelona, Spain, September 1999.

(2) <u>M. Takeda</u>, T. Noguchi, and T. Yoshizawa, "A 190-300 GHz SIS mixer with an inhomogeneous distributed junction array", *8th International Superconductive Electronics Conference* (ISEC'01), Osaka, Japan, June 2001.

(3) <u>M. Takeda</u>, S. Asayama, T. Noguchi, and H. Ogawa, "A broadband SIS mixer with an inhomogeneous distributed junction array", *9th International Conference of Terahertz Electronics* (THz 2001), Virginia, U.S.A., October 2001.